Assessment of bias corrected satellite rainfall products for streamflow simulation: A TOPMODEL application in the Kabompo River Basin, Zambia

CALISTO KENNEDY OMONDI
February, 2017

SUPERVISORS:
Dr. Ing. T.H.M. Rientjes
Dr. B.H.P. Maathuis

Assessment of bias corrected satellite rainfall products for streamflow simulation: A TOPMODEL application in the Kabompo River Basin, Zambia

CALISTO KENNEDY OMONDI
Enschede, The Netherlands, February, 2017

Thesis submitted to the Faculty of Geo-Information Science and Earth Observation of the University of Twente in partial fulfilment of the requirements for the degree of Master of Science in Geo-information Science and Earth Observation.
Specialization: Water Resources and Environmental Management

SUPERVISORS:
Dr. Ing. T.H.M. Rientjes
Dr. B.H.P. Maathuis

THESIS ASSESSMENT BOARD:
Dr. Ir. C. van der Tol (Chair)
Prof. Dr. P. Reggiani (External Examiner, University of Siegen - Germany)

ABSTRACT

In many catchments, issues of limited hydro-meteorological data availability restrict effective water resources planning and management. Nowadays, satellite based meteorological products are available providing alternative source of hydro-meteorological information. Products, however, have inherent systematic and random errors constraining direct applications in hydrological modelling. With focus on assessing accuracies of satellite rainfall estimate, this study compares CMORPH, CHIRPS and TMPA estimates to rainfall estimates from 6 gauge stations for Kabompo Basin located in Zambia.

Comparisons are carried out at 0.05°, daily scales, over dry and wet seasons, and 6 rain rate classes for the period 2008-2012. Detection indices (e.g. POD, FAR and CSI) and frequency based statistics (e.g. RMSE, bias estimates and correlation coefficients) are computed and documented. This helps to understand how the rainfall products produce salient rainfall features for the dry and wet seasons and rainfall rates affecting runoff responses in the basin. Besides evaluating biases, focus is put on correcting prevailing systematic errors in the products by adopting linear based (Spatio-temporal) and an additive (Distribution Transformation) bias correction schemes. Further, Topographic driven model (TOPMODEL) is selected to illustrate how errors in the satellite rainfall products impact water balance closure.

For the selected rainfall products, CHIRPS product was less skilful in detecting extreme rainfall (<2.5 and >20 mmd^{-1}); signified by reduced rainfall occurrence detection capability to 20% during dry season. CHIRPS, however, had the least falsely detected rainfall (FAR<0.1 for dry period). Investigations reveal that better rainfall detections are achieved during wet than dry seasons. TMPA outperformed the other products detecting up to 88% of rainfall occurrence during wet season while CMORPH exhibited the best CSI between 0.69 and 0.8. The three products were found to underestimate rainfall depths (CMORPH bias: 1.56 mmd^{-1} and TMPA bias: 0.05 mmd^{-1}). TMPA exhibited a closer agreement with gauge observation (SD range 0.14 and 3.44 mm d^{-1}).

Research findings show that effectiveness of each of the bias correction schemes widely varies and depends on the indicator selected. Out of 5 selected bias correction schemes, most effective are DT (exhibiting highest CC > 0.7, least standard deviation of 0.52 mm d^{-1} and daily accumulated error of 5.24-10.42 mm), TFSV for correcting mean rainfall and TVSV exhibiting the lowest daily bias < 0.09 mm respectively. Finally, a clear improvement in water balance closure error is shown on bias correcting the satellite rainfall estimates to as low as 1.7%.

Keywords: Satellite rainfall estimates; Bias correction; TOPMODEL; Kabompo; Streamflow simulation

ACKNOWLEDGEMENTS

After almost eighteen months of intense MSc coursework, today I write a thank you note as a finishing touch on my thesis. The completion of the study received support from several individuals, whom I would like to reflect on.

I would first like to acknowledge the joint funding received from UTS-ITC Excellence Programme (University of Twente) and George E. Onyullo (PhD). Completing this MSc would have not been possible without your support, and I thank you for the opportunity.

A special thank you goes out to my tutors and colleagues at WRS department, Faculty ITC for their great support and willingness to help. I would particularly like to single out my supervisors: Dr. Ing. T.H.M. Rientjes and Dr. B.H.P. Maathuis, I want to express my kind and heartfelt gratitude for your unbound support and excellent cooperation giving me an opportunity to conduct and further my research. You definitely provided me tools required for successful completion of this work. Tom, your valuable guidance and counsel has not only nurtured my growth in the scientific field but also at personal level. Webster Gumindoga is greatly appreciated for providing part of the datasets used in this study, including deliberations we had along the process.

To my parents and entire family, words cannot express how thankful I am for all the sacrifices you have made. I would also like to acknowledge Francis, Martin, Pauline and Lali for your constant prayers and moral support that kept me motivated. Finally, there are these cheerful group of Kenyan colleagues particularly from WRS department: J. Mutinda, D. Kyalo, P. Murunga and K. Ochieng. We were always supportive to each other apart from talking about studies.

Thank you to all contributors, mentioned and unmentioned by names!

TABLE OF CONTENTS

LIST OF FIGURES

LIST OF TABLES

LIST OF ACRONYMS

CHIRPS	Climate Hazards group Infrared Precipitation with Stations
CHRS	Center for Hydrometeorology and Remote Sensing
CMORPH	Climate prediction center MORPHing technique
CSI	Critical Success Index
DT	Distribution Transformation bias correction scheme
FAR	False Alarm Ratio
FEWSNET PET	USGS Famine Early Warnings Systems Network potential evapotranspiration
GDAS	Global Data Assimilation System
IDL	Interactive Data Language
ILWIS	Integrated Land and Water Information System
KRB	Kabompo River Basin
POD	Probability of Detection
SREs	Satellite-based rainfall estimates
SRTM DEM	NASA Shuttle Radar Topographic Mission (SRTM) digital elevation model
STB	Spatio-temporal bias correction
TMPA	Tropical Rainfall Measuring Mission Multi-Satellite Precipitation Analysis – 3B42 version 7 product
TOPMODEL	TOPography based conceptual rainfall-runoff MODEL

1. INTRODUCTION

1.1. Background

Quantification of spatio-temporal changes in water cycle components is essential for promoting effective planning and management of water resources (Nourani et al., 2014). Such requires knowledge on hydrological processes which demands accurate hydro-meteorological information. Traditionally, *in-situ* meteorological measurements (either from rain gauge or weather radar) facilitate such assessments. In most catchments, however, especially the semi-arid and water limited environments, there are vast challenges faced with *in-situ* measurements networks. Some of the challenges manifest in the form of non-existence and sparse distribution of rain gauging networks (Behrangi et al., 2011; University of California, 2004; Wagner et al., 2009). Furthermore, radar installations for rainfall measurements are not available in many developing countries where resources are limited. As CHRS (2004) argues, topographic relief and mountains often also suffer from limited rain gauge installations thus resulting in large gaps in rainfall coverages. Quality of *in-situ* data is also a concern due to dependency on spatial and temporal scales (after Gosset et al., 2013). Besides, gauging flows in sensitive ecosystems such as floodplains is difficult or imprecise. This situation results in poor or inadequate *in-situ* data availability hampering effective water-related studies thus restricting affected water resources management, particularly for near-real-time predictions (Bhattacharya and Solomatine, 2015).

As an alternative to overcome such constrains, remote sensing technologies have evolved providing spatially and temporally continuous meteorological data for water related studies (Li et al., 2014). Furthermore, meteorological data from such satellite based models have large spatial coverages (e.g. less than 0.25°) and high temporal resolutions (e.g. daily and sub-daily) (Abera et al., 2016; Behrangi et al., 2011; Yang and Luo, 2014). For instance, the Climate Hazards Group InfraRed Precipitation with Stations data (CHIRPS; Funk et al., 2015) provides rainfall estimates at 0.05° resolution while from the USGS Famine Early Warnings Systems Network (FEWSNET) PET, daily global potential evapotranspiration information is accessible (Maathuis et al., 2014). Availability of these products near-real time facilitate modelling applications where water resources management is critical yet data collection and quality assurance is a concern (Xianghu et al., 2014). These products are available at varying accuracies, performances and resolution (spatial and temporal) thus impacting water resources modelling.

However, the accuracy of the satellite based meteorological estimates when compared to gauge measurements are often not impressive (Behrangi et al., 2011; Bhatti et al., 2016; Khan et al., 2011; Sun et al., 2012). They suffer from some inherent shortcomings and are contaminated with random and systematic errors (commonly termed as bias) as Pan et al. (2010) argued. These systematic differences arise from sensor limitations, retrieval algorithm errors, poor spatio-temporal sampling frequencies and sensor parameterization uncertainties among others (Hong et al., 2006; Maggioni et al., 2013). Results from several studies suggest that accuracies of the satellite rainfall products (hereinafter SREs) is dependent on topography, location, season, rain type, elevation, climatological factors; and manifest in the form of rainfall depths, occurrence and intensities (Dinku et al., 2008; Gumindoga et al., 2016; Habib et al., 2012; Yang and Luo, 2014).

Based on the aforementioned shortcomings, estimates from the satellite products need validation with *in-situ* measurements (that commonly is referred to as ground truth) to quantify their direct relevance for a targeted application (Abera et al., 2016; Xianghu et al., 2014). The systematic difference in the products then need adequate correction and refining before deemed fit for any water resources application (Habib et al., 2014). As Bhattacharya and Solomatine (2015) emphasized, adopting bias (error) correction can potentially compensate for these systematic differences in SREs thus improving their reliability.

Kabompo River Basin, focus area for this study, is a headwater basin of the Zambezi River Bain and located in the North-western part of Zambia. Like many African catchments, the basin is poorly covered by rain gauges. Issues of environmental changes in form of land cover (emanating from increased mining activities and deforestation) and climate changes are common in this basin (ZEMA, GRID-Arendal, GRID-Sioux Falls, UNEP, 2012). These aspects directly affect runoff response in the catchment, streamflow variability and frequency of hydrological extremes. As the hydrological regimes get affected, so does water balance in the basin, thus threatening sustainability of its water resources and consequently higher-order streams of Zambezi Basin.

1.2. Study relevance

This study is on use of bias corrected SREs for hydrological modelling for the Kabompo Basin in Zambia. The Kabompo is a head river basin for Zambezi Basin, a transboundary river basin shared by eight countries in the Southern African Development Community (SADC). In this regard, determining runoff response and water balance from the basin as it influences higher-order streams is urgently needed. Except for two recent studies carried out by Gumindoga et al. (2016) and Valdés-Pineda et al. (2016) in the Zambezi Basin, most bias correction schemes and/or assessments focus on Europe (e.g. Piani et al., 2010), America (e.g. Chen et al., 2013; Tobin and Bennett, 2010) and Asia (e.g. Tian et al., 2007) and so far, none has focused on the Kabompo Basin. In hydrological application in the Zambezi Basin, previous studies report on the use of uncorrected SREs despite evidence of errors in satellite products (Cohen et al., 2012). This study thus brings significant contributions to scientific community focusing on *i)* finding appropriate precipitation bias correction scheme for the Kabompo Basin; *ii)* understanding the efficiency and need of applying bias corrected SREs data in streamflow simulations of the basin, as an example of sparsely distributed rain-gauge basin; and *iii)* serves as a feedback to respective products' developers and end users in understanding the errors and uncertainties involved and how they propagate in hydrological response applications.

1.3. Problem statement

Water resource assessment and planning requires reliable rainfall data. Aspects of poor spatial distribution and non-existence of reliable rain gauge networks that applies to many catchments also applies to the Kabompo Basin. As such, satellite-derived rainfall has emerged as a viable option to indirectly retrieve rainfall estimates. However, accuracies of the rainfall products as compared to gauge measurements are often not impressive, so bias correction that can potentially compensate for the systematic errors is essential. Performance of the SREs also need to be assessed when estimates are used as inputs to hydrological modelling. For Kabompo Basin, the use of bias corrected rainfall estimates in streamflow simulations is yet to be fully explored. Furthermore, and among other factors, many studies reveal that accuracies of SREs are affected by season, yet very few studies have analysed such aspects. Motivated by this existing gap, this study thus attempts to assess effects of bias corrections of rainfall estimates from Climate prediction center MORPhing (CMORPH), Tropical Rainfall Measuring Mission (TRMM) Multi-satellite Precipitation Analysis (TMPA) 3B42v7 (hereinafter TMPA) and CHIRPS satellites. Inter-comparison of different seasonal performance, and application of SREs to streamflow simulations and water balance closure assessments are required to understand the runoff behaviour in the basin, applying Topographic driven model (hereinafter TOPMODEL).

1.4. Objectives and research questions

1.4.1. Objectives

The study aims at assessing the performance of bias corrected daily precipitation time series for streamflow simulation for the period 2008-2012 in the Kabompo Basin (Zambia) applying TOPMODEL.

Specific objectives are:

i. To evaluate the effect of elevation and seasonality on CMORPH, CHIRPS and TMPA satellite rainfall detection in the Kabompo basin,
ii. To apply and compare bias correction schemes for CMORPH, CHIRPS and TMPA rainfall for different rain rates and seasons,
iii. To parameterize TOPMODEL rainfall-runoff model using remote sensing data, and
iv. To assess water balance closure using TOPMODEL as affected by use of bias corrected CMORPH, CHIRPS and TMPA satellite rainfall.

1.4.2. Research questions

i. What differences in magnitude of errors exist between CMORPH, CHIRPS and TMPA estimates when compared to ground observations?
ii. What are the seasonal characteristics of CMORPH, CHIRPS and TMPA satellite rainfall in the basin?
iii. What is the most effective rainfall bias correction scheme for the Kabompo Basin?
iv. Does the use of bias corrected CMORPH, CHIRPS and TMPA satellite rainfall instead of gauge data improve TOPMODEL streamflow simulation and water balance closure for the basin?

This study hypothesises that space-time variant bias correction scheme results in improved satellite-rainfall driven streamflow simulations for the Kabompo Basin.

1.5. General research methodology

This research involved the acquisition and subsequent pre-processing of *in-situ* and remote sensing datasets required for TOPMODEL rainfall-runoff application for the Kabompo Basin. The *in-situ* based meteorological data for the period 2008-2012 were provided by Webster Gumindoga, who is a Ph.D. candidate at the WRS department, Faculty ITC. Similarly, satellite-based data were retrieved from respective data provider's archives and pre-processed in appropriate formats. These include ½-h CMORPH, 3-h TMPA and 24-h CHIRPS at 0.05°, 0.07° and 0.25° spatial resolutions respectively, plus SRTM-90m digital elevation model. TOPMODEL IDL code, a conversion of FORTRAN TOPMODEL version in Beven and Kirkby (1979), were acquired, checked and modified where appropriate for distribution modelling.

The collected *in-situ* meteorological data were subjected to quality assessments, completions and pre-processing. Subsequently, systematic errors in the SREs were assessed in comparison to rain gauge observations as ground truth. Based on literature, selected bias correction schemes were used in adjusting errors in satellite rainfall estimates prior to TOPMODEL simulations. The model was initialised, calibrated based on sensitive parameters and validated using gauge rainfall. Thereafter, uncorrected and bias corrected satellite rainfall estimates were independently used as forcing in the model; and consequently, water balance closure analysis done. Figure 1.1 outlines these general research sequence.

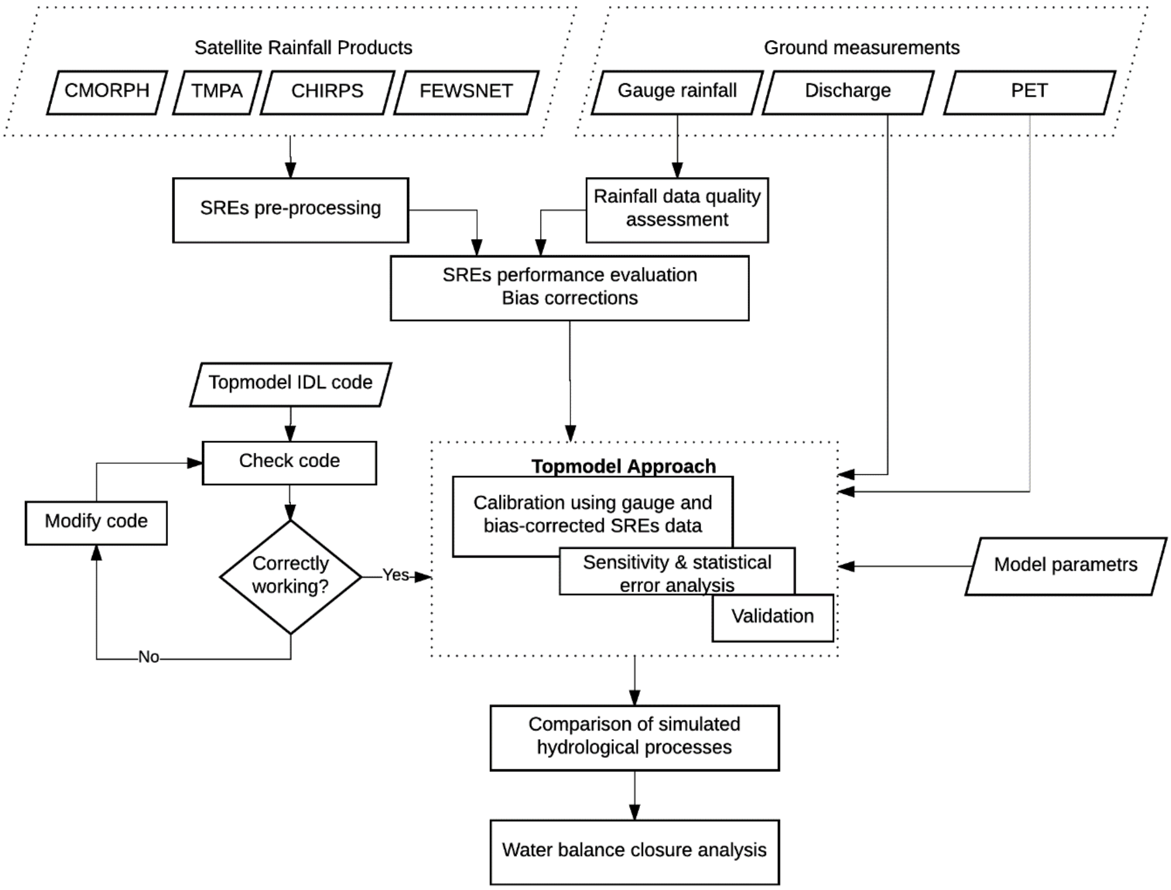

Figure 1.1: Schematic diagram outlining the general research sequence.

2. STUDY AREA AND DATA SOURCES

2.1. Study area

2.1.1. Geographical location and topography

The study focuses on a 69,737 km² Kabompo Basin, a headwater basin of Zambezi River Basin that is shared by eight SADC countries. The basin is located in the North-western part of Zambia between 11°S to 15°S latitude and 23°E to 26°E longitude. At its outlet is the basin's gauging station, the Watopa Pontoon, with an upstream area of ~ 67,261 km² (Kampata et al., 2013; Mwiza, 2012; Siwila et al., 2013). The Kabompo River originates from a highland forming the eastern watershed between the Zambezi and Congo River Basins. The river receives water flows from two rivers: Western Lunga and Dongwe. The elevation of the basin ranges from 1076 to 1508 m above mean sea level (SRTM) with lower elevation ranges at the South-western parts. It is characterised by undulating terrain and good network of tertiary drainage patterns. Figure 2.1 shows the location of the study area including the distribution of streamflow and rainfall measuring stations in and around the basin.

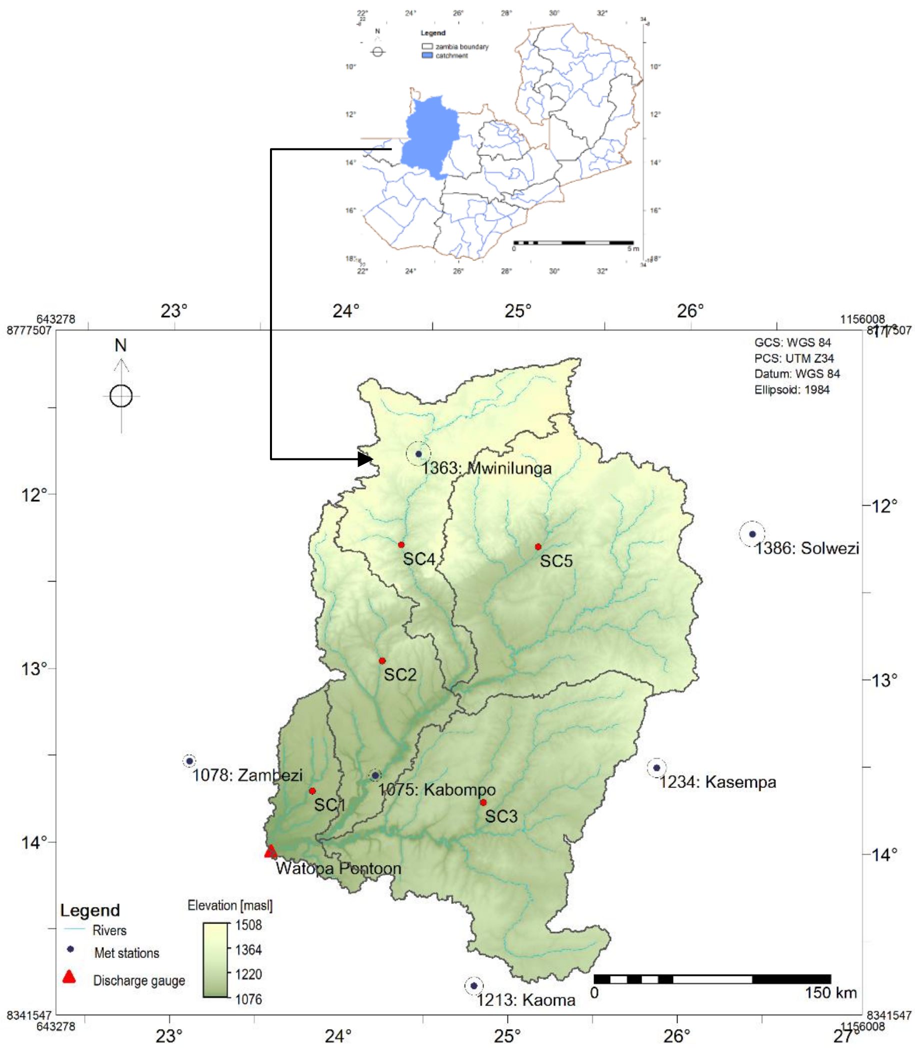

Figure 2.1: Location of the Kabompo Basin, Zambia and distribution of hydro-meteorological stations.

2.1.2. Climate and land cover

Kabompo Basin is described to have a sub-tropical savanna climate experiencing 3 distinct seasons: wet and hot (November – March), dry and cool (April – July) and dry and hot (August – October) (Kampata et al., 2013). On average the basin receives annual rainfall of ~1200 mm (World Bank, 2010). Its mean annual potential and actual evapotranspiration is estimated to be 1337 and 1113 mm respectively. The average temperature in the area is between 16 °C (in July) and 22 °C (in November). The variation of altitude and rainy seasons (driven by Inter-Tropical Convergence Zone – ITCZ) are reported to affect the tropical climate in the region (Siwila et al., 2013). Summer rainfall patterns in the region are also reported to be dependent on the El Nino/Southern Oscillations phenomenon.

The north and south of the Kabompo River is confined with a dense tropical evergreen forest dominated by *Crypotsepalum exfoliatum pseudotaxus*, locally known as *mavunda* (WWF, 2006). The rest of the region is dominated by miombo and savanna woodlands. However, increased mining activities in the Upper Kabompo Basin and encroachment of agriculture into Forest Reserves (e.g. Ndeta Forest Reserves) have resulted in loss of forest cover.

2.2. In-situ data

Daily time series of precipitation, air temperature, humidity, wind speed, sunshine hours and discharge from stations in and around the basin are obtained from Webster Gumindoga, a Ph.D. candidate at WRS department, Faculty ITC. Based on proximity to the basin, only 6 stations shown in Figure 2.1 are suitable for the study. Four stations namely Kabwe, Kalabo, Mongu and Senaga, for which *in-situ* data were available, are then excluded.

For precipitation, recording period is 1998-2013 for all stations except Kabompo (1998-2005) with data gaps existing. The historical discharge data collected are for the period 01/01/1998 - 30/04/2013, with missing records. This is measured at Watopa Pontoon, the basin's only discharge-gauging station with upstream area of ~67,261 km² from 5 sub-catchments. Potential evapotranspiration variables are limited and vary between the stations with several missing records, particularly in recent years. For instance, solar radiation was only available at Mwinilunga and Zambezi stations while Kasempa had no wind speed record. An inventory of meteorological variables from the selected stations are summarized in Table 2.1.

Table 2.1: An inventory of meteorological variables collected from stations in and around the basin.

Station		Coordinates of station		Type of meteorological variable from the station						
ID	Name	Lat.	Lon.	Altitude	P	Tmax	Tmin	RH	WS	SS
675430	Kabompo	-1360	+02420	+1075	x	x	x	x	x	
676410	Kaoma	-1480	+02480	+1213	x	x	x	x	x	
675410	Kasempa	-1353	+02585	+1234	x	x	x	x		
674410	Mwinilunga	-1175	+02443	+1363	x	x	x	x	x	x
675510	Solwezi	-1218	+02638	+1386	x	x	x	x	x	
675310	Zambezi	-1353	+02311	+1078	x	x	x	x	x	x

P –rainfall, Tmax - daily maximum temperature. Tmin – daily minimum temperature, RH – relative humidity, WS – wind speed and SS – sunshine hours

2.3. Satellite rainfall estimation products

In this section, three high resolution satellite rainfall products for which their accuracies are compared and evaluated against rain gauge observations are described. These are Climate Prediction Center MORPHing (CMORPH; Joyce et al. 2004), Tropical Rainfall Measuring Mission Multi-satellite Precipitation Analysis version 7 (TMPA 3B42 v7; Huffman et al., 2010) and Climate Hazards group InfraRed Precipitation with Stations (CHIRPS; Funk et al., 2015). Table 2.2 gives a summary of the selected products with brief descriptions.

Table 2.2: Main characteristics summary of satellite rainfall products used.

Rainfall product	CMORPH	TMPA	CHIRPS
Provider	NOAA-CPC	NASA	CHG, USGS
Spatial coverage	60°N to 60°S, globally	50°N to 50°S, globally	50°N to 50°S, across all longitudes
Temporal coverage	Since 01.01.1998	since 01.01.1998	Since 01.01.1981
Period tested	2008-2012	2008-2012	2008-2012
Original/ used spatial resolution	0.07° / 0.05°	0.25° / 0.05°	0.05°
Original/ used time step	½ h / 24 h	3 h / 24 h	24 h
Main input data sources	Geostationary IR, SSM/I, AMSU, AMSR-E, and TMI	Geostationary and LEO IR, TCI, SSM/I, AMSU, AMSR-E, CAMS and GPCC	CHPClim, Geostationary IR, TRMM 3B42 products, CFSv2, In-situ precipitation observations from various sources e.g. GHCN, GSOD
Retrieval algorithm	Precipitation estimates are based on PMW data. IR data are only used in deriving CSAVs to propagate PMW-derived precipitation. The estimates are adjusted using GPCP data (Tramblay et al., 2016).	MW-based estimates are merged and calibrated, then combined with IR-based estimates. Combined estimate is then rescaled using monthly CAMS and GPCC data.	Blends 0.05° CCD-based rainfall estimates with ground station data to produce preliminary products (2-days latency) and final product (with 3-weeks latency). The CCD-estimates are calibrated using TMPA 3B42 v7.
References	Joyce et al. (2004)	Huffman et al. (2007)	Funk et al. (2015); Funk et al. (2014)
For data access	ftp://ftp.cpc.ncep.noaa.gov/precip/	http://mirador.gsfc.nasa.gov/	ftp://ftp.chg.ucsb.edu/pub/org/chg/products/

CMORPH is chosen because of validation results by Dinku et al. (2008) who showed detection capability up to 63% of rainfall occurrence over the Zambezi region; and because of high spatial (0.07°) and temporal resolution (½ h) the product is available. Similarly, TMPA provides long time-series data for runoff simulation which increases the period of records available for calibration and validation as shown by Cohen et al. (2012); and is suitable for rainfall distribution assessments (Huffman et al., 2016). Selection of CHIRPS is motivated by its fairly low latency and bias, high resolution, long period of record and suitability for hydrological assessments in data sparse regions dependent on convective rainfall (Funk et al., 2015). Moreover, these products cover the study area and are readily accessible online by end users.

2.3.1. CHIRPS rainfall product

The Climate Hazards group InfraRed Precipitation with Stations (CHIRPS) is a quasi-global (50°S-50°N) infrared Cold Cloud Duration (CCD) based precipitation estimates (Funk et al., 2015). Main data sources for CHIRPS creation include CHPClim, quasi-global geostationary IR satellite observations from CPC and NCDC, TRMM 3B42 product from NASA, atmospheric model rainfall fields from the NOAA CFSv2 and *in-situ* precipitation from various sources (Funk et al., 2014).

The CHIRPS algorithm involves: *i)* creating infrared precipitation (IRP) pentad estimates from satellite information (i.e. based on 0.05° CCD) to represent sparsely gauged locations, then *ii)* expressing IRP pentad as a percent normal by dividing the values with their long-term averages, *iii)* resulting normal IRP pentad is then multiplied by corresponding CHPClim pentad to give CHIRP – unbiased gridded estimate, then *iv)* CHIRP is blended with stations data to produce CHIRPS (after Funk et al., 2015). The CCD-estimates are calibrated using TMPA 3B42 v7 products. For this study, the CHIRPS Africa daily precipitation product at 0.05° resolution used are sourced from ftp://ftp.chg.ucsb.edu/pub/org/chg/products/ accessible as at November 2016.

2.3.2. TRMM rainfall product

The TRMM TMPA 3B42 version 7 dataset uses TMI orbit data (from 2A12 rain estimates) and monthly TCI calibration parameters (from 3B31 rain estimates) in adjusting merged-IR rain rates to produce

TRMM-adjusted merged infrared and root mean square precipitation-error estimates (Huffman et al., 2016). Major data sources for the TMPA are precipitation-related passive microwave data from low-earth-orbit (LEO) satellites and window channel (~10.7 μm) infrared brightness temperatures data from geostationary satellites. It also employs TCI estimates and monthly rain gauge analysis from GPCC and CAMS (Huffman et al., 2007).

The TMPA estimates are generated by calibrating and combining precipitation-related microwave data to TRMM TCI; monthly microwave-IR histogram matching is then applied to compute IR precipitation estimates; which is used in filling missing data in individual 3-h merged microwave fields; then applying inverse-error-variance weighting, monthly totals of the 3-h multi-satellite are integrated with monthly GPCC rain gauge data producing TRMM 3B43; finally each of the 3-h field in the month are scaled by computing the ratio between satellite-gauge combination and multi-satellite product (Huffman et al., 2007, 2010). This gives 3-h 3B42 estimates [mm h^{-1}] at 0.25° spatial resolution with a global coverage of 50°N-50°S. This dataset is only used to the extent of the study area and accessed from http://mirador.gsfc.nasa.gov/.

According to Liu (2015), TMPA product is relatively better than its precursors in providing accurate estimates given substantial changes in its input datasets and algorithm, thus extensively used in research. Its key limitations however include consistent overestimation of calibrated microwave data (3-5% higher than 2B31 calibrator) and deficiencies in precipitation occurrence originating from introduction of IR data sources at different points (e.g. AMSU-B over 2000-2003). However, this is corrected at monthly scales (Huffman, 2013).

2.3.3. CMORPH rainfall product

The CPC Morphing technique (CMORPH) is based on morphing approach where passive microwave (PMW) derived precipitation estimates and infrared (IR) brightness temperature are blended to generate high resolution (~0.10°, latitude/longitude, ½-h) global (in longitude, 60°N-60°S) precipitation (Joyce et al., 2010). The geostationary satellite IR data used is retrieved from the European Meteosat-5/7 (at ½-h interval), US GOES-8/10 (every 3-h) and Japanese MTSAT (hourly). PMW information are generated from polar orbiting satellite such as TMI, SSM/I and AMSU. Tables 1 and 2 by Joyce et al. (2004) summarizes these geostationary and PMW sensors.

The CMORPH dataset generation involves assembling all ½ h, 8-km combined PMW rainfall estimates from various sensors, calibrated to TRMM TMI 2A12; IR data is then used in deriving cloud system advection vectors (CSAVs) to spatially propagate forward and backward in time the combined PMW rainfall for every ½ h of the day; subsequently both forward- and backward-propagated rainfall are inversely-weighted by the respective temporal distance from observed PMW rainfall – producing the shape and intensity of precipitation at a location every ½ h (Joyce et al., 2004). This study uses CMORPH rainfall product at ½ h and 0.07° resolution from ftp://ftp.cpc.ncep.noaa.gov/precip/ archives.

2.4. FEWSNET global potential evapotranspiration product

The USGS Famine Early Warnings Systems Network (FEWSNET) PET provided daily global potential evapotranspiration used in evaluating suitability of FAO-56 calculated ET_0 for this study. It is estimated based on weather parameters extracted from Global Data Assimilation System (GDAS) analysis fields generated every 6 hours by NOAA – including air temperature, atmospheric pressure, wind speed, relative humidity and solar radiation (Maathuis et al., 2014). Standardized Penman-Monteith equation (2.1) (after Allen et al., 1998) is used in computing the 6-hourly global PET. This is then aggregated to give daily PET, λET [mm d^{-1}].

$$\lambda ET = \frac{\Delta(R_n + G) + \rho_a C_p \frac{(e_s - e_a)}{r_a}}{\Delta + \gamma\left(1 + \frac{r_s}{r_a}\right)} \tag{2.1}$$

where R_n is the net radiation [MJ m^{-2} d^{-1}], G is ground heat flux [MJ m^{-2} d^{-1}], $(e_s - e_a)$ is air vapour pressure deficit [kPa], ρ_a is mean air density at constant pressure [kg m^{-3}], C_p is specific heat of air [MJ kg^{-1} °C^{-1}], Δ is the slope of the saturated vapor pressure curve [kPa °C^{-1}], γ is the psychrometric constant [kPa °C^{-1}], r_s and r_a are the (bulk) surface and aerodynamic resistances [s m^{-1}].

The PET data is available since 2001 at 1° spatial resolution with global spatial coverage (180°W to 180°E longitude, 90°N to 90°S latitude). This study uses daily FEWSNET PET at 1° grid size for 2001-2013 retrieved from http://earlywarning.usgs.gov/fews/datadownloads/Global/PET/days.

2.5. SRTM 90m digital elevation model

The NASA Shuttle Radar Topographic Mission (SRTM) digital elevation model is a product of NASA's SRTM in 2000 (Farr et al., 2007). It is offered and distributed free of charge by NASA/USGS through Earth Explorer (via USGS EROS Data Center accessible at http://earthexplorer.usgs.gov/) as a post-processed 3-arc second (~90m resolution at equator) global elevation data. The SRTM 90m DEM's geographical coverage is 60°N-57°S latitude by 180°W-180°E longitude.

Selection of this digital elevation is motivated by its high resolution, less vertical error ~16 m as reported by CGIAR (1998) and availability in different formats (GeoTIFF, BIL and DTED) facilitating seamless data processing in GIS applications. Selected 90m resolution version is a trade-off between the size of the basin and desire of having a fine-scale raster DEM that better describes the hillslope flow paths required in modelling rainfall-runoff processes as Gumindoga et al. (2011) argued. The SRTM data used in the study is retrieved in GeoTIFF format from http://droppr.org/srtm/v4.1/6_5x5_TIFs/ at 5 x 5 degree tiles.

3. LITERATURE REVIEW

3.1. Image re-sampling and scale issues

Most spatial data are collected at variable spatial scales from a variety of sources and often they are incompatible. As a result, selecting an appropriate scale to use for specific remote sensing application usually is challenging (Gotway and Young, 2002). This is because, studying spatial information at one scale may differ on applying another scale. Furthermore, integrating such spatial information at multiple scales is increasingly becoming common leading to increased concern on scale issues. This requires unifying scale that permits merging and comparing spatial data from various sources and at multiple scales. In remote sensing, this is achieved through resampling.

As Santhos and Devi (2010) describes, image resampling involves interpolating new pixel values of a raster image from existing pixel values whenever a raster image is rescaled (i.e. rows and columns modified) or re-projected to a different coordinate reference system. More often after geometric corrections, raster images only maintain their spatial extents but not spatial information stored within the pixels (e.g. measured precipitation, surface reflectance derived from respective sensors). This becomes a concern when dealing with satellite imagery where scientific interpretation and data integrity ought to be upheld.

Nowadays, several GIS and image-editing applications exist offering variety of resampling techniques for computing new pixel values, the commonly used in remote sensing given in increasing order of complexity and accuracy are nearest neighbour (Cover and Hart, 1967), bilinear interpolation and cubic convolution. Each of these techniques have their own pros and cons, necessitating careful considerations driven by intended application of the resampled output, an understanding of error propagation and potential effects introduced on resampling satellite imagery. Besides, assessing how the interpolated and original pixel values correlate and how best their corresponding averages are preserved is a requisite.

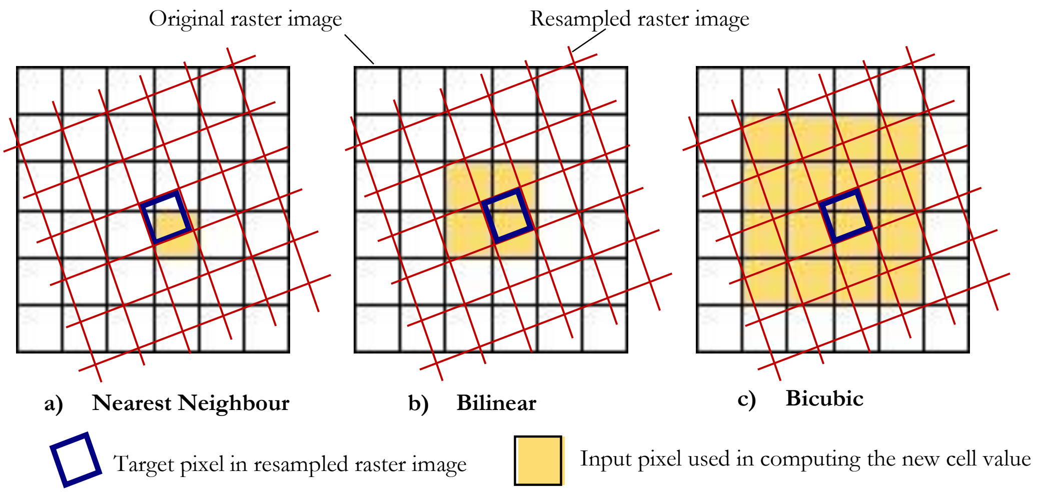

Figure 3.1: Schematic diagram showing nearest neighbour, bilinear and bicubic resampling principles.

The *nearest neighbour resampling* determines the value of a pixel in a resampled raster by matching it to the corresponding position in an original raster. In case no corresponding pixel is available, the nearest pixel is used. For instance, in Figure 3.1 (a) considering the red and black grids as resampled and original raster images respectively, the value of the target pixel (dark blue) is determined by assigning it the value of the yellow pixel (i.e. nearest original pixel).

The nearest neighbour method is useful because of its speed, simplicity and ability to preserve original pixel values hence widely suits discrete and sometimes continuous data. The method is, however, known to result in noticeable disjointed appearance and occasionally giving duplicate pixel values or omitting them thus considered least accurate interpolation method (Studley and Weber, 2011).

In the case of *bilinear interpolation,* a linear distance-weighted average of four nearest pixels in the original raster closest to the target pixel is calculated applying a 2x2 kernel, as illustrated in Figure 3.1 (b). This method tends to smoothen the output raster grid and gives better positional accuracy than nearest neighbour method thus suitable for up-sampling. However, it introduces some blurring effect on the resampled raster edges. In addition, the method alters original pixel values through the averaging process introducing a new set of values never existing in the original raster; which may be undesirable for subsequent quantitative analysis (Santhos and Devi, 2010).

The *bicubic resampling* (also known as cubic convolution), is similar to bilinear interpolation only that the target pixel value is calculated based on cubic distance-weighted average of sixteen surrounding pixels in the original raster as demonstrated in Figure 3.1 (c). This method produces a more continuous, smooth and accurate results with no disjoints than either bilinear or nearest neighbour resampling. In some cases, however, it may result in resampled pixel values that are outside the range of observed input values, including negative values (ESRI, 2016). A phenomenon that arises when cubic convolution fits a smooth curve to a local window with high deviance data (i.e. extremely different values across small distances) or applying unconstrained splines. In essence the algorithm can extrapolate data to maintain its full variation of the datasets. Another shortcoming is that resampling requires much computing time.

3.2. Bias in satellite rainfall products and their correction

Several studies reveal that accuracy of satellite rainfall products, when compared to gauge measurements are less impressive (e.g. Bhattacharya and Solomatine, 2015; Bhatti et al., 2016; Sun et al., 2012). Results from these studies suggest that SREs are contaminated with inherent random and systematic errors, which is directly linked to how the estimates are derived (Pan et al., 2010); the former tend to cancel out when products are considered at large spatial and temporal scale (Jobard et al., 2011). As described in Smith et al. (2006), this systematic difference between satellite and ground truth is commonly termed as bias, and computable based on equation (3.1) after Gosset et al. (2013). In the equation, G_i and S_i are daily rainfall series from gauge and satellite, while N is the total number of days considered.

$$Bias\ [mm\ d^{-1}] = \frac{\sum_{i=1}^{N}(S_i - G_i)}{N} \tag{3.1}$$

As explained in Tian et al. (2009), this uncertainty associated with SREs can further be decomposed into *a) hit bias*: difference occurring when both satellite and gauge detect rainfall leading to under/over estimations; *b) missed rainfall:* total rainfall depth reported by gauge when satellite detects nothing, and *c) false rain:* occurring when satellite falsely detect rainfall. These error components are obtainable using equations in Table 3.1.

Table 3.1: Satellite rainfall error components.

Bias type	Short description	Equation
Hit bias	Total difference between satellite and gauge rainfall depths when both detect rainfall leading to over or underestimations.	$HB = \sum_{i=1}^{n} (P_s - P_g) \| (P_s > 0 \& P_g > 0)$
Missed rain bias	Total rainfall depth reported by gauge when satellite detects nothing.	$MRB = \sum_{i=1}^{n} P_g \| P_s = 0 \& P_g > 0)$
False rain	Total amount of satellite falsely detected rainfall.	$FRB = \sum_{i=1}^{n} P_s \| P_s > 0 \& P_g = 0)$

where P_s and P_g are satellite and gauge based data at day i.

Based on the above uncertainties, many efforts have been devoted to examine the quality of various satellite estimates versus *in-situ* observations around the world; that encompasses characterising and quantifying the errors (e.g. Alemohammad et al., 2015; Hong et al., 2006; Maggioni et al., 2013; Mei et al., 2014; Tian et al., 2007). Examples in Africa include Dinku et al. (2008) and Jobard et al. (2011) focusing on East and West Africa respectively. The former evaluated 10 satellite products at monthly and decadal precipitation accumulations and found products' accumulated errors to vary from 45 to 60% indirectly relating to time steps; while the latter found CMORPH to have a stronger positive bias out of 7 operational products evaluated at 10-daily timescale.

Some studies that evaluate CMORPH accuracy include Cohen et al. (2012) who found the product to overestimate rainfall volume over Zambezi River Basin as large as 40% at monthly time scale; Gosset et al. (2013) demonstrating this product overestimating daily rainfall in Niger by an average of 2 mm; Jobard et al. (2011) and Dinku et al. (2008) respectively showing it poorly performed in West Africa and Ethiopia exhibiting low linear correlations (~0.32) when decadal estimates were used. In western highland of Ethiopia, Dinku et al. (2010) show that CMORPH and TMPA overestimated rainfall occurrence by 13% and 11% respectively. Evaluating TRMM-3B42 v7 in Morocco, Tramblay et al. (2016) found the product adequately reproducing observed precipitation patterns (i.e. monthly and annual totals) but underperformed in detecting precipitation extremes in Nepal as shown by Duncan and Biggs (2012).

Several studies (e.g. Dinku et al., 2008; Gumindoga et al., 2016; Habib et al., 2012; Yang and Luo, 2014) reveal that satellite rainfall biases are highly influenced by topography, location, season, rain type, elevation, and climatological factors; and manifest in the form of rain depths, occurrence and intensities. Carrying a study in the northern Russia, eastern coastal Canada and along Bering Strait coasts, Tian et al. (2007) demonstrated that negative biases in daily precipitation can be as large as 50-100% in cold seasons over high latitudes. Evaluating rainfall products over complex mountainous terrain, Ward et al. (2011) show that both PERSIANN and TMPA experienced difficulties detecting light rainfall amounts thus resulting in underestimates during the dry season. In the Great Rift Valley and Awash River Basin (Ethiopia), TMPA and CMORPH exhibited elevation-dependency showing rainfall underestimations at higher elevations (Hirpa et al., 2010). According to Yamamoto et al. (2011), PERSIANN exhibited large differences during winter whereas CMORPH overestimated rainfall in the pre- and post-monsoon seasons over Nepal Himalayas. These errors in rainfall products impair their use in water-related applications. It is, therefore, essential that they be assessed, corrected and adequately refined to improve their reliability (Aghakouchak et al., 2012; Habib et al., 2014).

As discussed in several studies (Bhatti et al., 2016; Chen et al., 2013; Fang et al., 2015; Habib et al., 2014; Lee et al., 2015), many bias correction algorithms have been proposed to correct systematic errors in

SREs. Examples include mean based comparisons (Seo et al., 1999), quantile-matching (Li et al., 2010), spatio-temporal methods, distribution-based, power transformation bias corrections, and multiplicative shift technique (Ines and Hansen, 2006). The choice of any of the schemes is driven by desired accuracy levels of the bias corrected products, the application for which the bias corrected product is meant (Habib et al., 2014), and the accountability of spatial and temporal patterns in the bias.

Globally, researchers continue to assess various bias correction schemes including performance of bias corrected products. For instance, Gumindoga et al. (2016) evaluated 5 bias correction schemes for CMORPH across 54 rain gauge stations in Zambezi Basin and found Distribution Transformation and Spatio-Temporal bias schemes to be effective in correcting mean values of CMORPH for the basin. The latter reduced CMORPH rainfall bias at ~70% of the stations. Power transformation scheme poorly performed for the upper Zambezi (with a RMSE ~10.1 mm d^{-1}) for 1998-2013. In the study, a minimum of 5 rainy days within preceding 7-day window and at least 5 mm rainfall accumulated depth was used in bias factor calculation. Bhatti et al. (2016) in the Gilgel Abbay watershed (Ethiopia) proposed and identified 7-days sequential window approach as most effective in assessing and correcting CMORPH rainfall error distribution. In the procedure, a multiplicative shift technique that entails multiplying the uncorrected satellite estimates with spatially interpolated bias factor was applied. Aghakouchak et al. (2012) investigated systematic and random error components of CMORPH, PERSIAN and TMPA over different seasons, thresholds and temporal accumulations; concluding that spatiotemporal characteristics of errors should be considered in choosing appropriate bias correction procedure. Lafon et al. (2013) compared 4 bias correction techniques: linear, non-linear, empirical and γ-based quantile mapping; concluding that non-linear scheme is more effective in correcting daily precipitation simulated by HadRM3-PPE-UK, a regional climate model.

3.3. Hydrological simulations

3.3.1. Sampled hydrological modelling based on bias corrected data

Apart from correction of errors in satellite products, their application in rainfall-runoff modelling application has gained attraction in hydrology. For instance, Habib et al. (2014) forced Hydrologiska Byråns Vattenbalansavdelning (HBV-96) with CMORPH bias corrected data based on 3 spatio-temporal schemes for the Gilgel Abbay catchment; and show that accounting for temporal variability largely influence rainfall-runoff simulations. Besides, observed hydrograph patterns and volumes were better captured when using bias corrected products instead. Chen et al. (2013) compared the performance of 6 bias correction methods for hydrological modelling in North America using HSAMI and highlighted that hydrological model performance is highly dependent on suitable bias correction scheme adopted. Tian et al. (2007) forced Community Land Model version 3 (CLM3) land surface model with bias corrected precipitation and found bias corrections applied to induce snowfall accumulation which resulted in runoff and streamflow increasing by up to 0.6 mm d^{-1} and 25% respectively for most rivers in the northern latitudes. Errors in bias corrected precipitation were found to propagate in runoff modelling simulations by Teng et al. (2015).

3.3.2. TOPMODEL application

TOPMODEL, a topography-based variable contributing area conceptual model of Beven and Kirkby (1979), is among the many models used in hydrology to predict streamflow in data scarce environments. The model relies on catchment topography, soil transmissivity and slope for its distributed and semi-distributed predictions of hydrological responses (Beven and Freer, 2001; Devia et al., 2015). Topography in the model is analysed by means of gridded elevation data (DEM) (Rientjes, 2015). Currently, the model supports the use of finer resolution raster DEM thus, better defined flow paths for rainfall-runoff simulations (Gumindoga et al., 2011). The model structure consists of 3 soil layers: saturated, unsaturated and root zones.

Among other governing equations detailed in (Beven and Kirkby, 1979; Rientjes, 2015), the model computes local storage deficit (S_i) as a function of topographic index, TI in equation (3.2). TI values are directly proportional to local saturation degree (expressed as S_i/m) by large upstream contributing areas (Quinn et al., 1995). Since equal TI values behave in a hydrologically similar manner, the index is considered a measure of hydrological similarity of any point in the catchment (after Muhammed, 2012).

$$TI = \ln\left(\frac{a}{T_0 \tan\beta}\right) \tag{3.2}$$

where a is, specific discharge contributing area, $\tan\beta$ is the local topographic gradient and T_0 is the effective soil transmissivity of top soil when saturated.

According to Beven & Freer (2001) and Rientjes (2015), the model simplifies reality on dynamic flow behaviour across saturated flow domain by assuming that:

a) the dynamics of the saturated zone are approximated by successive steady state representations,
b) effective hydraulic gradient of the saturated zone can be approximated by the local topographic surface gradient (tan β),
c) effective down slope transmissivity of a soil profile at a point is a function of soil moisture deficit at that point, and
d) "saturation of the soil column occurs from below and as such runoff generated by the saturation excess overland mechanism" (Gumindoga, 2010).

In Table 3.2, a summary of TOPMODEL parameters adapted from works of Gumindoga et al. (2014) are given. Previous studies (e.g. Gumindoga et al., 2014, 2011) indicate m , T_0 and SR_{max} as the most sensitive parameters for hydrological modelling.

Table 3.2: TOPMODEL parameters (after Gumindoga et al., 2014).

Parameter	Description	Equation
m[m]	Scaling parameter that controls the rate of decline of transmissivity function which is a function of local storage deficit or depth to water table. Value range 0.001-0.05	$T = T_0 e^{-s_i/m}$
T_0[m²/h]	Effective transmissivity of top soil when saturated. Value range 0.01-2.25	$T = T_0 e^{-s_i/m}$
t_d [h]	Time delay constant for infiltration to recharge the saturated zone. Value range 0.01-24	$q_v = \frac{S_{uz}}{S_i t_d}$
CHV[m/h]	Overland flow velocity. Ranges are catchment specific	$t_d = \sum_{i=1}^{N} \frac{x_i}{CHV tan\beta_i}$
RV[m/h]	Stream flow velocity. Ranges are catchment specific	$E_a = E_p(1 - SRZ/SR_{max})$
SR_{max}[m]	Maximum root zone available water storage capacity. Published range 0-0.3	$\frac{dQ_b}{dt} = \frac{Q_b}{AS_m}\frac{dQ_b}{d\delta}$
Q_b[m/h]	Initial stream discharge representing base flow	
SR_0[m]	Initial root zone moisture deficit. Range 0.001-0.1	
$INFEX$[-]	Flag for infiltration simulation. Activated when set to 1 to include infiltration excess calculations, otherwise 1	
K_{sat} [m/h]	Hydraulic conductivity and land surface that declines with depth	
ψ_f[m]	Effective suction head for infiltration excess flow calculations	
θ [-]	Change of water content across the wetting front	

For hydrological simulations, the model requires these ASCII files: *i)* project file describing application and input file names and paths, *ii)* catchment data file with topographic index distributions and other parameter values in Table 3.2, *iii)* forcing input data (daily accumulations of precipitation, potential evapotranspiration and observed discharge as model calibration target), *iv)* topographic index map data file and *v)* distance to outlet file for routing channel and overland flows.

4. RESEARCH METHODS

4.1. Methodological approach

In the study, both *in-situ* hydro-meteorological and remote sensing data are used. The former was provided by Webster Gumindoga, a Ph.D. candidate at the WRS department, Faculty ITC while the latter were retrieved from respective providers' archives discussed in sections 2.2-2.5. *In-situ* data consistency checks and completion were done by incorporating SASCAL WeatherNet information accessible at http://www.sasscalweathernet.org/.

Focussing on assessing accuracies of satellite rainfall products, point-to-pixel derived estimates of CMORPH, CHIRPS and TMPA were compared with gauged counterparts from 6 stations across Kabompo Basin located in Zambia. The comparisons are carried out at 0.05°, daily scales, over dry and wet seasons and 6 rain rate classes for the period 2008-2012. Commonly applied evaluation metrics are computed, documented and analysed to understand how the selected products produce salient rainfall features seasonally and within different rain rate classes affecting rainfall-runoff responses. Such are detection capability indices (e.g. probability of detection (POD), false alarm ratio (FAR) and critical success index (CSI)) and frequency based statistics (e.g. root mean square error, bias estimates and correlation coefficients).

Further focus is put on correcting prevailing errors in the rainfall products by adopting linear based (Spatio-temporal) and an additive (Distribution Transformation) bias correction schemes. Bias corrected rainfall estimates are then inter-compared to find the most optimal correction algorithm for the basin.

The Topographic driven model (TOPMODEL) proposed by Beven and Kirkby (1979) is selected for illustrating how errors in the satellite rainfall products impact the basin's water balance closure. Simulation runs were performed based on remote sensing and *in-situ* data. The key model forcing components are Thiessen polygon interpolated rainfall and FAO-56 ET_0 estimates. Daily discharge time series served as model calibration target. The SRTM-90m resolution was used in DEM hydro-processing for calculating topographic index and generating distance to catchment file. The model was then initiated, manually calibrated and validated prior to performing water balance closure analysis. Figure 4.1 summarizes the conceptual framework and research sequence adopted.

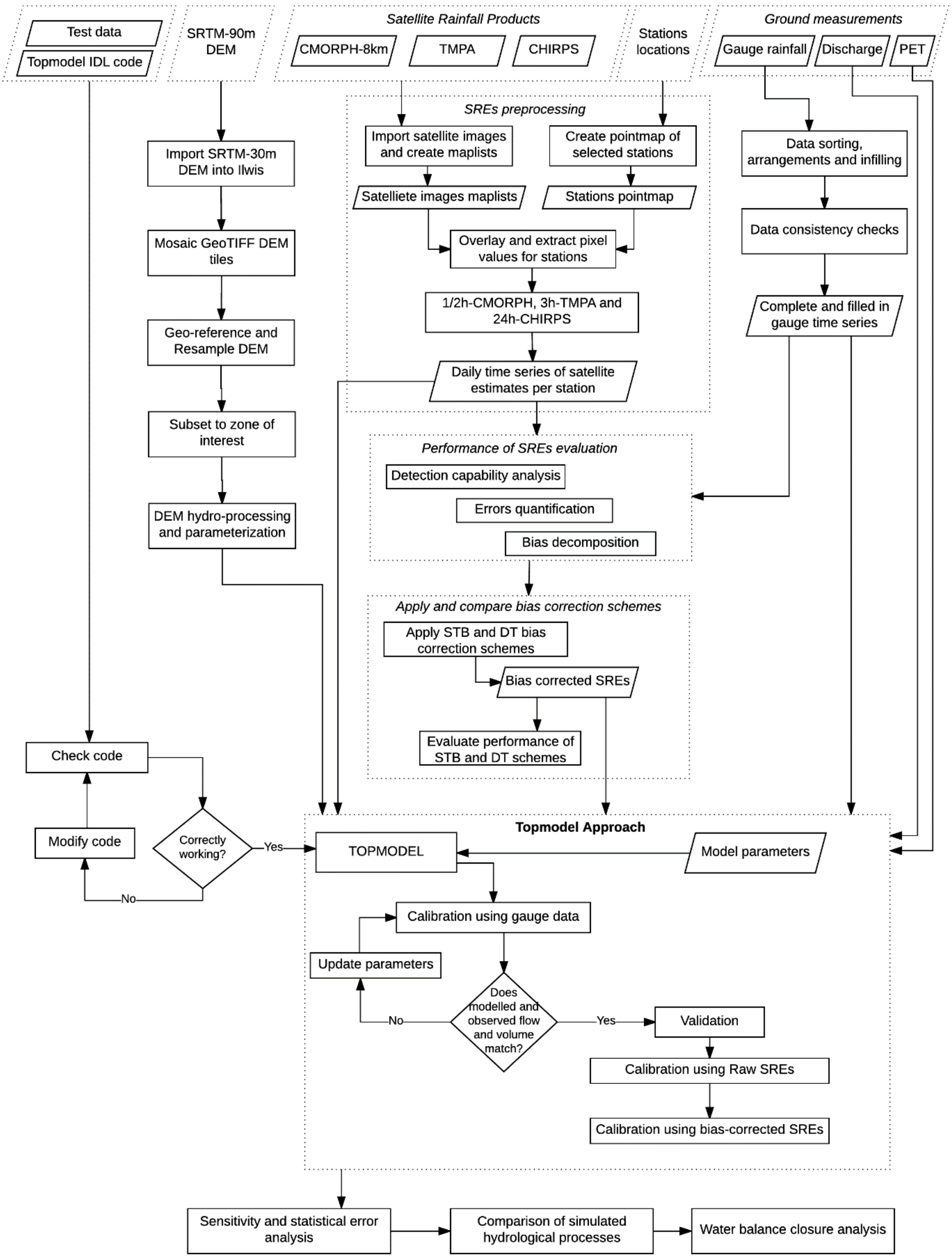

Figure 4.1: Conceptual framework showing the sequence of research process and methodology.

4.2. *In-situ* data processing, completion and quality assessment

4.2.1. Rainfall data

Except for Kabompo, the daily rain gauge data is generally 1998-2013 for all stations. None of the stations have complete rainfall data with Kasempa missing more than 20% of the records as shown in Table 4.1. Available time series are, however, of sufficiently long period allowing assessment of effects of seasons on the satellite rainfall estimates. Furthermore, they overlap with period for SREs evaluated. Missing rainfall records, particularly for Kabompo were therefore completed by fitting a multiple linear regression equation (4.1) (after Michelle, 1997; Rientjes, 2015) to neighbouring stations' records besides using SASCAL WeatherNet information accessible at http://www.sasscalweathernet.org/.

$$P_x = \beta_0 + \sum_{j=1}^{m} \beta_j P_j + \varepsilon \tag{4.1}$$

where P_x is estimated rainfall for x^{th} station, β_0 is a constant, β_j and P_j are regression coefficient and precipitation value for j^{th} station, ε is an error term.

Table 4.1: Inventory of gauge precipitation in Kabompo Basin showing year of data availability and gap analysis.

Station		Coordinates of station		Altitude	Period of data		Gaps	
ID	Name	Lat.	Lon.	[masl]	Start	End	#	%
675430	Kabompo	-1360	+2420	+1075	1/1/1998	30/04/2005	0	0
676410	Kaoma	-1480	+2480	+1213	1/1/1998	30/11/2013	575	9.89
675410	Kasempa	-1353	+2585	+1234	1/1/1998	31/12/2013	1729	29.59
674410	Mwinilunga	-1175	+2443	+1363	1/1/1998	31/12/2013	282	4.83
675510	Solwezi	-1218	+2638	+1386	1/1/1998	31/12/2013	1	0.02
675310	Zambezi	-1353	+2311	+1078	1/1/1998	31/12/2013	122	2.09

For assessing the SREs, collected *in-situ* rainfall records are taken as ground truth, hence adopted without adjustments. Prior to completions, the normal annual rainfall of the stations range between 415.7 to 1313.1 mm, with annual accumulated rainfall reaching 1600 mm as shown in Figure 4.2.

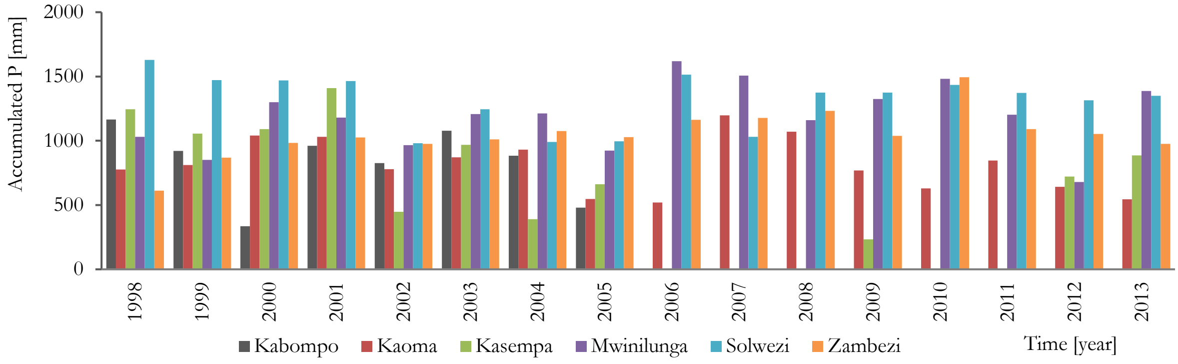

Figure 4.2: Annual rainfall of the meteorological stations for 1998-2013.

4.2.2. Potential evapotranspiration

Daily potential evapotranspiration (ET_0) is determined based on the widely accepted FAO-56 Penman-Monteith method (Allen et al., 1998; Zotarelli et al., 2013). Several gaps, however, exist in meteorological records of relative humidity, air temperature, wind speed and sunshine as illustrated in Table 4.2. These were assessed and data completion done using expectation-maximization (EM) algorithm (Dempster et al., 1977) in SPSS software prior to applying the FAO-56 equation (4.2).

$$ET_0 = \frac{0.408\Delta(R_n - G) + \gamma \frac{900}{T + 273} u_2 (e_s - e_a)}{\Delta + \gamma(1 + 0.34u_2)} \tag{4.2}$$

where ET_0= reference evapotranspiration rate [mm d^{-1}], R_n= net radiation flux at the crop surface [MJ m^{-2} d^{-1}], G= sensible heat flux into the soil [MJ m^{-2} d^{-1}], γ=psychrometric constant [kPa °C^{-1}], T= mean daily air temperature at 2m height [°C], u_2= wind speed at 2m height [m s^{-1}], e_s= saturation vapor pressure [kPa], e_a= actual vapor pressure [kPa], $e_s - e_a$= saturation vapor pressure deficit [kPa], Δ=slope of the saturated vapor pressure curve [kPa °C^{-1}].

Table 4.2: Summary of potential evapotranspiration data gaps for the period 1998-2013.

Station	Missing Gaps (%)		
	Wind speed	Relative Humidity	Temperature
Kabompo	64.9	57.5	58.0
Kaoma	50.4	24.5	77.4
Kasempa	-	82.1	16.3
Mwinilunga	0.5	34.2	9.3
Solwezi	0.3	4.3	37.8
Zambezi	0.2	26.8	3.3

The FAO-56 based ET_0 is evaluated against daily FEWSNET ET_0 at gauge station-level. This remote sensing data was downloaded via ISOD toolbox in ILWIS and subsequently resampled to area of interest. In order to subset the FEWSNET ET_0 product to Kabompo Basin and extract daily ET_0 pixel values from the GDAS grids, projection coordinates of Kabompo Basin in Figure 2.1 were used. Only three stations having at least 60% complete ET_0 variables (i.e. Mwinilunga, Solwezi and Zambezi) were used in validation.

First, time series cumulative curves at the respective stations were visually inspected to help understand any accumulated error in the ET_0 estimates and reveal volumetric agreement between them. Secondly, time series plots were generated to observe deviations from the mean ET_0 calculated. Scatter plots were visually inspected to identify any over or underestimations tendencies from the FEWSNET ET_0 product. Lastly, commonly used performance indices (e.g. mean bias, mean absolute error and root mean square error) were applied to quantify the differences for the period 2008-2012.

The mean bias in equation (4.3), helps evaluate the daily average differences between the FEWSNET and FAO-56 ET_0 time series for the entire 5-years span. The positive and negative differences in the ME may, however, cancel out hence not showing the actual magnitude of over or underestimations. Therefore, mean absolute error in equation (4.4), was applied to obtain the absolute difference between the FEWSNET and FAO-56 ET_0 time series. The root mean square error, equation (4.5), aids in getting a clear picture on the distribution of the differences. For detailed description on these indices, reference is made to (Chai and Draxler, 2014; Rientjes, 2015).

$$ME = \frac{\sum_{i=1}^{n} e_i}{n} \tag{4.3}$$

$$MAE = \frac{\sum_{i=1}^{n} |e_i|}{n} \tag{4.4}$$

$$RMSE = \sqrt{\frac{\sum_{i=1}^{n} {e_i}^2}{n}} \tag{4.5}$$

where e_i represents the differences between FEWSNET and FAO-56 based ET_0 estimates while n is the number of observations.

4.2.3. Screening and correcting spurious discharge data

The observed discharge time series for 1998-2013 were screened and unreliable records corrected. Initially, the hydrograph at Watopa Pontoon gauging station was visually inspected, and some records flagged as suspicious particularly at the onset and end of low flow phases as seen in Figure 4.3. These are, however, of short duration (i.e. less than 2 days). Due to absence of neighbouring gauge observation to aid in correcting the suspicious records, values preceding and succeeding an incorrectly identified record were linearly interpolated to obtain filled in discharge values.

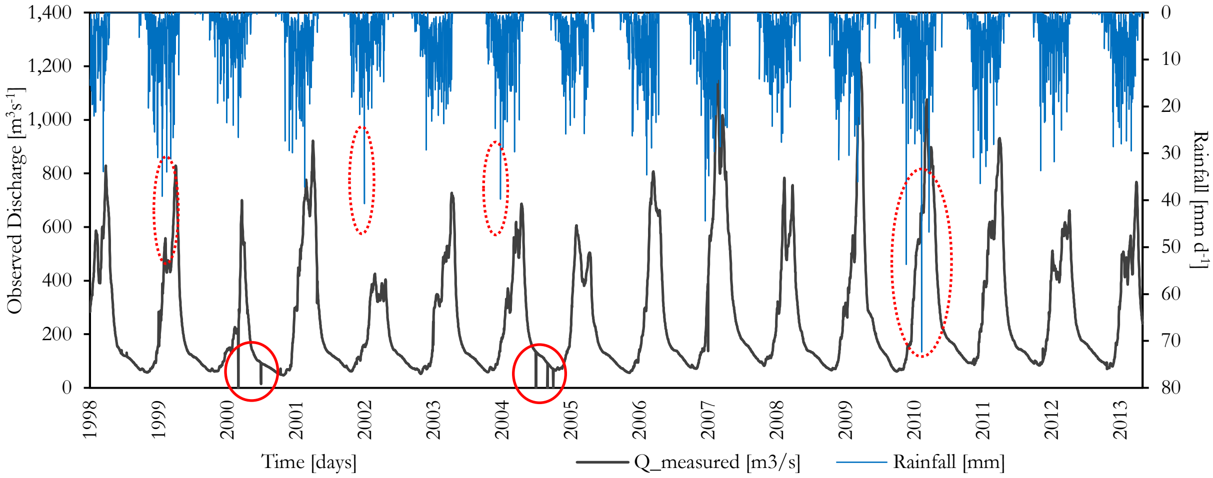

Figure 4.3: Rainfall and observed discharge daily time series (1998-2013) for Kabompo Basin showing spurious recordings and exceptional inconsistencies highlighted.

As highlighted, exceptional inconsistencies between interpolated rainfall and discharge are identified, perhaps sign of either unique events, erroneous data or uncertainties introduced during rainfall spatial interpolation process. These are high peak events in the discharge without coinciding causative rainfall events or high intensity rainfall events without significant response to observed discharge.

The pre-adjusted discharge time series were then checked for accuracy and consistency through comparison with spatially interpolated rainfall besides applying rainfall-discharge double-mass curve analysis (after Searcy & Hardison, 1960) as illustrated in Figure 4.4 (a). The principle applied by double-mass curves is that, by plotting the cumulative rainfall versus corresponding discharge recorded at the same period and station, a consistent slope pattern should result. On visual inspection, a fairly consistent slope pattern is evident.

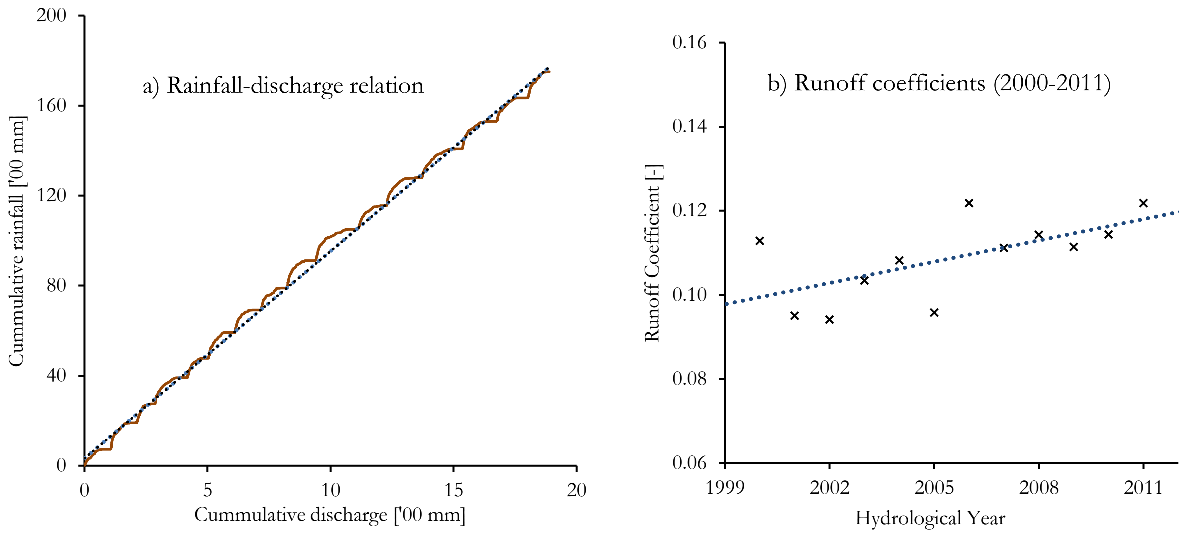

Figure 4.4: Rainfall - discharge relation using double-mass curves [x100 mm] (a) and the basin's runoff responses for 2000-2011 hydrological years (b).

Further investigation of the runoff coefficients (equation (4.6)) at annual base for the period 2000-2011 in Figure 4.4 (b) reveal that on average 10.9% of rainfall received results in runoff production in the basin. This is variable for the hydrological years evaluated at ±1.5% margin and 0.9% standard deviation, perhaps due to catchment heterogeneity and variations in rainstorm characteristics such as intensities, duration and distribution. This low runoff coefficient also implies most of rainwaters in the catchment infiltrates into the soils thus delayed discharge peaks observed. No runoff coefficients' outliers are present.

$$Runoff\ coefficient = \frac{Annual\ measured\ discharge\ [mm]}{Annual\ precipitation\ [mm]} \tag{4.6}$$

As a final procedure in identify individual unreliable discharge measurements during the high rainfall events, incremental differences method was applied (after Rientjes et al., 2011). This involved, calculating the incremental or decremental differences of precipitation (ΔP) and corresponding observed discharge (ΔP) for each time step applying equations (4.7) and (4.8), then plotting the ratio of absolute precipitation differences against corresponding discharge differences, $|\Delta P|/\Delta Q$ for the period 1998-2013.

$$\Delta P = P_t - P_{t-1} \tag{4.7}$$

$$\Delta Q = Q_t - Q_{t-1} \tag{4.8}$$

Most of the $|\Delta Q|/\Delta P$ and $|\Delta P|/\Delta Q$ values lie close to zero while some appear as outliers as demonstrated in Figure 4.5. These were selected, inspected against the rainfall events and appropriately adjusted.

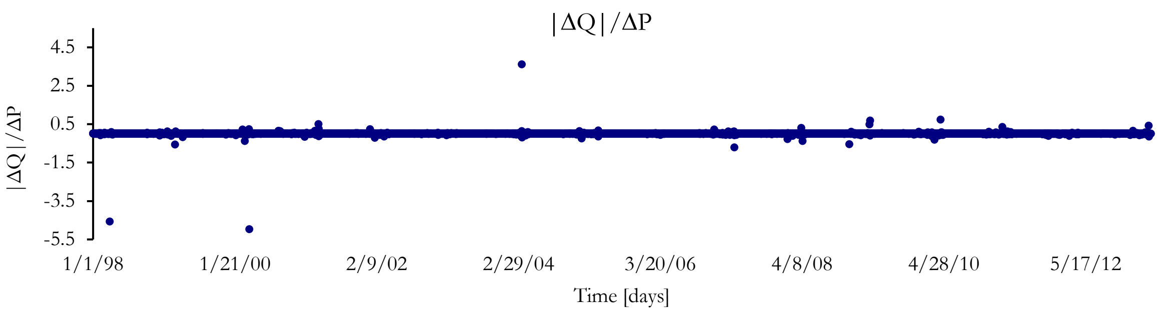

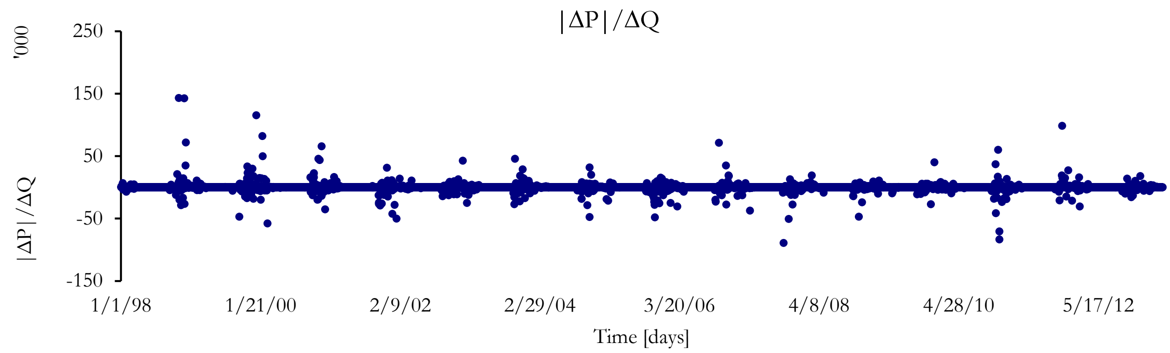

Figure 4.5: Showing the $|\Delta Q|/\Delta P$ and $|\Delta P|/\Delta Q$ ratios during 1998-2013 for Kabompo Basin.

Figure 4.6 shows obtained hydro-meteorological time series in the basin corrected for spurious data. A consistent pattern of dry and wet seasons with base flows occurring in any year is shown. This is an indication of the Kabompo River being a perennial stream.

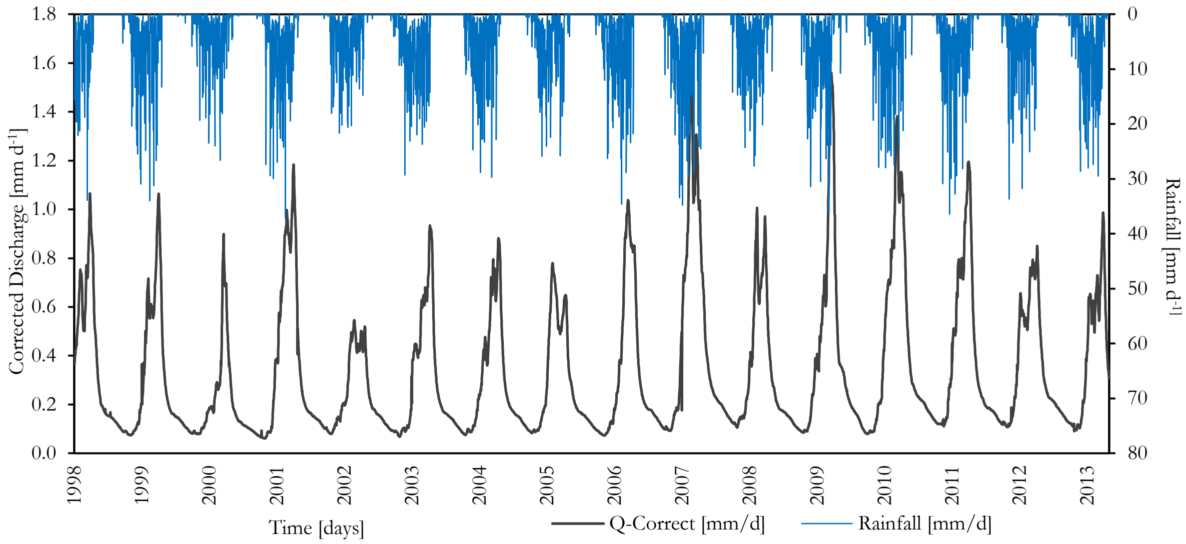

Figure 4.6: Corrected rainfall and discharge time series in Kabompo Basin for 1998-2013.

4.3. Selection of unifying resampling scale and method

Prior to comparing the three satellite rainfall products: ½-h CMORPH, 3h-TMPA and 24h-CHIRPS discussed in section 2.3, they had to be of a uniform scale. Thus, resampling the satellite imageries was crucial. Three resampling techniques discussed in section 3.1, were tested on how best they preserve spatial information contained in the satellite imageries (e.g. pixel values and their averages) when resampled across different spatial scales (i.e. fine scale of 0.05°, 0.07° and coarser 0.25° pixels) for the period 2007-2008.

Each of the interpolation methods were first evaluated based on their ability to reproduce satellite-derived estimates patterns in the basin. Then, the best resulting interpolation method was assessed against the three spatial scales. To assess their accuracies, quantitative metrics such as root mean square error $(RMSE)$, mean bias (MB), Pearson correlation coefficients (r) in equations (4.9) - (4.11) with detailed description in Chai and Draxler (2014), Jagalingam and Hegde (2015) and Yusuf et al., (2013) were used besides computing averages and extreme-values. Qualitatively, scatter plots and graphical representations were visually inspected.

$$MB = \frac{\overline{E_{sat}} - \overline{E_{res}}}{\overline{E_{sat}}} \tag{4.9}$$

$$RMSE = \sqrt{\frac{\sum_{i=1}^{n}(E_{sat} - E_{res})^2}{n}} \tag{4.10}$$

$$r = \frac{\frac{1}{N}\sum_{n-1}^{N}\left(E_{sat,i} - \bar{E}_{sat}\right)\left(E_{res,i} - \bar{E}_{res}\right)}{\sigma_{sat}\sigma_{res}} \tag{4.11}$$

where E_{sat} and E_{res} are satellite and resampled estimates respectively, N is the total number of data elements, while σ_{sat} and σ_{res} are satellite and resampled estimates standard deviations.

In this study, the MB is expressed as a percentage to give the mean difference between the satellite (as reference image) and resampled estimates. An ideal value of 0 is obtained when the two estimates are similar. Similarly, $RMSE$ calculates the variations in the pixels with a value of 0 indicating resampled estimates to be close to their satellite counterparts. And, r indicates similarities between the estimates with 1 as an ideal value.

The investigation was carried out at 24-h, monthly and semi-annual time-steps. Besides, extreme rainfall rates (below 1 mm d^{-1} and above 20 mm d^{-1}), the dry and wet seasons were assessed. Point to pixel method was applied in extracting the satellite estimates used in this procedure.

4.4. Satellite-based rainfall estimates retrieval

Each of the rainfall product imageries were downloaded from their respective archives listed in Table 2.2 via GeoNETCAST ISOD toolbox in ILWIS GIS software available at http://52north.org/downloads. Except for CHIRPS available on daily scale, CMORPH and TMPA data are provided at ½-h and 3-h scales respectively.

Customised ILWIS routines were then incorporated to download ½-h CMORPH rainfall product at 0.07° resolution from ftp site and process it to hourly values. Subsequently, the hourly images were aggregated to daily totals through ILWIS batch processing. This process sequence is summarized in Figure 4.7. Similarly, 3-h TMPA estimates with 0.25° resolution were downloaded, processed to hourly images and then aggregated to daily totals. This is to synchronize with daily accumulation time steps for available gauged rainfall for the period 2008-2012 applied in this study.

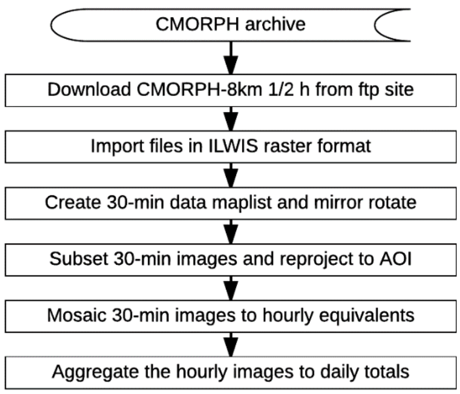

Figure 4.7: Processing sequence for half-hourly CMORPH data at 0.07° scale to daily estimates.

In retrieving daily SREs per pixel corresponding to the 6 rain gauge stations, a maplist of the imported images at daily time steps is generated and subset to area of interest. These images are geometrically corrected and registered to WGS 84 datum with the Universal Transverse Mercator zone 34S projection. To allow for satellite-gauge comparisons, resulting subset datasets are then spatially averaged to uniform space grids (based on section 4.3 results) and overlaid with stations point locations. This gives daily totals [in mm d^{-1}] which is exported to MS Excel for subsequent analysis.

4.5. Evaluation of SREs bias

Existing systematic differences in the satellite rainfall products are calculated by comparing their rainfall estimates with reference to rain gauge observations as data indicating the true rainfall. The reference data is derived from 5 out of 6 stations in the basin for the period 2008-2012. Irrespective of the rainfall products' native grid sizes, they are assessed at daily (24-h) time-step and 0.05° x 0.05° pixels. Daily accumulations are used not only because rain gauge measurements are available at this temporal scale, but also to ensure that random errors cancel out in the process based on Jobard et al. (2011) observation.

The SREs performance in detecting rainfall distribution in the basin is evaluated by clustering daily gauge measurements into 6 rain rate classes (0-1, 1-2.5, 2.5-5, 5-10, 10-20 and above 20 mm d^{-1}). Similarly, their seasonal dynamics in detecting and reproducing salient rainfall features during wet (November – March) and dry (April – October) seasons is assessed.

First, accuracy and precision of the individual products on detecting rainfall events at every station is analysed based on three commonly used detection capability indices: POD, FAR and CSI described in details by Wilks (2006). These indices are computed based on contingency diagram in Figure 4.8 and equations in Table 4.3. POD indicates rainfall occurrence correctly detected and is defined as ratio of false alarm to total number of rainfall non-occurrence. It ranges from 0 to 1, with a perfect score of 1. FAR gives proportion of falsely detected rainfall occurrence by SREs. It ranges from 0 to 1 with a perfect score of 0. CSI measures the fraction of the number of correctly identified precipitation, with best and worst scores of 1 and 0 respectively.

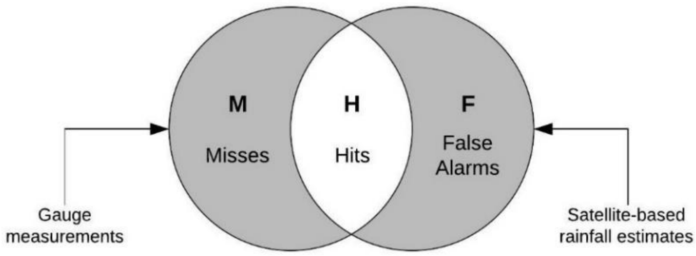

Figure 4.8: Visual representation of contingency diagram based on which detection capability indices are computed.

Table 4.3: Detection capability indices computed for different SREs and seasons.

Statistic	Description	Units
POD	Probability of Detection: Hits/ (Hits + Misses)	[-]
FAR	False Alarm Rate: False Alarm/ (Hits + False Alarm)	[-]
CSI	Critical Success Index: Hit/ (Hit + Misses + False Alarm)	[-]

Errors in the products, when compared with rain gauge observations, in terms of volume and rain depths were then quantified. This was done by calculating standard statistical scores measuring systematic differences (e.g. bias in equation (3.1)), accumulated error (e.g. root mean square error) and degree of linear agreements between the satellite and gauge series (e.g. correlation coefficients) (Haile et al., 2013;

Moazami et al., 2014) expressed in equations (4.12)-(4.15). Graphical summaries of the relative skills (particularly $RMSE$, r and standard deviations) were then generated using Taylor diagrams (Taylor, 2001) to compare how close satellite-based estimates match gauge observations in the basin.

Relative Bias [-]
$$RBias = \frac{\sum_{i=1}^{N}(P_{s,i} - P_{g,i})}{\sum_{i=1}^{N} P_{g,i}} \tag{4.12}$$

Root Mean Square Error [mm d^{-1}]
$$RMSE = \sqrt{\frac{\sum_{i=1}^{n}(P_{s,i} - P_{g,i})^2}{N}} \tag{4.13}$$

Mean Error [%]
$$MB = \frac{\bar{P}_g - \bar{P}_s}{\bar{P}_g} \tag{4.14}$$

Correlation Coefficient [-]
$$r = \frac{\frac{1}{N}\sum_{n-1}^{N}(P_{s,i} - \bar{P}_s)(P_{g,i} - \bar{P}_g)}{\sigma_s \sigma_g} \tag{4.15}$$

where $P_{s,i}$ and $P_{g,i}$ are satellite and gauge based data at day i; N is the total number of data elements; σ_s and σ_g are satellite and gauge data standard deviations; $\bar{P}_s$ and $\bar{P}_g$ are satellite and gauge data mean values.

The range for bias, relative bias, $RMSE$ and MB is $-\infty$ to $+\infty$ with a perfect score of 0 (SREs = gauge-based measurements) while that of r is -1 to $+1$ with a perfect agreement score of 1 (Mashingia et al., 2014).

Lastly, the total bias in the products was decomposed into different sources i.e. hit bias, missed rain and false rain based on equations in Table 3.1 and expressed in mm d^{-1}. This facilitated quantifying amount of water lost or added to water budget from hydrological viewpoint, inter-comparing the rainfall products and gaining deeper knowledge on the sources and nature of their bias.

4.6. Satellite-based rainfall bias correction

This procedure aimed at getting a new set of CMORPH, CHIRPS and TMPA daily estimates adjusted to match rain gauge observations. To achieve this, the respective daily satellite rainfall estimates are multiplied by bias factor estimated through these schemes:

4.6.1. Spatio-temporal bias correction

Here, space-time variant bias factor, BF_{TVSV}, is determined based on 7-day's sequential window approach, proposed by Bhatti et al. (2016). This multiplication factor is only calculated for a certain day when a minimum of 5 mm rainfall accumulation depth and at least 3 rainy days within the preceding 7-days' window is recorded, if not, no bias factor is assigned. Besides, no bias factor is assigned in cases when the gauge either had no records or continuous zero values.

The space-time variant bias factor is then obtained by dividing the sum of the satellite-based estimates and the sum of the gauge observations estimated from equation (4.16).

$$BF_{TVSV} = \frac{\sum_{t=d}^{t=d-l} G(i,t)}{\sum_{t=d}^{t=d-l} S(i,t)} \tag{4.16}$$

where S and G are satellite and gauge based data respectively; i is gauge location; t is julian day number; l is length of a time window for bias correction.

In addition to the space-variant bias scheme, *(i)* time and space fixed, BF_{TFSF}, correcting for all time steps and pixels based on equation (4.17); and *(ii)* time variable, BF_{TvSF}, correcting at daily time step for every pixel based on equation (4.18) are applied.

$$BF_{TFSF} = \frac{\sum_{t=1}^{t=T}\sum_{i=1}^{i=n} G(i,t)}{\sum_{t=1}^{t=T}\sum_{i=1}^{i=n} S(i,t)} \tag{4.17}$$

$$BF_{TvSF} = \frac{\sum_{t=d}^{t=d-1}\sum_{i=1}^{i=n} G(i,t)}{\sum_{t=d}^{t=d-1}\sum_{i=1}^{i=n} S(i,t)} \tag{4.18}$$

4.6.2. Distribution transformation

As described in Gumindoga et al. (2016) but based on 5-day window, the differences in the mean values and statistical variations between SREs and gauge measurements are matched following steps in equations (4.19)-(4.21). First, bias correction factor for the mean, DT_{μ}, is determined based on equation (4.19).

$$DT_{\mu} = \frac{G_{\mu}}{S_{\mu}} \tag{4.19}$$

where G_{μ} and S_{μ} are mean values of 5-day gauge and particular satellite rainfall estimates for stations overlaying gauge locations.

Then, bias correction factor for the variation, is determined by quotient of the 5-day standard deviations for the gauge (G_{τ}) and satellite based rainfall (S_{τ}) following equation (4.20).

$$DT_{\tau} = \frac{G_{\tau}}{S_{\tau}} \tag{4.20}$$

Finally, the correction factors are applied on daily SREs ($S_{i,t}$) to obtain bias corrected satellite estimates S_{DT} using equation (4.21). The formula is modified to ensure retention of uncorrected satellite-based rainfall estimates in cases of negative correction satellite estimates.

$$S_{DT} = DT_{\tau}\left(S_{i,t} - S_{\mu}\right) + DT_{\mu}S_{\tau} \tag{4.21}$$

4.7. DEM hydro-processing and parameterization

The SRTM 90m resolution DEM covering the study area was retrieved from specified source in section 2.5. ISOD toolbox routine incorporated in ILWIS is used in this process where extracted GeoTIFF tiles are transformed into ILWIS raster formats. Prior to DEM hydro-processing (Figure 4.9), the extracted elevation data are mosaiced, sub-mapped to area of interest then resampled and projected in UTM zone 34S with WGS84 datum and 1984 ellipsoid.

Figure 4.10 a) shows the spatial variation of elevation for the Kabompo Basin. The elevation ranges between 1075 m and 1508 m, thus a little variation of ~500 m.

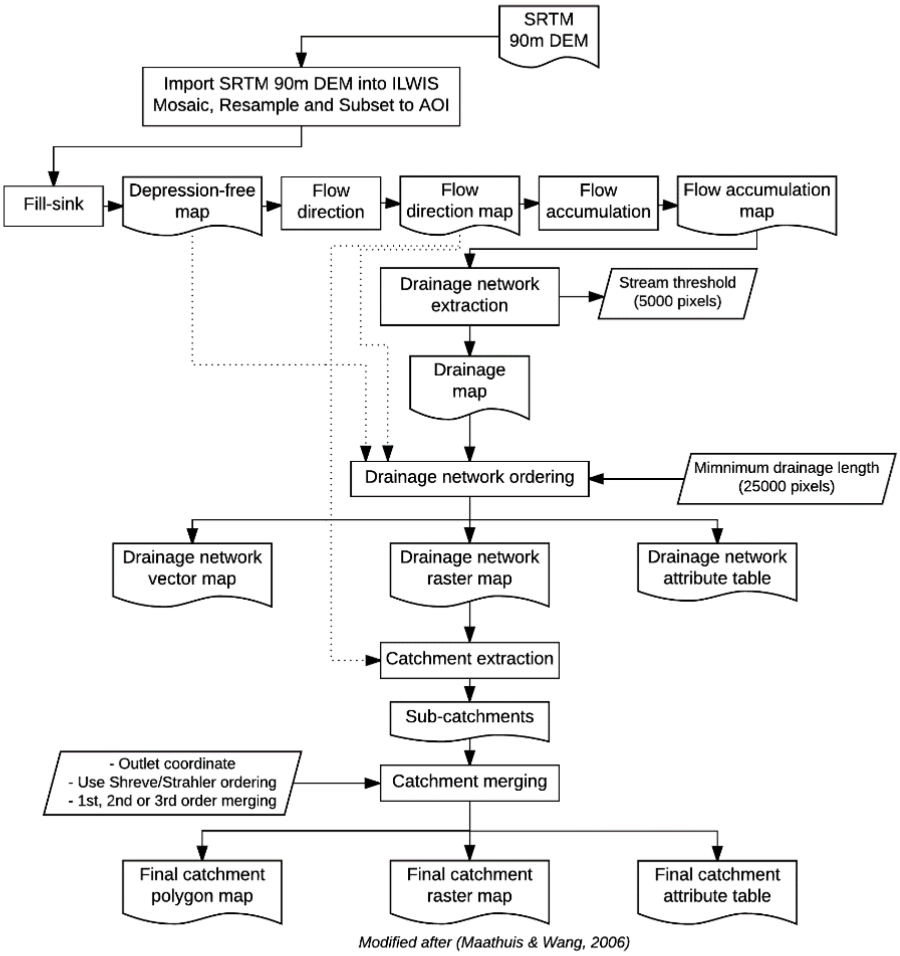

Figure 4.9: Drainage and catchment extraction schematic overview (modified after Maathuis and Wang, 2006).

4.7.1. Flow determination

The downloaded SRTM 90m DEM was useful in delineating drainage area including sub-catchments, extracting drainage network, elevation zoning besides generating topographic index (a key TOPMODEL input). The DEM hydro-processing thus involved: *i)* applying fill-sink operation on digital elevation map (Figure 4.10 a) to remove natural and artificial topographic depressions (Maathuis and Wang, 2006), where truncated streamflow pathways in the DEM domain are removed; *ii)* computing natural flow direction for each cell within the depression-free DEM (Figure 4.10 b) using the Deterministic-8 algorithm; then *iii)* based on the flow directions (Figure 4.10 c), the flow accumulation map (Figure 4.10 d) is calculated to find the drainage pattern of the terrain.

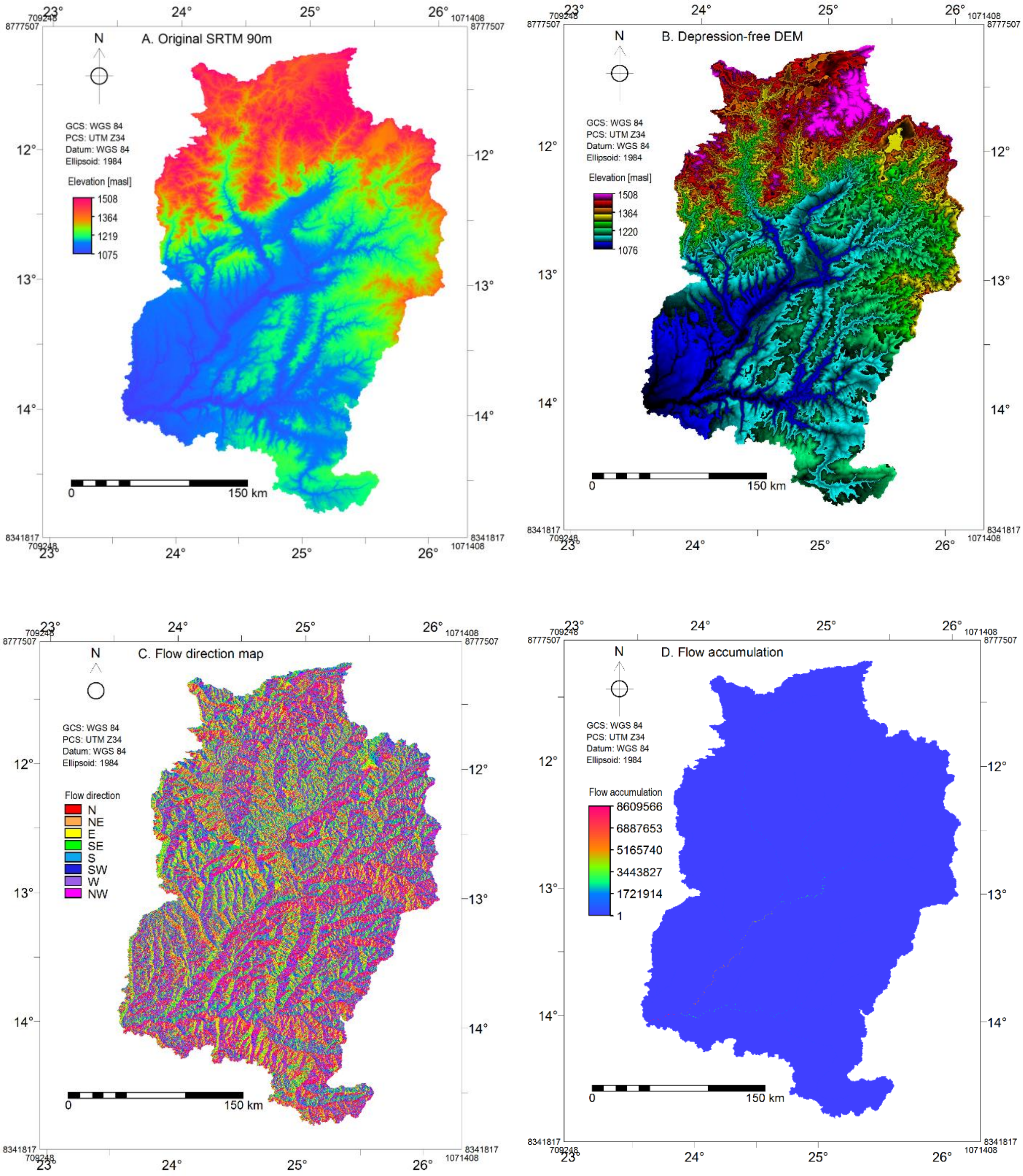

Figure 4.10: Showing original DEM, depression-free DEM, flow direction and accumulation maps.

4.7.2. Drainage network and catchment extraction

Using the flow-determination outputs, drainage network for the study area is extracted through drainage network routine. This routine joins nodes where ≥ 2 streams meet and assigns every stream unique IDs. In this case, the minimum drainage contributing area and drainage length applied are 5000 and 25000 pixels respectively. Thereinafter, sub-catchments are constructed for every stream in the drainage network ordering map. Adjacent sub-catchments are then merged using the basin's outlet location. Figure 4.11 shows extracted drainage network and 5 sub-catchments.

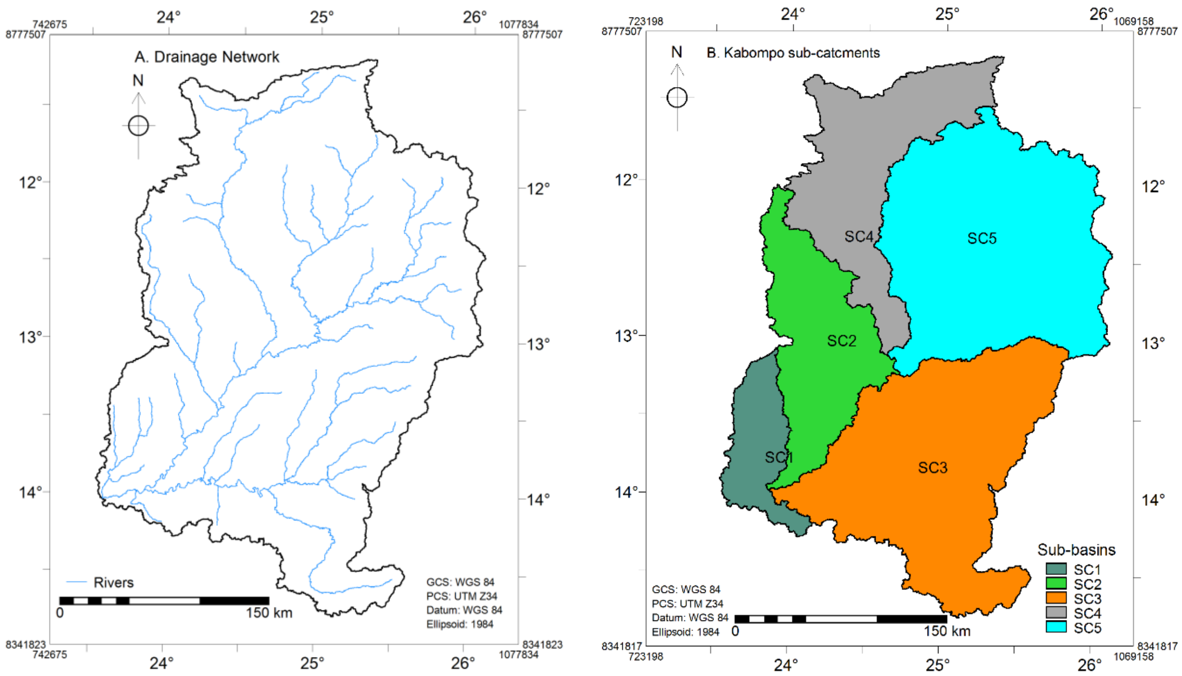

Figure 4.11: Drainage network and sub-basins maps

4.8. TOPMODEL application

An IDL TOPMODEL code modified by Tom Rientjes from WRS department of Faculty ITC, to allow application in a distributed manner is used. This is a conversion of FOTRAN version of TOPMODEL in Beven and Kirkby (1979). This version of code has successfully been applied in Gumindoga et al. (2014), (2011); Muhammed (2012) and Roberto (2011).

Application of this model favours this study because it makes hydrological predictions which are spatially distributed i.e. model parameters, inputs and outputs spatially vary in contrast with lumped HBV model. Unlike MIKE SHE, this model requires low number of parameters to obtain good hydrologic predictions thus relatively simple calibration with minimized optimization problems. Compared with physically based models (e.g. SWAT and MIKE SHE), TOPMODEL is simple and can easily be implemented in computer code. The model readily accepts the use of GIS and remote sensing data (e.g. DEM) as inputs (Gumindoga et al., 2014). Furthermore, it relies on topography which highly influences rainfall-runoff production. As argued by Devia et al. (2015), this model performs well in catchments characterised by shallow soils and undulating terrain.

4.8.1. Spatial interpolation of rainfall distribution and other hydro-meteorological inputs

In water balance assessments, rainfall is a key input. Rainfall records are, however, often incomplete due to several reasons including irregularly spaced gauging stations that restrict their application over large areas. In this study, for instance, the middle of the basin is fairly unrepresented.

To determine which interpolation technique best suit estimating rainfall distribution in the basin, a preliminary test is conducted where a station's rainfall is temporarily assumed unknown, one at a time. The assumed unknown rainfall is then estimated using Thiessen polygon method (Thiessen, 1911) and Inverse Distance Weighting (IDW; Shepard, 1968). In Table 4.4, a brief comparison of these two rainfall interpolation techniques is given. Each of the interpolated rainfall estimates are then cross-validated with practical values recorded at the respective gauges. The daily rainfall record for February 2000 from six irregularly spaced rainfall stations is used.

The accuracy of the spatial interpolation methods is evaluated by combining three regularly employed forecast accuracy measures: root mean square error $(RMSE)$, mean absolute error (MAE) and Pearson's correlation coefficient (r) defined in equations (4.22) - (4.24), further details in Chai and Draxler (2014). Both MAE and $RMSE$ indicate magnitude of extreme errors while r assess whether interpolated rainfall fits observations or not. Besides historical relevance in statistical modelling, the $RMSE$ and MAE are selected since they are dependent on scale of data in use, thus useful when comparing different methods applied to same data set as Hyndman and Koehler (2006) argues. Furthermore, MAE is based on absolute error between the actual and interpolated values, ensuring terms being summed are non-negative, and error accumulates rather than cancel out. $RMSE$ in contrast avoids use of absolute errors, but represents aggregated squared residual errors between quantities compared, hence magnified differentiability.

$$RMSE = \sqrt{\frac{\sum_{i=1}^{n}(\mu_o - \mu_c)^2}{N}} \tag{4.22}$$

$$MAE = \frac{1}{N}\sum_{i=1}^{N}|\mu_o - \mu_c| \tag{4.23}$$

$$r = \frac{\frac{1}{N}\sum_{t-1}^{N}(\mu_o - \overline{\mu_o})(\mu_c - \overline{\mu_c})}{\sigma_{\mu_o}\sigma_{\mu_c}} \tag{4.24}$$

where N is the number of rain events, μ_o and μ_c represents the observed and corresponding interpolated rainfall depths at a time i, $\overline{\mu_o}$ and $\overline{\mu_c}$ are the mean values for observed and interpolated data, while σ_{μ_o} and σ_{μ_c} are the observed and interpolated data standard deviations.

Table 4.4: A comparison of two rainfall interpolation methods.

Method	Thiessen polygons (nearest neighbor)	Inverse distance weighting (moving averages)
Reference	(Thiessen, 1911)	(Shepard, 1968)
Transitions	Abrupt	Gradual
Limitations	No error assessments, only a single data point per polygon, thiessen polygon patterns formed depend on distribution of data.	No error assessments, results highly depend on size of search window and weighting parameter chosen.
Best for	Nominal data from point observations	Quick interpolation from sparse data on regular grid or irregularly spaced samples
Assumptions	Best local predictor is nearest data point	Underlying surface is smooth

The Thiessen polygon method assumes that the average rainfall value over the same Thiessen polygon area is equivalent to point value located at the centroid of the polygon. To form the polygons, the adjacent stations are connected and each side of the connecting lines vertically bisected. Areal average rainfall is then computed by weighting each station with their corresponding polygon area applying equation (4.25) (after De Silva et al., 2016).

$$P_x = \frac{\sum_{i=1}^{N}[(A_j - A_i)P_i]}{\sum_{i=1}^{N}(A_j - A_i)} \tag{4.25}$$

where $\sum_{i=1}^{N}(A_j - A_i)$ is Thiessen polygon area for the station with missing values, A_j and A_i are Thiessen polygon area when stations with missing values are excluded and included respectively, P_i is annual precipitation of adjacent stations and P_x is estimated rainfall for the station missing observations.

The IDW interpolated rainfall estimates are calculated based on values at neighbouring stations weighted by distance from the interpolation station. This method assumes that each observed nearby station has a local influence that diminishes with distance i.e. the weighting is a function of inverse distance. Thus, the estimated rainfall at unknown site is a weighted sum of rainfall values at N nearby sites. This estimated rainfall using IDW, P_x is then defined by equation (4.26) modified after Noori et al. (2014).

$$P_x = \frac{\sum_{i=1}^{N} P_i d_i^{-\propto}}{\sum_{i=1}^{N} d_i^{-\propto}} \tag{4.26}$$

where P_x and P_i is the unknown and known rainfall data respectively, N is the number of surrounding stations, d_i is the distance from each rainfall stations to the location rainfall is being estimated, α is the power/ control parameter.

For preparing the forcing ASCII file for TOPMODEL application, Thiessen interpolated rainfall, ET_0 estimates based on standardized FAO-56 Penman Monteith ET_0 method (Zotarelli et al., 2013) and corrected discharge time series as calibration target discussed in section 4.2 are used.

4.8.2. The topographic index

The topographic index map is calculated using the DEM hydro-processing products. As a key TOPMODEL input file, the topographic index ($ln(a/tan\beta$), aids in approximating likely local zones of saturation for runoff production. Where, a is the specific discharge contributing area (in this case a=flow accumulation map x 90m grid resolution) and $tan\beta$ is the local topographic gradient (description after Quinn et al., 1995).

The topographic index values range between 9 and 32 with most areas having TI values of 12, 13, 14 and 15 and fractional area contribution of 11%, 21%, 33% and 13% respectively. Highest frequency of the pixels has topographic index of 13 as illustrated in Figure 4.12. Regions along streams are found to be associated with high topographic indices (≥27) implying zones of saturation thus potential subsurface or surface contributing areas. Comparatively, northern regions are predominantly having lower TI values (≤10) qualifying as runoff contributing areas.

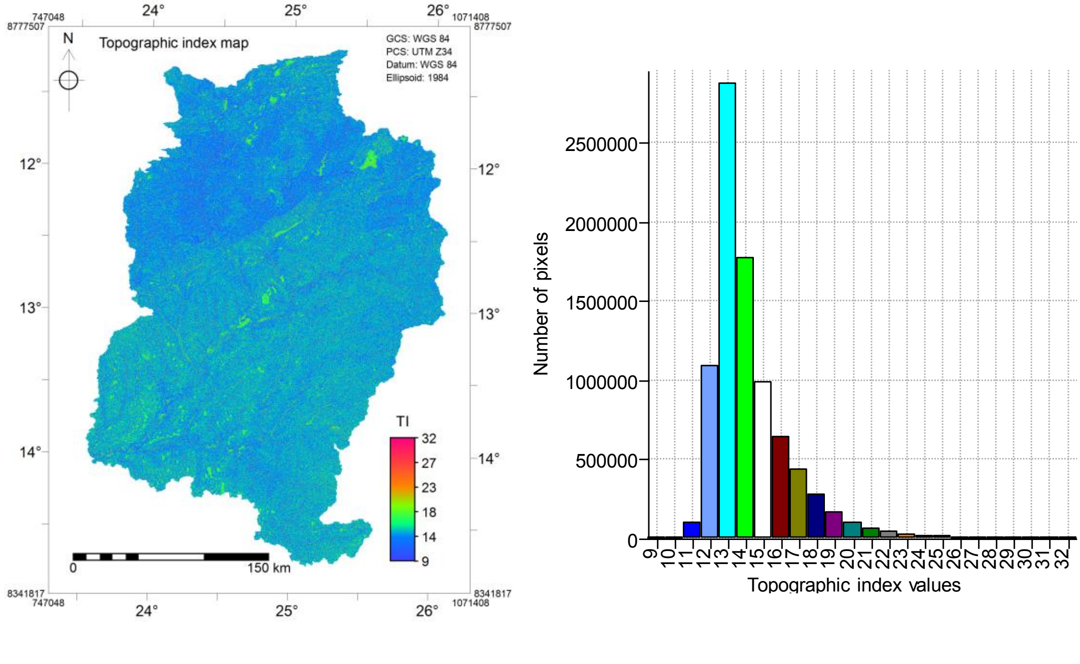

Figure 4.12: Topographic index map (left) and frequency distribution of the topographic index values (right).

4.8.3. Channel network routing

Selecting discharge gauging point as catchment outlet, the catchment is sub-divided into 16 area-distance classes as shown in Figure 4.13, through ILWIS slicing procedure. This aids defining the time any water droplet, travelling in a straight-line distance, would take to reach the catchment outlet. In reality, water droplets travel time varies for sub-basins; in the model, however, routing of surface flow is done by use of distance-related delay (Gumindoga et al., 2014, 2011; Muhammed, 2012). Then, any water falling within the same sliced distance is assumed to reach the outlet with equal travel time interval. Furthest fractional area from the catchment outlet determined is 379 km – straight line distance.

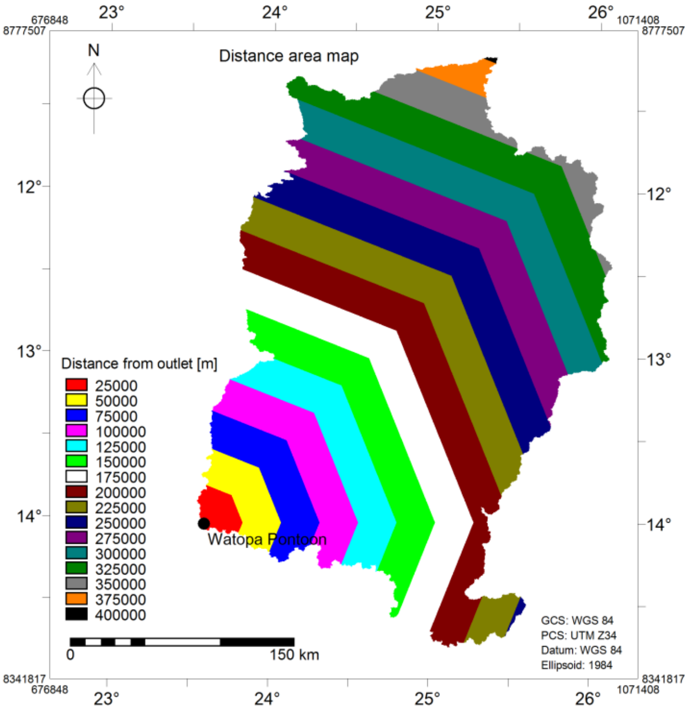

Figure 4.13: Area-distance map for channel routing in the Kabompo basin.

4.8.4. Model parameterization, sensitivity analysis and validation

The model was initialized, calibrated and validated by use of *in-situ* data before forcing it with bias corrected satellite rainfall estimates. The warm up period was from Sept. 2009 – Aug. 2010 whereas calibration covered the period Sept. 2009 through Sept. 2012. At calibration, the selection of first parameter values was done based on knowledge of sensitive model parameters from literature (e.g. Beven and Freer, 2001; Gumindoga et al., 2011) and best fits of simulated and observed hydrographs.

In the calibration process, model parameters in Table 3.2 were manually optimized through a 'trial and error' optimization procedure. This involved, changing only the value of a single parameter at each model run. Baseflow recessions were first fitted, then peak flows of the simulated and observed hydrographs. Focus was then shifted on adjusting the rising limb, timing of the peak flows and streamflow volume to closely match target hydrograph. The model was then meteorologically forced with a different set of *in-situ* rainfall and evaporation data for the hydrological year 2007 to test and validate the optimal parameter sets.

Performance of the model is graphically (through visual inspection of simulated hydrograph) and numerically analyzed using Nash-Sutcliffe coefficient of efficiency, R^2 (Nash and Sutcliffe, 1970) in equation (4.27) and Relative Volume Error, RV_E (Janssen and Heuberger, 1995) in equation (4.28). R^2 is for 'goodness-of-fit' assessment while RV_E is for mass balance checks. As indicated in Nash and Sutcliffe

(1970), R^2 value of 1 shows a perfect simulation of observed discharge. Any value between 1.0 - 0.9, 0.9 - 0.8, and 0.8 - 0.6 respectively signifies that the model performs extremely well, very well or reasonably, respectively. RV_E ranges from $-\infty$ to $+\infty$ with perfect value of 0 indicating model generating no differences between simulated and observed discharge volume. A well and reasonable model performance is indicated by RV_E of -5 to $+5$ and -10 to $+10$ respectively (Rientjes, 2015).

$$R^2 = 1 - \frac{\sum_{n-1}^{N}(Q_{obs} - Q_{sim})^2}{\sum_{n-1}^{N}(Q_{obs} - \bar{Q})^2} \quad (4.27)$$

$$RV_E = \left(\frac{\sum_{i=1}^{n} Q_{sim(i)} - \sum_{i=1}^{n} Q_{obs(i)}}{\sum_{i=1}^{n} Q_{obs(i)}}\right) x100 \quad (4.28)$$

where i is the time step, N is the total number of time steps, Q_{sim} and Q_{obs} the simulated and observed discharges at the n^{th} time interval respectively, $\bar{Q}$ mean value of observed runoff over the calibration period.

To further assess model sensitivity, three most sensitive parameters were selected: soil hydraulic conductivity decay (m), soil transmissivity at saturation (T_0) and root zone available water capacity (SR_{max}). Knowledge of most sensitive model parameters was obtained from literature (e.g. Beven and Freer, 2001; Beven and Kirkby, 1979; Gumindoga et al., 2011). This was done by varying each chosen parameter across its range while keeping the values of the other parameters constant, and results graphed for analysis.

5. RESULTS AND DISCUSSION

5.1. In-situ potential evapotranspiration validation

Here, utility of FEWSNET potential evapotranspiration (ET_0) product is evaluated. As mentioned in section 4.2.3, the comparison is at daily base for three stations having at least 60% complete observation records for the period 2008-2012.

As shown in Figure 5.1, the FEWSNET ET_0 has consistent lower estimates than counterparts by FAO-56 ET_0 estimates by *in-situ* data. This underestimation goes up to a daily high of 0.74 mm (Table 5.1). Similar pattern is portrayed on visualizing the agreement between the daily estimates at station level using scatter plots e.g. in Figure 5.2, where higher FAO-56 ET_0 estimates remain unreported by FEWSNET ET_0 product. Particular for extreme low and high ET_0 estimates, scatter plots show a noisy-pattern implying pronounced variations between FEWSNET and FAO-56 ET_0 estimates.

FEWSNET ET_0 time series show a number of erratic events that cause inconsistencies in the time series pattern. A close volumetric coherence between FEWSNET and FAO-56 ET_0 estimates is seen at Mwinilunga meteorological station. This, however, deteriorates at the other two stations considered, where an increasing accumulated difference between FEWSNET and FAO-56 ET_0 estimates is exhibited. This gap steadily widens with time as shown in Figure 5.2 mass-curve plots. The magnitude of this accumulated error is estimated to range between 1.16 to 1.43 mm with daily average differences going up to 1.12 mm. Graphical representations for the remaining stations are given in Appendix A and Appendix B.

Thus, based on the above-mentioned results, and focusing on reducing the influence of reported ET_0 under-estimations in rainfall-runoff simulations, ET_0 estimates based on FAO-56 Penman Monteith method is selected. Furthermore, the use of FEWSNET ET_0 estimates as meteorological forcing in TOPMODEL simulation would require an upfront removal of existing bias.

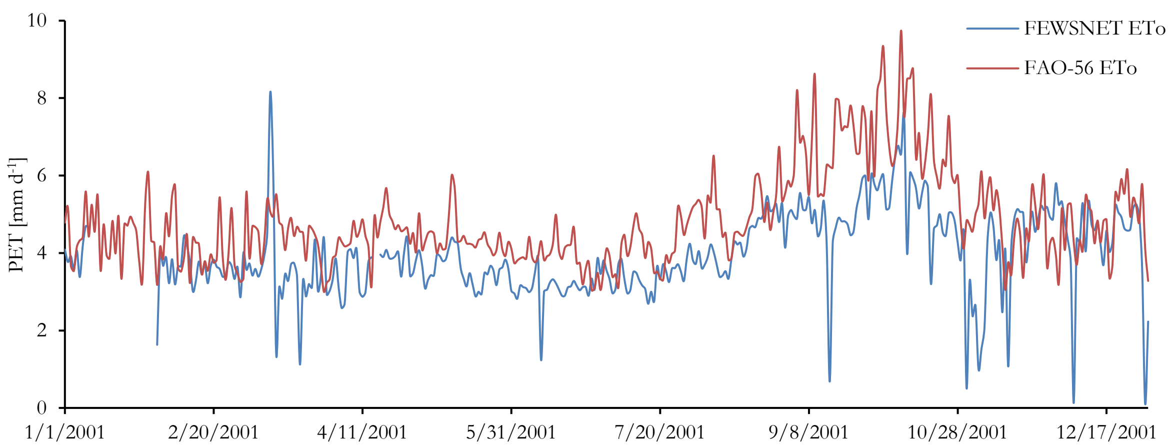

Figure 5.1: Daily variation of FEWNET and FAO-56 ET_0 estimates at Zambezi station in 2001.

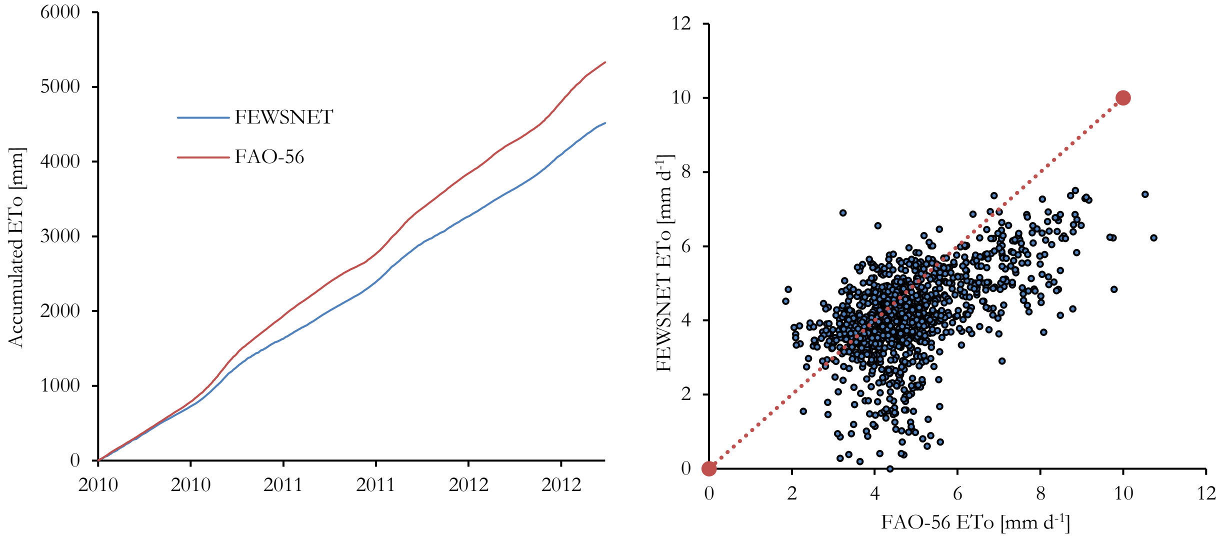

Figure 5.2: Cumulative plots for daily FEWSNET and FAO-56 ET_0 (left panel) and scatter plot (right panel) for the period 2008-2012 at Solwezi station.

Table 5.1: Statistical evaluation indices of FEWSNET ET_o using FAO-56 ET_0 as reference for the period 2008-2012.

	Mwinilunga	Solwezi	Zambezi
ME [mm d^{-1}]	-0.03	-0.74	0.13
MAE [mm d^{-1}]	0.87	1.09	1.12
RMSE [mm d^{-1}]	1.16	1.43	1.42

5.2. Evaluating the accuracy of rainfall spatial interpolation

From Table 5.2, it is evident that both Thiessen polygon and inverse distance weighting (IDW) interpolation techniques could not match the daily averages and accumulated monthly rainfall for all the tested stations. Except for Kasempa, IDW shows consistent lower accumulated rainfall than Thiessen polygon method that only had underestimations at Zambezi and Solwezi stations.

Table 5.2: Evaluation descriptive statistics for Thiessen polygon and IDW interpolation methods for daily rainfall analysed at 5 different test locations.

Evaluation coefficients	Kabompo	Zambezi	Kaoma	Kasempa	Solwezi
Inverse Distance Weighting (IDW)					
Total [mm]	205.9	187.9	196.3	244.7	164.6
Average [mm d^{-1}]	7.1	6.5	6.8	8.4	5.7
RMSE [mm]	10.5	16.2	14.7	14.0	13.4
MAE [mm]	7.1	10.6	8.4	9.0	7.4
Pearson r [-]	0.39	0.01	0.16	-0.03	0.17
Thiessen polygon					
Total [mm]	239.0	221.4	221.4	244.7	175.8
Average [mm d^{-1}]	8.2	7.6	7.6	8.4	6.1
RMSE [mm]	16.4	16.4	15.9	14.0	14.0
MAE [mm]	9.8	9.8	10.2	9.0	9.0
Pearson r [-]	0.31	0.50	0.30	0.75	-0.26
Gauge (reference) measurements					
Total [mm]	221.4	239.0	220.3	175.8	244.7
Average [mm d^{-1}]	7.6	8.2	7.6	6.1	8.4

Correlating analysis on the spatially interpolated rainfall and their observed counterparts at the stations indicate that Thiessen polygon exhibited a better agreement than IDW, with Pearson's correlation coefficients between 0.26 and 0.75. Though IDW outperformed Thiessen polygon in giving lower estimate errors, the Thiessen's magnitude of deviations from the monthly accumulated values and daily averages are relatively less. At Kasempa, both methods had similar performance with exception of r values.

Thiessen polygon method was therefore adopted because of the above findings and showing a relatively good fit for estimating daily averages and accumulated rainfall in the basin. Furthermore, among other rainfall interpolation techniques, Thiessen polygon method considers sparse distribution of stations, and estimates rainfall contribution from adjacent stations without considering missing observations. This minimizes error propagation that may result from rainfall data completion.

As an illustration, Figure 5.3 shows results obtained when IDW and Thiessen polygon methods are used to interpolated 18/02/2000 rainfall; while Table 5.3 summarises individual station's contribution to areal rainfall estimates.

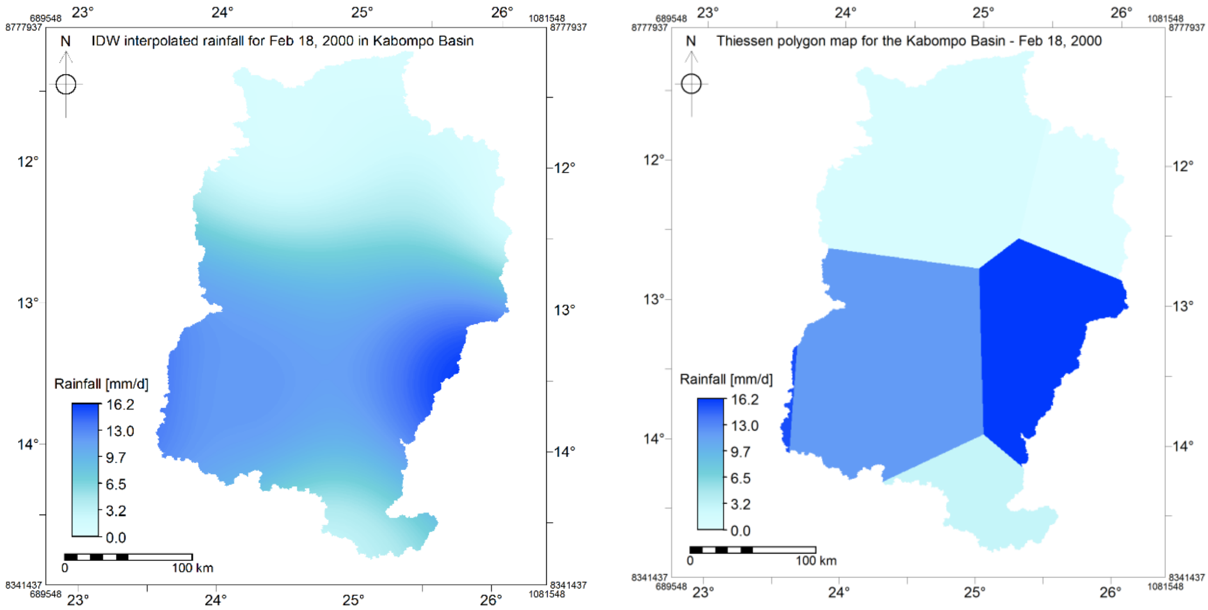

Figure 5.3: Areal rainfall distribution in the Kabompo Basin for February 18, 2000 based on Inverse Distance Weighting (left) and Thiessen polygon techniques (right).

Table 5.3: Individual stations Thiessen factor in determining basin's areal rainfall estimates.

Station	Area [km²]	Thiessen weight
Kabompo	22,480	0.3224
Kaoma	5,636	0.0808
Mwinilunga	22,168	0.3179
Solwezi	7,126	0.1022
Kasempa	12,016	0.1723
Zambezi	311	0.0045

5.3. Comparison of SREs resampling techniques across diffrent interpolating scales

When daily TMPA and CMORPH rainfall rates are interpolated using bicubic method, negative values are noticeably introduced at all the three spatial scales for every site considered. These negatives are as high as

2.08 mm d^{-1} and cancel out at monthly and semi-annual scales, but not at seasonal event and extreme events analysis. Conforming to ESRI (2016), the negative pixel values arise from bicubic extrapolating rainfall rates outside the input value range when fitting a smooth curve to a local window having extremely varying values across small distances. Such a phenomenon can however be avoided by restricting interpolation data range during resampling process in ILWIS GIS software. In Figure 5.4, scatter plots between satellite estimates prior to resampling (at their respective spatial grids) and interpolated estimates based on the three tested methods are shown.

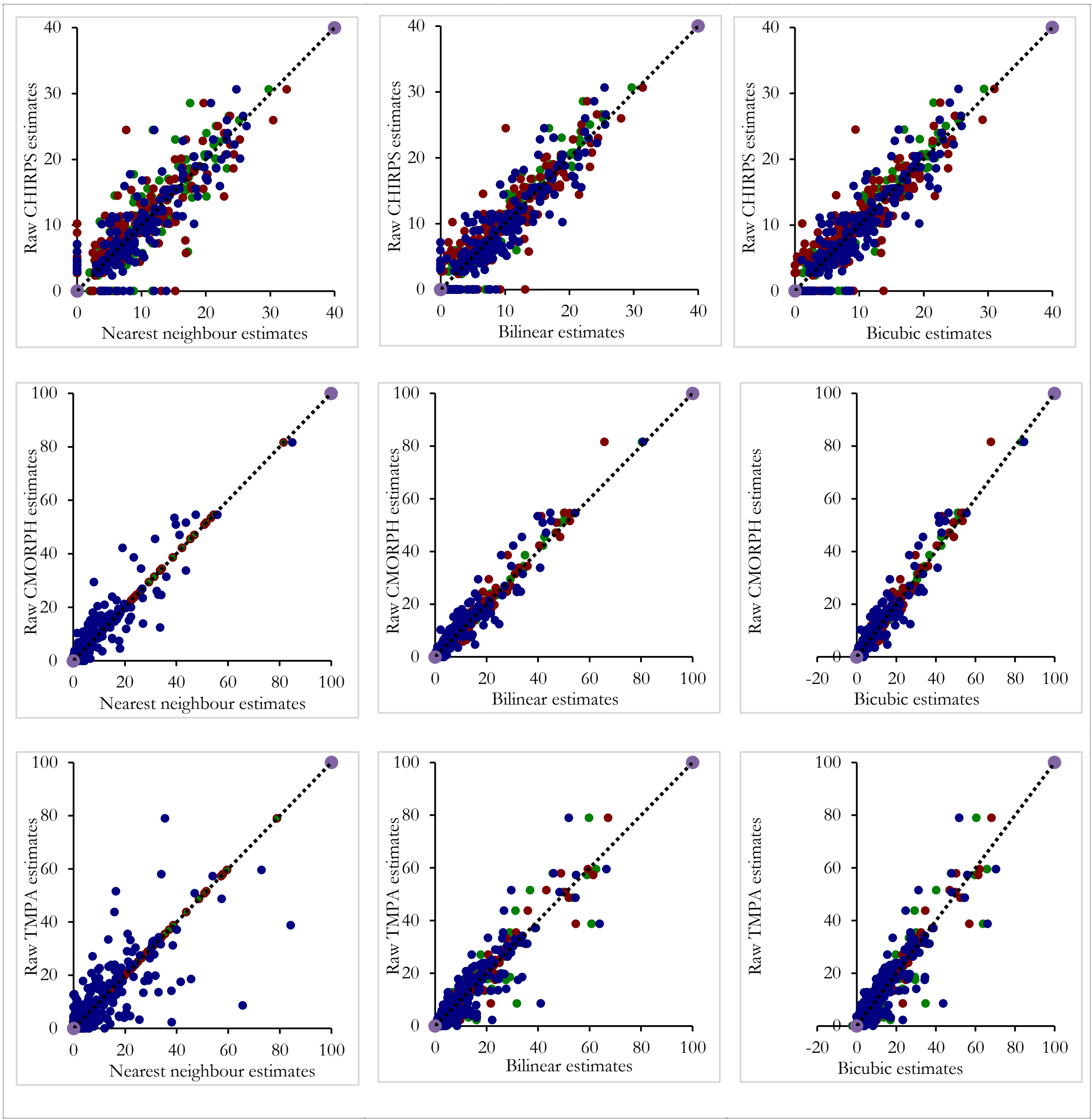

Figure 5.4: Scatter plots of uncorrected CHIRPS, CMORPH and TMPA estimates versus nearest neighbour, bilinear and bicubic resampled estimates at 0.05° (green), 0.07° (red) and 0.25° (blue) grid sizes at Zambezi station (2007-2008).

Unlike nearest neighbour, both bilinear and bicubic interpolations had difficulties in reproducing the daily and monthly maximum TMPA- and CMORPH-pixel values in the basin (example in Appendix C). At least half of the tested sites reportedly had their maxima satellite-estimates underestimated, with bilinear method that performs poorest. When 0.07° grid size was used, nearest neighbour only had a single count of inaccurate interpolation of monthly maximum TMPA-estimates.

On applying nearest neighbour interpolation at 0.05° and 0.07° grid sizes, a plausible pattern for daily and monthly maximum CHIRPS-estimates is reproduced for one third of the tested sites. Again, investigating daily averages and accumulated CHIRPS-interpolated estimates based on nearest neighbour at 0.05° and 0.07° grids, a fair match is observed while the other two methods show inconsistencies for at least half of the test sites. The corresponding root mean squares, mean bias and coefficients of variation are as shown in Table 5.4. In most cases, interpolating satellite estimates at 0.05° and 0.25° using the two latter methods revealed consistent under-estimations, whereas for grid sizes of 0.07° over-estimates for half of the tested sites is shown.

Table 5.4: Minimum and maximum evaluation indices based on daily time-step assessment.

Minimum evaluation scores										
Resampling method		Nearest Neighbor			Bilinear			Bicubic		
Applied grid size [km]		5	8	25	5	8	25	5	8	25
TMPA	RMSE [mm d^{-1}]	0.00	0.00	5.27	1.82	1.53	3.66	1.88	1.58	3.93
	Coef. Of Variation [-]	2.27	2.27	2.20	2.13	2.14	2.11	2.21	2.22	2.18
	Mean bias [%]	0.00	0.00	-8.41	-3.08	-2.76	-6.13	-3.20	-2.47	-6.55
CHIRPS	RMSE [mm d^{-1}]	6.41	6.68	6.53	6.46	6.64	6.50	6.52	6.68	6.54
	Coef. Of Variation [-]	1.69	1.72	1.65	1.65	1.65	1.64	1.67	1.67	1.65
	Mean bias [%]	-0.64	-1.82	-3.04	-0.50	-0.97	-3.49	-0.78	-1.28	-3.69
CMORP.	RMSE [mm d^{-1}]	5.02	5.02	5.46	5.04	4.90	5.50	5.09	4.94	5.61
	Coef. Of Variation [-]	2.46	2.46	2.45	2.43	2.43	2.39	2.45	2.45	2.42
	Mean bias [%]	0.00	0.00	-12.93	-2.18	-2.38	-12.80	-2.23	-2.53	-13.86
Maximum evaluation scores										
TMPA	RMSE [mm d^{-1}]	9.92	9.92	9.92	9.70	9.80	9.42	9.90	9.91	9.65
	Coef. Of Variation [-]	2.56	2.56	2.54	2.43	2.46	2.42	2.53	2.54	2.51
	Mean bias [%]	0.00	0.00	0.00	1.15	0.93	1.15	1.34	1.24	1.34
CHIRPS	RMSE [mm d^{-1}]	8.44	8.48	8.25	8.34	8.31	8.21	8.41	8.38	8.26
	Coef. Of Variation [-]	2.18	2.17	2.18	2.15	2.15	2.15	2.16	2.16	2.16
	Mean bias [%]	3.94	1.50	3.94	2.55	1.26	2.55	2.67	1.07	2.67
CMORP.	RMSE [mm d^{-1}]	9.69	9.63	9.95	9.68	9.57	9.70	9.72	9.61	9.83
	Coef. Of Variation [-]	2.95	2.95	2.93	2.91	2.83	2.86	2.93	2.87	2.89
	Mean bias [%]	0.00	0.61	5.76	0.84	2.18	4.53	0.23	1.36	3.84

For 4 out of 6 tested sites, a consistent over-estimation of daily and monthly TMPA and CHIRPS pixel average values is shown by bilinear, bicubic interpolations – for all the three spatial resolutions and on few cases nearest neighbour when 0.25° grid size is used. Overall, interpolations based on 0.25° grid sizes exhibited the largest mean variations ranging between +25.58% to -26.25% over the wet seasons as expressed in Figure 5.5 and Appendix D.

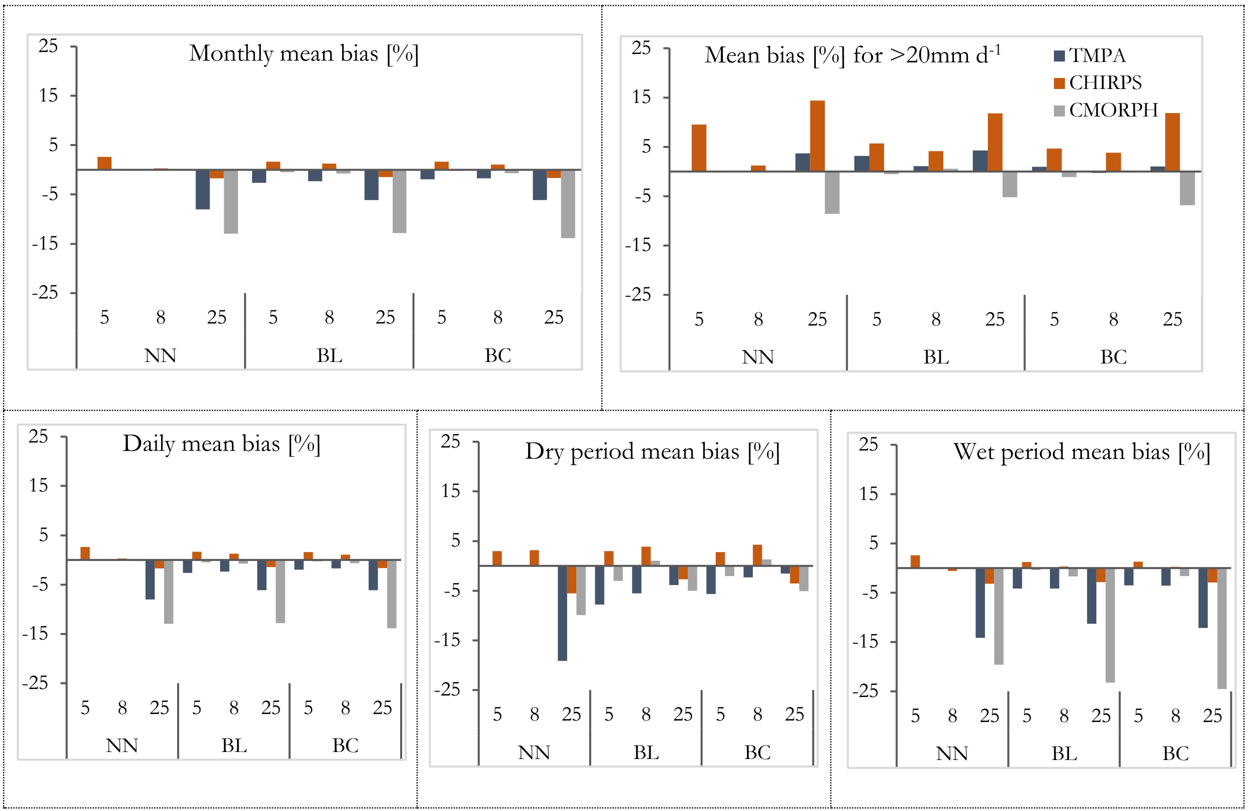

NN: Nearest Neighbour; BL: Bilinear; BC: Bicubic resampling methods

Figure 5.5: Respective interpolation methods' mean bias expressed as a percentage of satellite estimates in the basin at daily, dry and wet seasons and extreme rainfall occurrence at Kabompo station at 0.05°, 0.07° and 0.25° grid sizes.

Further investigations reveal that up to 83% counts of the daily accumulated TMPA-estimates are over-estimated, mainly from bilinear and bicubic interpolations. Similarly, 4 out of 6 tested sites show an over-estimation of monthly TMPA-accumulations from the two methods. However, there are a few cases of nearest neighbour over-estimating daily and monthly TMPA-accumulated estimates, but only when 0.25° grid size is used. Notwithstanding that nearest neighbour interpolation at either 0.05° or 0.07° grids sufficiently reproduces TMPA daily estimates with accumulated error ranging from 0 to 9.92 mm d^{-1} and relative standard deviation of 2.27 to 2.56 expressed as a ratio of the mean pixel values as shown in Table 5.4. Improved coefficient of variations resulted when evaluations are based on monthly time-steps to as low as 0.04 from daily high of 2.95.

On assessments based on dry and wet seasons, nearest neighbour interpolation at 0.05° and 0.07° grids exceptionally simulates the daily maximum, averages and accumulated TMPA- and CMORPH-pixel values for all the test sites, except for a single count. However, this is accompanied by varying mean bias errors up to + or - 26% and -24.54% for dry and wet spells respectively. Unclear seasonal patterns are portrayed by bilinear and bicubic interpolations in representing satellite-information. Compared to the other methods, nearest neighbour show a good match in reporting the extreme low and high TMPA and CMORPH rainfall rates. A few variations are however noticed on CHIRPS-rain rates when interpolated at 0.07° grid sizes.

For this application, then, interpolating the satellite-pixel values at either 0.05° or 0.07° grids and applying nearest neighbour method was found suitable. Comparatively, CHIRPS pixel values are better represented when interpolated at 0.07° grid sizes. Generally, interpolations at 0.05° conserves satellites' pixel information better than 0.07° grids. Coupled with the desire to have the selected grid size of the datasets fine enough to represent daily rain rates distributions for hydrological response simulations in the basin, nearest neighbour resampling technique at unifying spatial scale of 0.05° is thus selected.

5.4. Satellite-based rainfall bias analysis and comparison

Figure 5.6 shows annual accumulated rainfall (2008-2012) for CMORPH, TMPA and CHIRPS versus *in-situ* rainfall with stations that are ordered according to elevation. It is noted that station observations represent point scale observations by the size of the gauge funnel whereas SREs are pixel estimates for pixels that overlay the respective rain gauges. Findings indicate no clear relationship between accumulated rainfall measured at the stations and elevation. Perhaps due to insignificant elevation differences among the stations considered i.e. less than 310 m. As shown, TMPA consistently surpassed gauge rainfall accumulations unlike CMORPH that exhibits a consistent underestimation of mean annual rainfall at every station. Except for Kasempa, CHIRPS also underestimate gauge rainfall accumulations but outperforms CMORPH product.

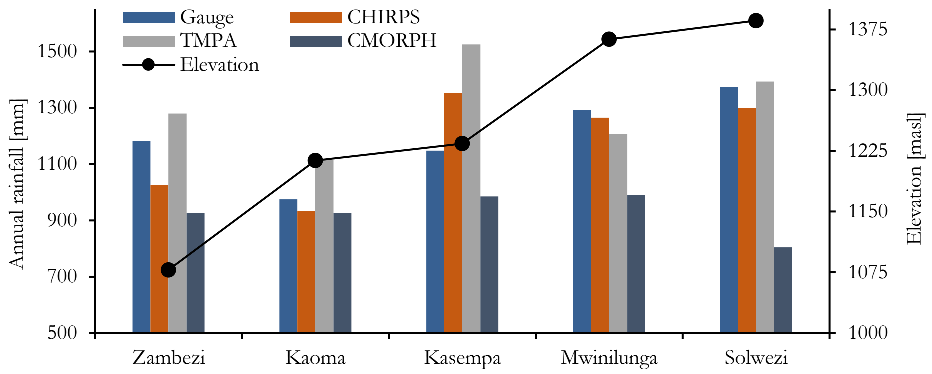

Figure 5.6: Comparison of mean annual rainfall from different SREs and gauge observations (2008-2012).

5.4.1. Rainfall occurrence analysis

Predominant daily rainfall occurrence in the basin are light showers (less than 1 mm), for instance in Figure 5.7 (a). Keeping a threshold of 0.05 mm d^{-1}, rainfall occurrence distribution at stations in and around the basin is shown in Figure 5.7 (b)-(f).

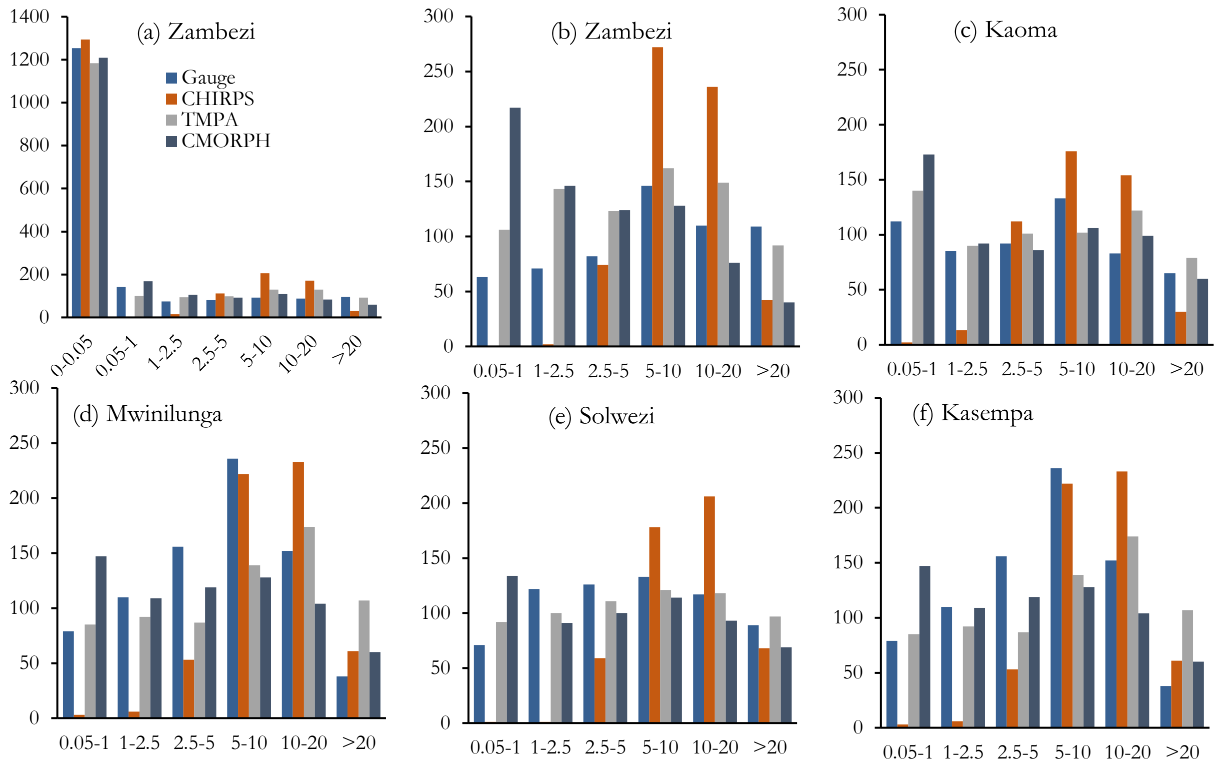

Figure 5.7: Frequency for rainfall rates (a) without and (b – f) with 0.05 mm d^{-1} threshold in the Kabompo Basin.

For low rainfall rates of 0.05 to 1 mm d^{-1}, a high variation between satellite and gauge rainfall occurrence is observed with CMORPH recording the highest differences found. CHIRPS, compared to the other rainfall products, mainly detect rainfall at 5 to 20 mm d^{-1} rate and becomes less skilful in detecting rain rates <2.5 mm d^{-1} and rainfall rates >20 mm d^{-1}. The CMORPH product on the other hand frequently detects rainfall with low rain rate but with huge differences from gauge observations. Except for rates of 10-20 mm d^{-1}, most of the TMPA rainfall occurrence are found to be evenly distributed with minimal deviations. This remarkable performance of TMPA witnessed could be related to the substantial improvements the product has received over time on its rainfall estimates over sub-Saharan Africa, as argued by Gosset et al. (2013).

Based on rainfall events detection, CMORPH has the highest number of rainfall hits, mainly found at Kasempa station agreeing with the relatively higher annual average rainfall observed in Figure 5.6. All the products experienced least number of hits at Kaoma (a low-level elevated station) and higher number of hits at Kasempa (a mid-level elevated station). At higher elevated stations (i.e. Solwezi and Mwinilunga), a higher number of missed and false rainfall counts are experienced.

Figure 5.8 shows satellite rainfall detection skills computed for SREs investigated for dry and wet seasons. Irrespective of seasonal variations, CHIRPS product was less skilful in detecting rainfall occurrence compared to other rainfall products. During dry season, for instance, its rainfall detection reduced to 20%. This weak performance is supposedly related to CHIRPS being less skilful in reporting extreme low and high rainfall rates as shown in Figure 5.7. TMPA and CMORPH show similar detection skills but the former had a better score detecting up to 88% of rainfall occurrence during wet periods.

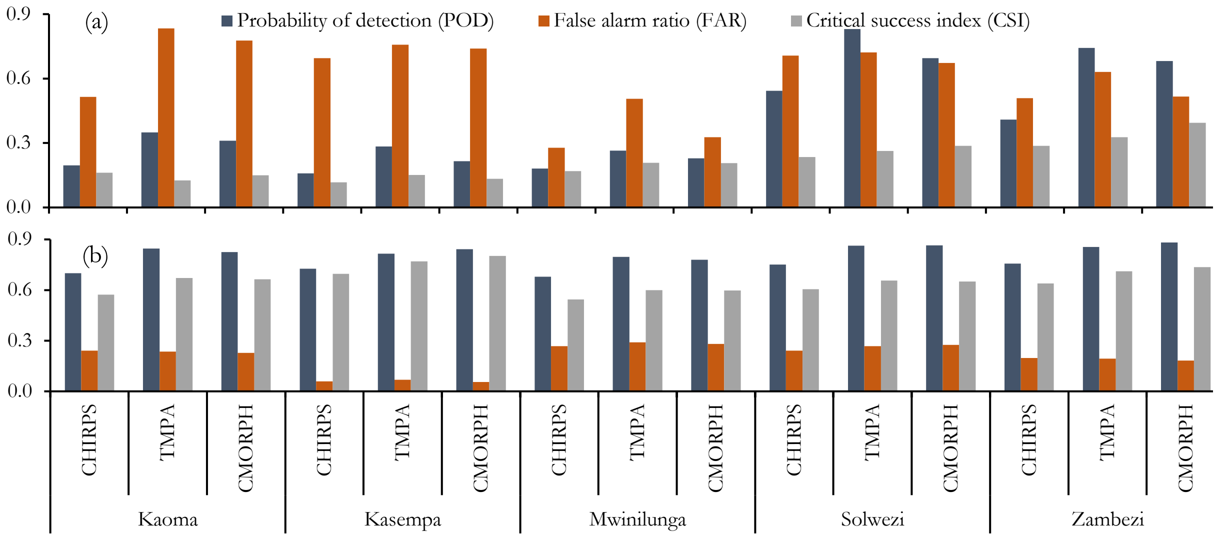

Figure 5.8: Detection skill score for investigated satellite rainfall products during (a) dry and (b) wet seasons

As evident, detection capabilities of all the three SREs are better during wet than dry seasons, a clear indication of seasonal influence on the performance of rainfall products. Rainfall occurrence correctly detected during wet and dry seasons varies between 68-88% and 16-83% respectively. Again, falsely detected rainfall occurrence during wet season outnumbers those of the dry season. TMPA reportedly has the highest falsely detected rainfall occurrence up to 0.83 during the wet seasons. CHIRPS product best performs in terms of lowest falsely detected rainfall (FAR < 0.1 for dry period) closely challenged by CMORPH falsely detecting less than 13% of rainfall occurrence for the same period.

The fraction of correctly identified rainfall in the basin is within the range 0.12-0.8. CMORPH shows the best CSI (~0.8 for wet period and an overall of 0.69) observed at Kasempa station whereas CHIRPS product has the least CSI of 0.47. Similar to the SREs' POD pattern observed, critical success indices during the dry period are lowest. In a nutshell, TMPA has the highest POD, CHIRPS product shows the least FAR while CMORPH has the best CSI in the basin.

5.4.2. Rainfall estimated depth

Here, evaluation of the satellite rainfall products across the study area over two seasons and six rain rate classes are presented. Statistical measures including bias, root mean square error and Pearson correlation coefficients (discussed in section 4.5) are used in assessing systematic differences in the satellite products compared to gauge observations in terms of rainfall depths and volume. Table 5.5 gives these indices computed for the investigated rainfall products compared to gauge observations.

Results show that a wide variation of the daily average, highest and accumulated rainfall depths between the gauge and three rainfall products exists. None of the products could match the gauge observation with CHIRPS possessing the largest daily deviation of 1.05 mm from the mean value during wet seasons.

Table 5.5: Frequency based statistics of daily estimates for the satellite rainfall products and gauged estimates in Kabompo Basin (2008-2012). Best performance when compared to gauge observations are highlighted in bold.

		Lumped					Dry season					Wet season				
		SD	CV	Mean	Max	Sum	SD	CV	Mean	Max	Sum	SD	CV	Mean	Max	Sum
Kaoma	Gauge	7.53	2.82	2.67	102.2	4873	1.45	8.64	0.17	32.4	179	10.62	1.71	6.20	102.2	4694
	CHIRPS	5.29	2.07	**2.56**	36	**4671**	**1.30**	6.30	**0.21**	15	**222**	6.81	1.16	**5.88**	36	**4450**
	TMPA	**7.81**	2.56	3.05	**118**	5568	1.61	7.63	0.21	**34**	226	**10.78**	1.53	7.06	**118**	5342
	CMORPH	6.78	**2.67**	2.54	60	4631	2.08	**8.65**	0.24	39	257	9.32	**1.61**	5.78	60	4374
Kasempa	Gauge	5.84	1.86	3.14	58	5736	0.76	5.24	0.14	9	155	7.14	0.97	7.37	58	5582
	CHIRPS	**6.60**	**1.78**	3.70	**48**	6760	2.13	**5.98**	0.36	**28**	382	**7.79**	**0.92**	**8.43**	**48**	**6379**
	TMPA	9.28	2.22	4.17	89	7623	3.28	7.11	0.46	57	492	12.07	1.28	9.42	89	7131
	CMORPH	6.96	2.58	**2.70**	132	**4927**	**1.98**	8.99	**0.22**	41	**236**	9.50	1.53	6.20	132	4692
Mwinil.	Gauge	9.13	2.58	3.54	121	6461	3.16	4.54	0.70	36	746	12.63	1.67	7.55	121	5715
	CHIRPS	6.86	1.98	**3.46**	56	**6323**	1.90	**6.37**	**0.30**	21	**319**	8.62	1.09	7.93	56	6005
	TMPA	**7.69**	2.33	3.30	63	6031	**2.23**	8.21	0.27	58	291	10.22	1.35	**7.58**	63	**5741**
	CMORPH	7.52	**2.78**	2.71	**80**	4946	1.77	10.13	0.18	**44**	187	**10.50**	**1.67**	6.29	**80**	4759
Solwezi	Gauge	9.65	2.57	3.76	124	6869	2.29	6.03	0.38	37	408	13.36	1.56	8.55	124	6461
	CHIRPS	6.00	1.68	3.56	45	6500	3.03	3.58	0.84	30	904	6.98	0.94	7.40	45	5596
	TMPA	**8.47**	2.22	**3.82**	**111**	**6965**	3.38	4.41	0.77	**41**	821	**11.20**	1.38	**8.13**	**111**	**6144**
	CMORPH	5.81	**2.64**	2.20	102	4023	**1.73**	**5.14**	**0.34**	23	**360**	8.09	**1.67**	4.84	102	3663
Zambezi	Gauge	9.43	2.92	3.23	121	5907	2.87	7.13	0.40	55	431	13.26	1.83	7.23	121	5476
	CHIRPS	5.47	1.95	2.81	44	5132	1.55	5.44	0.28	24	305	6.86	1.08	6.38	44	4827
	TMPA	**8.20**	2.34	**3.50**	72	**6396**	**2.23**	5.69	**0.39**	29	**418**	**11.06**	1.40	**7.90**	72	**5978**
	CMORPH	7.45	**2.94**	2.54	**77**	4633	2.19	**6.91**	0.32	**35**	339	10.51	**1.85**	5.67	**77**	4294

Generally, the SREs underestimated the gauge rainfall depths. For example, with exception of Kasempa station, CMORPH largely underestimated the maximum and mean rainfall depths in the basin for the entire evaluation period and during wet seasons. On one occasion, the product missed accounting for up to 44 mm rainfall occurrence at Zambezi station. A similar revelation on visualizing scatter plots of gauge estimates against respective SREs (e.g. in Appendix E), where several data points are seen spread along the x and y-axes. Moreover, all the rainfall products were found to underestimate maximum rainfall depths for every station except Kasempa, where TMPA reportedly overestimated the maximum rainfall depth. Seasonal evaluation results show that maximum rainfall depths by TMPA are closer to gauge counterparts than those of CHIRPS, that has the largest drift. At every station, CHIRPS experienced difficulties matching extreme low rainfall depths, a similar tendency exhibited when this product is compared with either TMPA or CMORPH (in Appendix F). Notwithstanding non-linear correlation amongst the three rainfall products, both TMPA and CMORPH show some similarities in reporting daily rainfall depths.

Expressing coefficient of variation (CV) as a ratio of standard deviation to mean rainfall depths at each station, TMPA exhibited the highest agreement with the gauge counterparts for the entire evaluation period but underperforms when evaluated at seasonal scales. It comparatively had the least disparities matching the respective standard deviations of the gauged estimates, with a daily deviation of 0.14-3.44 mm. Finally, the CVs from all the products were consistently lower during wet than dry seasons.

In Table 5.6, errors in the products in reference to gauge rainfall is shown. CMORPH shows the highest daily underestimation of up to 1.56 mm, while TMPA has the smallest daily bias (< 0.05 mm). In addition, CMORPH considerably underestimated seasonal rainfall depths with a daily variation of up to 3.7 mm. Results show that more bias exists during rainy season and high rainfall events than observable on no or little showers. An increase in bias with increasing rainfall depth is also evident, spanning up to daily underestimation of 29.32 mm during high rainfall events (>20 mm). When bias factor is defined for total rainfall depth detected by satellite against gauge observations, CMORPH shows least agreement with the gauge observations underestimating rainfall depth at overall bias factor of 0.79. TMPA follows with overestimations at 1.1 bias factor and CHIRPS best performing but with underestimation of 0.42 mm d^{-1} (at 0.99 bias factor).

Table 5.6: Seasonal and rain-rate based biases [mm d^{-1}] of satellite rainfall products in reference to gauge observations.

Station	Product	Lumped	Seasons		Rainfall rates [mm d^{-1}]					
			Dry	Wet	0-1.0	1.0-2.5	2.5-5.0	5-10	10-20	>20
	CHIRPS	-0.11	0.04	-0.32	0.96	3.85	2.94	-0.18	-5.78	-23.35
	TMPA	0.38	0.05	0.86	0.84	4.48	4.31	1.99	-4.06	-16.62
Kaoma	CMORPH	-0.13	0.07	-0.42	0.83	3.19	2.27	-0.51	-4.60	-20.32
	CHIRPS	0.56	0.21	1.05	0.80	5.10	4.83	1.12	-5.29	-17.84
	TMPA	1.03	0.32	2.05	0.90	5.67	5.99	2.05	-4.39	-14.06
Kasempa	CMORPH	-0.44	0.08	-1.18	0.53	4.17	3.02	-1.73	-8.28	-17.76
	CHIRPS	-0.08	-0.40	0.38	1.51	4.52	3.01	-0.12	-3.18	-28.63
	TMPA	-0.24	-0.43	0.03	1.42	3.87	1.77	0.68	-4.20	-27.81
Mwinilunga	CMORPH	-0.83	-0.52	-1.26	1.06	3.06	0.40	-0.36	-4.92	-29.32
	CHIRPS	-0.20	0.46	-1.14	1.59	5.53	4.74	0.44	-5.66	-24.68
	TMPA	0.05	0.39	-0.42	1.83	4.04	3.56	0.89	-4.67	-22.95
Solwezi	CMORPH	-1.56	-0.04	-3.70	1.06	2.01	1.19	-3.00	-8.85	-27.89
	CHIRPS	-0.42	-0.12	-0.86	1.23	4.62	2.56	0.18	-4.91	-27.25
	TMPA	0.27	-0.01	0.66	0.94	5.37	5.84	2.19	-1.68	-18.39
Zambezi	CMORPH	-0.70	-0.09	-1.56	0.67	2.26	4.02	-1.23	-4.74	-22.50

Figure 5.9 shows a Taylor diagram based on daily rainfall time series from gauge versus satellite estimates for the period 2008-2012, using all the five stations. In the diagram, correlation between the satellite and gauge based estimates is denoted by the dark radial line while on the x and y axis, standard deviations are plotted indicating the amount of variance between the time series, proportional to radial distance from the origin.

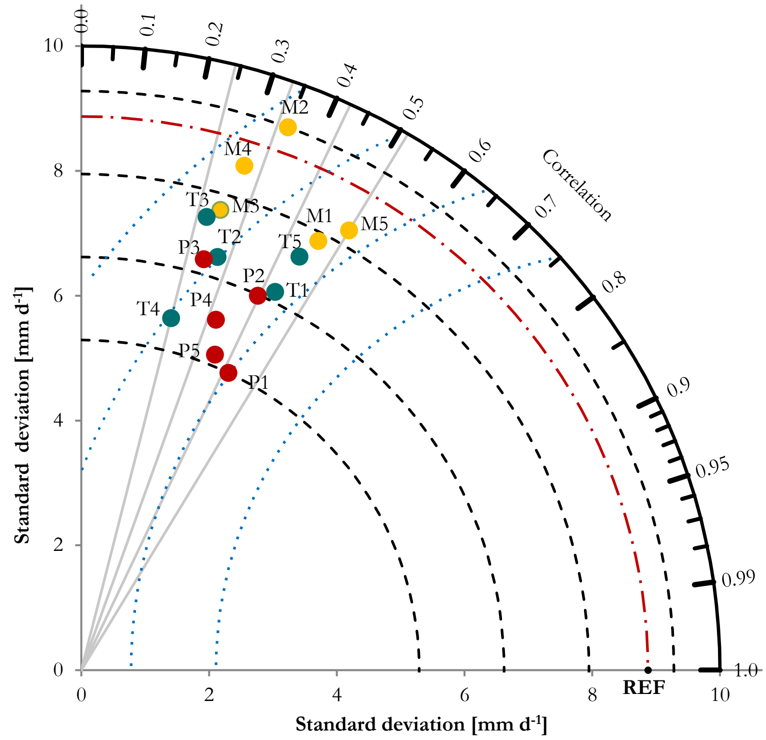

Figure 5.9: Taylor's diagram of statistical comparison between the daily time series of rain gauge (reference) vs three SREs (T-CMORPH, P-CHIRPS and M-TMPA), period 2008-2012, for Kaoma, Kasempa, Mwinilunga, Solwezi and Zambezi stations in ascending orders (1-5). Position of the symbols relative to the origin indicates how close the satellite-based estimates match gauge observations. RMS differences are directly proportional to the distance between the centered RMS and the "REF" point on x-axis (further details, see Taylor (2001)).

As can be inferred from the diagram, there is a weaker agreement (below 0.55) between gauge and SREs, with CMORPH ranging lower than 0.25 at Solwezi station. None of the products lie at the dashed arc, which signifies matchless standard deviations between the gauge and SREs. Besides, except for TMPA at Kasempa, all the other points of comparison fall below the mean standard deviation of 8.87 mm d^{-1}. All the SREs at various stations lie farther away from the reference RMS (marked "REF") indicating high daily accumulated error range of 6.76-10.75 mm d^{-1}. Individually, CHIRPS portray a closer match to indicated reference then TMPA and CMORPH.

5.4.3. Rainfall bias decomposition

Figure 5.10 shows decomposed satellite rainfall bias into hits, missed and false rain bias in terms of daily rainfall depths. As revealed, the main error source for CHIRPS is missed rainfall which likely originates from its less skilful nature in detecting extreme rainfall events as discussed in section 5.4.1. Similarly, TMPA and CMORPH products had their bias contributed mostly from falsely detected rainfall and hit bias respectively.

Error sources for SREs were found to be seasonally dependent which conforms to Ward et al., (2011) findings. Hit bias prevails during wet periods whereas dry periods largely experience falsely detected rainfall. As shown, all the bias component contributed to overestimations, with exception of hit bias element when evaluated with(out) considering seasonal variations.

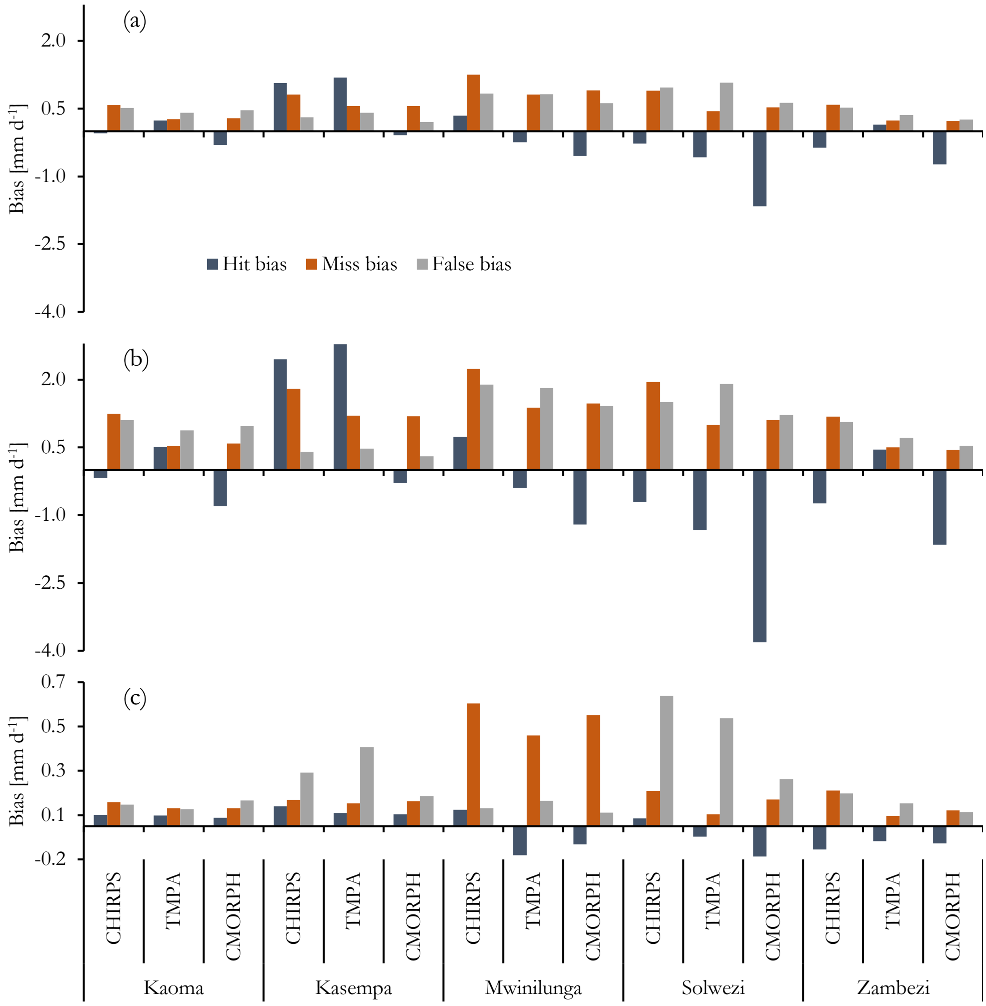

Figure 5.10: Showing (a) lumped, (b) wet and (c) dry season total bias distribution for daily satellite rainfall estimates (2008-2012) in the Kabompo Basin.

5.5. SREs bias correction analysis

5.5.1. Rainfall bias correction

The total rainfall depth (2008-2012) for the gauge, uncorrected and bias corrected satellite products with corresponding mean inter-annual ratios of rainfall amounts for SREs against gauge are shown in Table 5.7. In the basin, space variant (TFSV), time and space variant (TVSV) and distribution transformation (DT) total rainfall depths are respectively found closer to gauged estimates, suggesting their effectiveness in correcting the total rainfall depths. As shown by ratios <1, time variant (TVSF) and time-space fixed (TFSF) results in underestimated rainfall depths, particularly for CHIRPS and CMORPH estimates. There are a few instances when uncorrected SREs outperform bias corrected SREs in reproducing rainfall depths (e.g. ratios of DT: 1.14 versus uncorrected CMORPH: 0.95) indicating how ineffective bias correction schemes can be. A similar result is shown in Teng et al. (2015) for the southern Murray–Darling Basin, Australia.

Table 5.7: Total rainfall depths and mean inter-annual ratios of rainfall amounts of SREs with(out) five bias correction schemes to corresponding gauge amounts (note: 1 is best) in the Kabompo Basin. Bold figures show most improved performance of the bias schemes per station.

		Total rainfall depth [mm]					Ratio [-]				
		Kaoma	Kasempa	Mwinil.	Solwezi	Zambezi	Kaoma	Kasempa	Mwinil.	Solwezi	Zambezi
	Gauge	4,873	5,736	6,461	6,869	5,907					
CHIRPS	Uncorrected	4,671	6,760	6,323	6,500	5,132	0.97	1.18	0.98	0.95	0.88
CHIRPS	DT	**4,824**	5,204	7,016	7,116	**6,035**	**0.99**	0.91	1.09	1.04	1.03
CHIRPS	TVSV	5,045	**5,966**	6,670	7,336	5,748	1.04	1.04	1.04	1.07	0.98
CHIRPS	TVSF	4,373	6,875	5,663	**6,801**	5,082	0.90	1.20	0.88	**0.99**	0.87
CHIRPS	TFSV	**4,873**	**5,736**	**6,461**	**6,869**	**5,907**	1.01	**1.00**	1.01	**1.00**	**1.01**
CHIRPS	TFSF	4,744	6,866	**6,422**	6,601	5,212	**0.98**	1.20	**1.00**	0.96	0.89
TMPA	Uncorrected	5,568	7,623	6,031	6,965	6,396	1.04	1.33	0.94	1.01	1.09
TMPA	DT	5,492	**5,727**	7,183	7,708	6,763	1.12	**1.00**	1.12	1.12	1.15
TMPA	TVSV	**5,222**	6,084	**6,677**	7,439	**5,926**	1.08	1.06	1.04	1.08	**1.01**
TMPA	TVSF	6,484	9,585	6,968	9,641	7,836	1.33	1.67	1.08	1.40	1.33
TMPA	TFSV	**4,873**	**5,736**	**6,461**	**6,869**	**5,907**	**1.00**	**1.00**	**1.01**	**1.00**	**1.01**
TMPA	TFSF	5,655	7,742	6,126	**7,074**	6,496	1.16	1.35	0.95	1.03	1.11
CMORPH	Uncorrected	4,631	4,927	4,946	4,023	4,633	0.95	0.86	0.78	0.59	0.78
CMORPH	DT	5,539	5,946	7,360	7,821	6,974	1.14	1.04	1.14	1.14	1.19
CMORPH	TVSV	5,207	**5,913**	**6,630**	7,543	5,856	1.07	1.03	1.04	1.10	**0.99**
CMORPH	TVSF	5,278	6,179	5,797	5,439	**5,840**	1.09	1.08	0.91	0.79	**0.99**
CMORPH	TFSV	**4,873**	**5,736**	**6,461**	**6,869**	**5,907**	**1.00**	**1.00**	**1.02**	**1.00**	**0.99**
CMORPH	TFSF	**4,704**	5,004	5,024	4,086	4,705	0.97	0.88	0.79	0.60	0.79

In Figure 5.11, bias and relative bias values of the gauge, uncorrected and bias corrected satellite rainfall for the five schemes are shown. As evident and except for CMORPH estimates at 4 out of 5 stations, time variable bias values are exceedingly higher than those of uncorrected CHIRPS and TMPA rainfall estimates (e.g. TVSF: 2.11 mm d^{-1} vs uncorrected TMPA: 1.03 mm d^{-1}). Notwithstanding, a general bias decrease for uncorrected satellite rainfall depths upon correction was noted, with TVSV outperforming DT and the rest of the bias schemes (e.g. from 0.56 mm d^{-1} to 0.13 mm d^{-1} for time-space variant correcting CHIRPS at Kasempa). Space variable bias scheme removes all the cumulative rainfall differences in the products. TVSF and TFSF have the highest relative bias values (up to 0.67).

In Table 5.8, the statistical findings of the bias correction schemes in Kabompo are presented. As can be noted, the TFSV is more effective in correcting the mean values of the satellite rainfall, trailed by TVSV and DT bias factors. In terms of maximum rainfall values, the DT has a closer match to gauge observations than TVSV and other bias schemes in the basin. Large overestimation of the maximum rainfall depths is obtained from time variable bias factor correcting TMPA and CMORPH estimates (e.g. TVSF: 400.2 mm d^{-1} vs Gauge: 124.3 mm d^{-1}).

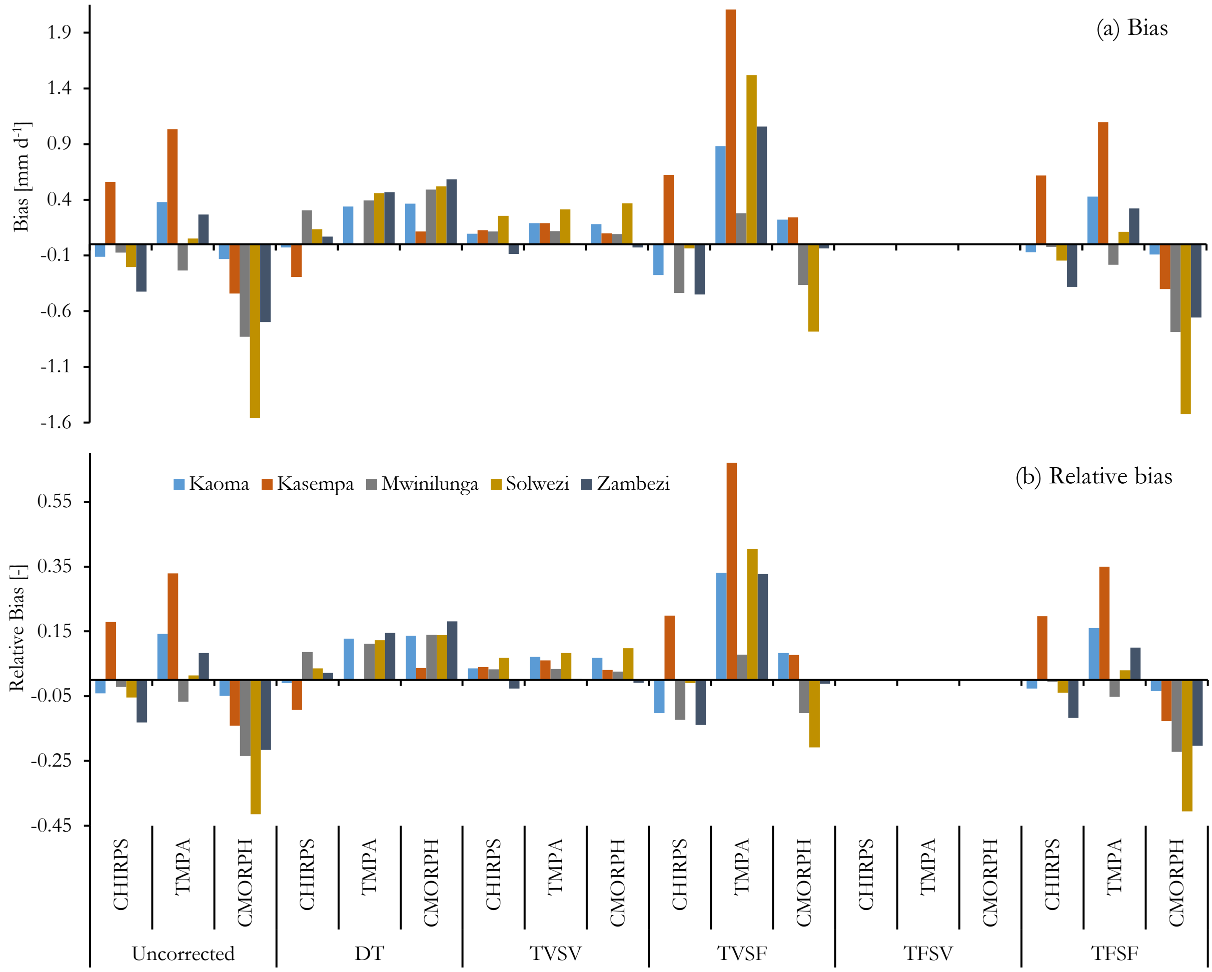

Figure 5.11: Measures of systematic differences in gauge, uncorrected and bias corrected satellite rainfall for the five correction schemes in the Kabompo Basin.

Table 5.8: Frequency evaluation coefficients for the gauge, uncorrected and bias corrected CHIRPS, CMORPH and TMPA. Bold figures show most improved performance of bias correction schemes from uncorrected SREs when compared against gauge observations.

		CHIRPS					TMPA					CMORPH				
	B-Scheme	Mean	Max	SD	CC	RMSE	Mean	Max	SD	CC	RMSE	Mean	Max	SD	CC	RMSE
Kaoma	Gauge	2.67	102.20	7.53			2.67	102.20	7.53			2.67	102.20	7.53		
	Uncorrected	2.56	35.63	5.29	0.43	7.08	3.05	117.70	7.81	0.48	7.87	2.54	60.00	6.78	0.45	7.55
	DT	2.64	**60.92**	6.43	**0.59**	6.40	3.01	79.97	7.26	0.72	**5.54**	3.03	**101.33**	7.47	**0.72**	**5.65**
	TVSV	2.76	59.48	6.22	0.51	6.89	2.86	74.57	7.35	**0.60**	6.69	2.85	57.10	7.58	0.55	7.18
	TVSF	2.39	49.79	5.70	0.56	**6.39**	3.55	187.55	12.29	0.47	11.02	2.89	136.57	10.06	0.48	9.27
	TFSV	**2.67**	37.17	5.52	0.43	7.14	**2.67**	**103.00**	**6.84**	0.48	7.38	**2.67**	63.13	7.13	0.45	7.71
	TFSF	2.60	36.19	**5.37**	0.43	7.10	3.10	119.53	7.93	0.48	7.94	2.57	60.94	**6.88**	0.45	7.60
Kasempa	Gauge	3.14	58.30	5.84			3.14	58.30	5.84			3.14	58.30	5.84		
	Uncorrected	3.70	47.75	6.60	0.42	6.76	4.17	88.78	9.28	0.35	9.13	2.70	131.65	6.96	0.31	7.60
	DT	2.85	43.78	**5.12**	**0.55**	**5.24**	3.13	**56.70**	**5.65**	**0.58**	**5.29**	3.25	59.06	6.03	**0.56**	**5.56**
	TVSV	3.27	47.13	6.12	0.47	6.14	3.33	66.11	7.20	0.42	7.10	3.24	**58.49**	7.24	0.45	6.99
	TVSF	3.76	79.20	8.40	0.45	7.78	5.25	263.05	16.23	0.32	15.51	3.38	232.16	11.60	0.30	11.32
	TFSV	**3.14**	40.52	5.60	0.42	6.17	**3.14**	66.80	6.98	0.35	7.37	**3.14**	153.26	8.10	0.31	8.41
	TFSF	3.76	**48.50**	6.71	0.42	6.83	4.24	90.16	9.42	0.35	9.26	2.74	133.71	**7.06**	0.31	7.67
Mwinilunga	Gauge	3.54	120.60	9.13			3.54	120.60	9.13			3.54	120.60	9.13		
	Uncorrected	3.46	56.32	6.86	0.28	9.76	3.30	63.48	7.69	0.28	10.13	2.71	79.75	7.52	0.26	10.23
	DT	3.84	**100.03**	8.61	0.46	9.21	3.93	**94.99**	8.82	**0.49**	**9.05**	4.03	**107.68**	8.91	**0.51**	**8.94**
	TVSV	3.65	80.39	7.98	0.36	9.73	3.65	91.74	8.68	0.36	10.06	3.63	86.99	9.00	0.39	9.97
	TVSF	3.10	60.92	7.04	**0.47**	**8.50**	3.81	324.61	13.08	0.40	12.60	3.17	203.37	11.72	0.37	11.87
	TFSV	**3.54**	57.55	7.01	0.28	9.83	**3.54**	68.01	8.24	0.28	10.42	**3.54**	104.17	9.83	0.26	11.53
	TFSF	3.52	57.20	**6.96**	0.28	9.81	3.35	64.48	**7.81**	0.28	10.19	2.75	81.00	**7.64**	0.26	10.29
Solwezi	Gauge	3.76	124.30	9.65			3.76	124.30	9.65			3.76	124.30	9.65		
	Uncorrected	3.56	45.17	6.00	0.35	9.41	3.81	111.34	8.47	0.30	10.75	2.20	101.95	5.81	0.24	10.11
	DT	3.90	**113.22**	8.56	**0.51**	**9.05**	4.22	102.61	9.15	**0.47**	**9.66**	4.28	**120.16**	9.86	**0.43**	10.42
	TVSV	4.02	71.67	7.71	0.45	9.26	4.07	72.05	8.67	0.43	9.81	4.13	102.96	9.92	0.39	10.83
	TVSF	3.72	57.51	7.61	0.43	9.36	5.28	400.20	18.09	0.26	18.22	2.98	179.70	10.56	0.25	12.39
	TFSV	**3.76**	47.73	6.34	0.35	9.50	**3.76**	109.80	8.36	0.30	10.69	**3.76**	174.07	9.92	0.24	12.05
	TFSF	3.61	45.88	**6.09**	0.35	9.43	3.87	**113.08**	**8.61**	0.30	10.82	2.24	103.54	**5.90**	0.24	**10.14**

Zambezi	Gauge	3.23	120.60	9.43			3.23	120.60	9.43			3.23	120.60	9.43		
	Uncorrected	2.81	43.82	5.47	0.38	8.92	3.50	71.58	8.20	0.51	8.78	2.54	76.60	7.45	0.46	8.98
	DT	3.30	**82.84**	8.09	0.52	8.64	3.70	**84.43**	8.92	**0.68**	**7.40**	3.82	85.01	9.37	**0.65**	**7.87**
	TVSV	3.15	73.88	6.79	0.49	8.49	3.24	83.74	7.94	0.60	7.83	3.21	97.35	8.71	0.60	8.13
	TVSF	2.78	53.95	6.45	**0.54**	**8.07**	4.29	158.45	12.46	0.61	10.12	3.20	214.56	11.65	0.53	10.42
	TFSV	**3.23**	50.43	6.29	0.38	9.12	**3.23**	66.10	**7.57**	0.51	8.56	**3.23**	**97.66**	9.50	0.46	9.85
	TFSF	2.85	44.50	**5.55**	0.38	8.94	3.56	72.70	8.33	0.51	8.83	2.58	77.80	**7.57**	0.46	9.01

The standard deviation of most of the bias correction schemes fall in the range 5.5 to 9 mm d^{-1}. TFSF and DT perform better than the other schemes in giving standard deviations closer to gauge observations. However, deterioration of standard deviations post-bias correction is noted (e.g. DT: 9.86 vs uncorrected: 5.81), which shows probable introduction of additional errors by these schemes. This observation is consistent with findings by Teng et al. (2015) confirming that bias correction can potentially introduce additional errors. Based on correlation coefficients, DT bias corrected rainfall shows a better agreement (up to 0.72 correlation) with gauge observations, followed by TVSF and TVSV schemes. Compared to uncorrected SREs, all the schemes yielded improved RMSEs for every station, except Solwezi, with DT consistently lower.

Table 5.9 gives the percentage of days belonging to six rain rate classes for the gauge, uncorrected and bias corrected satellite rainfall. As evident, light showers (less than 1 mm d^{-1}) are the most predominant accounting for more than 70% of rainfall occurrence. Heavy rainfall accounts for only 4.2% of the rainfall falling in the basin. Based on forgoing and in order of most effective bias correction methods, DT, TVSF and TVSV are found to be more appropriate in reproducing patterns of rain rates against gauged rainfall for Kabompo.

Table 5.9: Percentage of days belonging to six rain rate classes (0-1, 1-2.5, 2.5-5, 5-10, 10-20 and >20 mm d^{-1}) for Kabompo Basin. Bold figures indicate best bias correction scheme performance when compared against gauge and uncorrected satellite rainfall.

	Product	CHIRPS						TMPA						CMORPH					
	Rain intensity	0-1.0	1.0-2.5	2.5-5.0	5-10	10-20	>20	0-1.0	1.0-2.5	2.5-5.0	5-10	10-20	>20	0-1.0	1.0-2.5	2.5-5.0	5-10	10-20	>20
Kaoma	Gauge	74.27	5.15	5.09	7.39	4.54	3.56	74.27	5.15	5.09	7.39	4.54	3.56	74.27	5.15	5.09	7.39	4.54	3.56
	Uncorrected	73.45	0.71	6.13	9.63	8.43	1.64	72.95	4.93	5.53	5.59	6.68	4.33	75.52	5.15	4.82	5.81	5.42	3.29
	DT	70.17	**6.02**	8.16	**7.01**	5.75	**2.90**	67.82	6.79	7.77	**7.83**	6.35	**3.45**	67.93	6.51	8.21	**7.77**	5.97	**3.61**
	TVSV	73.51	1.59	**5.15**	9.25	7.72	2.79	73.67	4.82	5.86	5.75	6.19	3.72	**75.10**	4.38	**5.36**	5.69	5.31	4.16
	TVSF	**74.88**	2.57	5.97	8.32	**5.53**	2.74	**74.17**	5.47	**5.20**	5.47	**4.93**	4.76	76.85	5.36	4.16	5.25	**4.43**	3.94
	TFSV	73.45	0.60	6.13	9.30	8.81	1.70	73.34	5.69	5.25	5.80	6.68	3.23	75.53	4.93	4.49	5.80	5.36	3.89
	TFSF	73.45	0.66	6.19	9.47	8.54	1.70	72.91	**4.87**	5.58	5.53	6.51	4.60	75.53	**5.15**	4.65	5.64	5.58	3.45
Kasempa	Gauge	61.74	6.29	8.65	12.92	8.32	2.08	61.74	6.29	8.65	12.92	8.32	2.08	61.74	6.29	8.65	12.92	8.32	2.08
	Uncorrected	68.53	0.33	2.90	12.15	12.75	3.34	67.20	5.04	4.76	7.61	9.53	5.86	71.25	6.02	6.68	6.96	5.75	3.34
	DT	**63.22**	**5.80**	**7.66**	14.40	7.39	1.53	**61.08**	**6.13**	**9.58**	**12.86**	**8.48**	**1.86**	**61.36**	**6.46**	**7.94**	**13.19**	**8.70**	**2.35**
	TVSV	68.53	1.15	5.36	**12.21**	9.96	2.79	67.76	4.60	6.90	8.87	7.66	4.21	70.01	4.43	6.40	7.44	7.17	4.54
	TVSF	69.73	2.74	4.32	9.14	**9.03**	5.04	68.20	5.58	5.25	6.79	6.57	7.61	72.41	7.12	5.20	6.08	4.82	4.38
	TFSV	68.53	0.44	5.15	13.63	10.45	**1.81**	68.91	4.82	5.75	9.14	7.99	3.39	70.55	5.47	6.46	6.84	6.62	4.05
	TFSF	68.53	0.33	2.63	12.04	12.97	3.50	67.21	4.87	4.76	7.55	9.58	6.02	71.26	6.02	6.62	6.84	5.75	3.50
Mwinilunga	Gauge	67.76	6.57	7.06	7.22	6.51	4.87	67.76	6.57	7.06	7.22	6.51	4.87	67.76	6.57	7.06	7.22	6.51	4.87
	Uncorrected	71.98	0.05	3.23	9.74	11.11	3.89	70.04	5.48	6.08	6.63	6.46	5.31	74.10	5.20	5.53	6.24	5.15	3.78
	DT	**65.30**	**4.16**	**7.61**	10.45	7.55	**4.93**	63.00	**6.40**	**7.88**	10.29	7.12	5.31	63.11	**6.35**	**7.28**	10.02	7.88	5.36
	TVSV	72.14	1.15	4.00	**8.21**	9.03	5.47	**69.68**	5.25	5.47	6.62	7.33	5.64	**72.36**	3.72	4.71	6.90	**6.62**	5.69
	TVSF	73.07	1.97	4.93	8.59	**7.22**	4.21	72.09	5.20	5.42	**7.06**	4.98	**5.25**	75.48	5.20	4.82	**7.12**	3.45	3.94
	TFSV	71.98	0.05	3.17	9.69	10.89	4.21	69.84	5.47	5.80	6.13	7.06	5.69	72.91	4.93	4.38	6.90	5.64	**5.25**
	TFSF	71.98	0.05	3.17	9.74	10.89	4.16	70.06	5.47	6.02	6.40	**6.68**	5.36	74.11	5.20	5.36	6.35	5.20	3.78
Solwezi	Gauge	70.81	4.38	4.65	8.00	6.19	5.97	70.81	4.38	4.65	8.00	6.19	5.97	70.81	4.38	4.65	8.00	6.19	5.97
	Uncorrected	65.74	0.11	4.05	14.89	12.92	2.30	63.36	7.83	6.74	8.87	8.16	5.04	71.41	8.16	6.85	7.23	4.16	2.19
	DT	64.20	**4.65**	8.43	10.18	**7.22**	**5.31**	62.34	6.73	7.28	9.30	8.59	5.75	63.93	**6.13**	8.26	**7.99**	7.22	**6.46**
	TVSV	65.79	1.15	5.69	11.99	10.95	4.43	63.22	7.39	7.50	**8.16**	7.77	**5.97**	67.49	6.84	**5.75**	6.40	6.95	6.57
	TVSF	**67.93**	2.68	5.80	**9.52**	9.09	4.98	**66.83**	**6.62**	**6.51**	7.28	**5.97**	6.79	73.67	6.90	6.46	5.20	4.00	3.78
	TFSV	65.74	0.11	3.34	14.45	13.57	2.79	63.55	7.83	6.68	8.87	8.16	4.93	67.05	7.50	6.57	7.72	**5.80**	5.36
	TFSF	65.74	0.11	**4.00**	14.56	13.19	2.41	63.38	7.77	6.68	8.70	8.26	5.20	**71.43**	8.16	6.84	7.12	4.16	2.30
Zambezi	Gauge	75.81	4.32	4.60	5.09	4.87	5.31	75.81	4.32	4.60	5.09	4.87	5.31	75.81	4.32	4.60	5.09	4.87	5.31
	Uncorrected	70.83	0.82	6.13	11.22	9.36	1.64	70.21	5.15	5.37	7.12	7.06	5.09	75.25	5.86	5.09	5.97	4.60	3.23
	DT	69.18	**5.36**	7.01	**7.94**	**5.97**	**4.54**	66.83	6.19	7.44	8.48	6.08	4.98	67.05	6.73	6.79	7.99	6.19	**5.25**
	TVSV	70.88	1.75	6.08	9.41	8.54	3.34	70.66	5.15	6.35	6.90	6.29	4.65	73.02	**5.09**	5.80	6.29	4.76	5.04
	TVSF	**73.02**	2.30	6.40	8.54	6.02	3.72	**72.36**	**4.98**	**5.09**	**5.80**	**5.20**	6.57	76.52	6.73	4.21	**4.32**	4.05	4.16
	TFSV	70.83	0.60	**4.82**	9.30	11.28	3.17	70.61	5.20	5.97	7.06	6.62	4.54	74.00	5.64	**4.82**	6.13	**4.76**	4.65
	TFSF	70.83	0.71	5.97	11.06	9.63	1.81	70.17	5.09	5.42	6.90	7.12	**5.31**	**75.26**	5.86	5.04	5.91	4.65	3.28

5.5.2. Seasonality influence on SREs bias correction

DT is found more effective correcting for mean values and reducing differences between gauge and satellite rainfall than other schemes during the dry and wet seasons (Table 5.10). This bias correction also results in improved total rainfall depths but underestimation of total gauged rainfall during dry season is shown. Generally, all the bias schemes investigated have higher accumulated errors during wet seasons than dry seasons although for both seasons improvement over uncorrected rainfall is shown. Similarly, larger standard deviations are exhibited by these schemes for wet seasons with unsatisfactory performance from TVSF, TFSF and TFSF bias factors.

Table 5.10: Frequency based statistics for gauge, uncorrected and bias corrected satellite rainfall for dry and wet seasons.

		Dry season						Wet season					
	Bias scheme	Mean	Max	Sum	SD	RMSE	Ratio	Mean	Max	Sum	SD	RMSE	Ratio
	Gauge	0.36	105.2	5969	8.32			7.38	105.2	5586	11.40		
CHIRPS	Uncorrected	0.40	23.6	426	1.98	2.70	0.069	7.20	45.7	5451	7.41	12.62	0.978
	DT	**0.37**	**34.3**	394	2.12	**2.18**	0.064	**7.46**	**80.2**	5645	**9.69**	**11.67**	1.009
	TVSV	0.42	33.5	**452**	**2.30**	2.75	**0.073**	7.53	66.5	5702	8.91	12.14	1.021
	TVSF	0.27	27.7	285	1.68	2.45	0.045	7.23	60.3	5474	9.29	12.10	0.979
	TFSV	0.41	24.0	437	2.02	2.69	0.071	7.31	46.7	5532	7.56	12.57	0.992
	TFSF	0.40	23.9	433	2.01	2.72	0.070	7.31	46.5	**5536**	7.53	12.67	**0.993**
TMPA	Uncorrected	0.42	43.7	450	2.55	2.94	0.073	8.01	90.6	6067	11.07	14.07	1.093
	DT	0.43	34.0	464	2.27	**1.80**	0.075	8.07	83.7	6110	10.50	**11.27**	1.095
	TVSV	0.45	46.3	**485**	**2.68**	2.85	**0.079**	7.64	77.6	5785	10.57	12.42	1.037
	TVSF	**0.37**	**54.9**	400	2.71	2.99	0.065	10.18	266.8	7703	20.87	20.66	1.379
	TFSV	0.39	40.3	415	2.33	2.76	0.067	**7.34**	82.7	**5554**	10.14	13.40	**0.996**
	TFSF	0.43	44.4	457	2.58	2.97	0.075	8.14	**92.0**	6162	**11.24**	14.18	1.110
CMORPH	Uncorrected	0.26	36.4	276	1.95	2.57	0.047	5.75	90.0	4356	9.58	13.47	0.791
	DT	0.46	33.5	**489**	**2.38**	**2.12**	**0.079**	8.24	94.7	6239	11.06	**11.66**	1.118
	TVSV	**0.34**	38.7	362	2.28	2.53	0.059	7.75	79.2	5867	**11.55**	13.02	1.049
	TVSF	0.23	38.5	248	1.98	2.44	0.041	7.21	193.3	5458	16.24	16.91	0.987
	TFSV	**0.34**	**46.0**	367	2.51	2.90	0.061	**7.40**	**118.5**	**5602**	12.36	15.01	**1.003**
	TFSF	0.26	37.0	280	1.98	2.59	0.047	5.84	91.4	4424	9.73	13.54	0.804

As observed, the effectiveness of each of these bias factors widely varies in the basin depending on evaluation indicator being considered. Overall, the three most effective bias correction schemes are DT (exhibiting highest CC > 0.7, least standard deviation of 0.52 mm d^{-1} and daily accumulated error range 5.24-10.42 mm), TFSV for correcting mean rainfall and TVSV exhibiting the lowest daily bias < 0.09 mm respectively. This is consistent with Gumindoga et al. (2016) findings showing DT and spatial-temporal to be effective in correcting mean values of SREs for Zambezi Basin.

5.6. Impact on TOPMODEL rainfall-runoff application

5.6.1. Model calibration, sensitivity analysis and validation

Table 2.1 shows parameter values used in initializing the TOPMODEL for the period between Sept. 2009 and Aug. 2010. Initialization results suggested the model could well simulate baseflows, rising and recession curves of the hydrograph but posed difficulties in matching the peak discharges. Three dimensional plots in Figure 5.12 and Figure 5.13 represent sensitivity of the model to changes in m, T_0 and SR_{max} parameters that aided further fine-tuning the model performance for the period Sept. 2009 – Oct. 2012.

Table 5.11: Parameter values used in initializing the model.

Parameter	m [m]	T_0 [m²/h]	Td [h]	CHV [m/h]	RV [m/h]	SR_{max} [m]	Q_0 [m/dt]	SR0 [m]
Value	0.035	4.2	28	1200	402	0.009	0.000109053	0.002

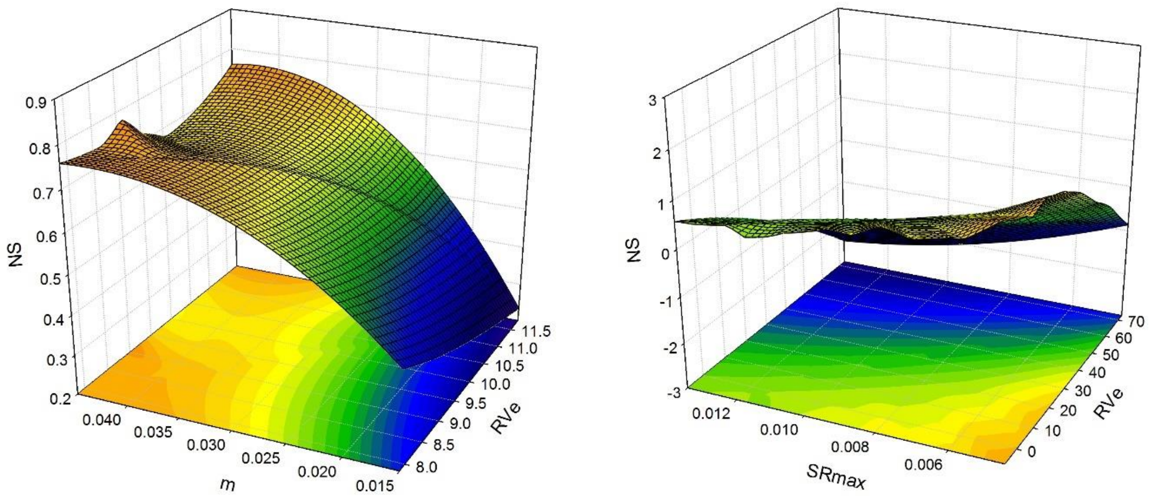

Figure 5.12: Showing effects of m and SR_{max} parameters on model efficiency.

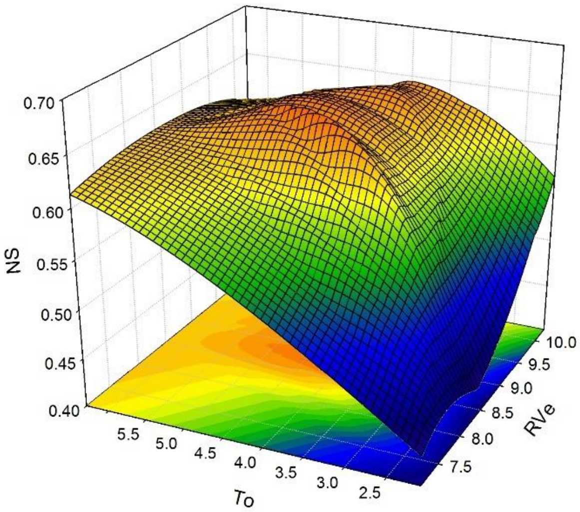

Figure 5.13: Effects of T_0 parameter on model efficiency.

While keeping the initial parameter values in Table 5.11 fixed, soil hydraulic conductivity decay (m) parameter was changed within the range 0.015-0.045. These changes directly influenced the Nash Sutcliffe (NS) efficiency and relative volume error (RV_E). For example, increasing m from 0.015 to 0.045 resulted in improved model efficiency to 0.76 and reduced over-simulated water volume error by 3.86%. Smaller values of m cause high peaks and virtually no to little base flows. This implies that, at low m values, less effective soil depths is available for water infiltration, thus reduced sub-surface flows resulting in increased surface routing of water to the outlet as also noted by Gumindoga et al. (2011).

Varying maximum root zone available water capacity (SR_{max}) values within range 0.0045-0.0135 significantly affects RV_E. It results in RV_E changing from 72.9% for low values to -6.74% for higher values of SR_{max}. The model efficiency is, however, not very sensitive to this parameter. But NS efficiencies become low (i.e. 0.02 and 0.57) at 0.0054 and 0.0135 values of SR_{max} respectively. Similarly, effective soil transmissivity at saturation (T_0) varied between 2.1 and 6.3 both decreases and increases model efficiency.

At low T_0 values, a more satisfactory RV_E < 7.12% are obtained but show poor model performance (NS <43%). The above are the three most critical TOPMODEL parameters found for accurate streamflow simulations.

Fine-tuning the model by incorporating the above sensitivity results yields hydrograph in Figure 5.14 and optimal model parameter values summarized in Table 5.12. Compared to observed streamflow, the model successfully reproduced the baseflows for all the years. Similarly, both the rising and recession limbs of the model hydrograph were well predicted on combining higher $(T_0 > 4)$ and lower $(m \leq 0.03)$ values. However, the model could not fully predict high peaks; for instance, at the onset year, the amount of runoff simulated substantially exceed reality. This indicates either a shallow nature of the catchment thus low infiltration capacity or possible errors in spatial distribution of rainfall and discharge, a subject for further investigations. Alternatively, this could be related to errors in coupling optimal m and T_0 values governing effective soil depth and thus transmissivity decay. Furthermore, by setting the T_0 value in the model, a homogeneous soil is assumed for the catchment; which likely varies for such a large basin. Attempts of further improving the peak flows only yielded compromised baseflows while deteriorating other parts of the simulated hydrograph. The model also achieved good timing of the peaks exhibiting reasonable performance at NS efficiency of 0.65 and RV_E of 10.03%.

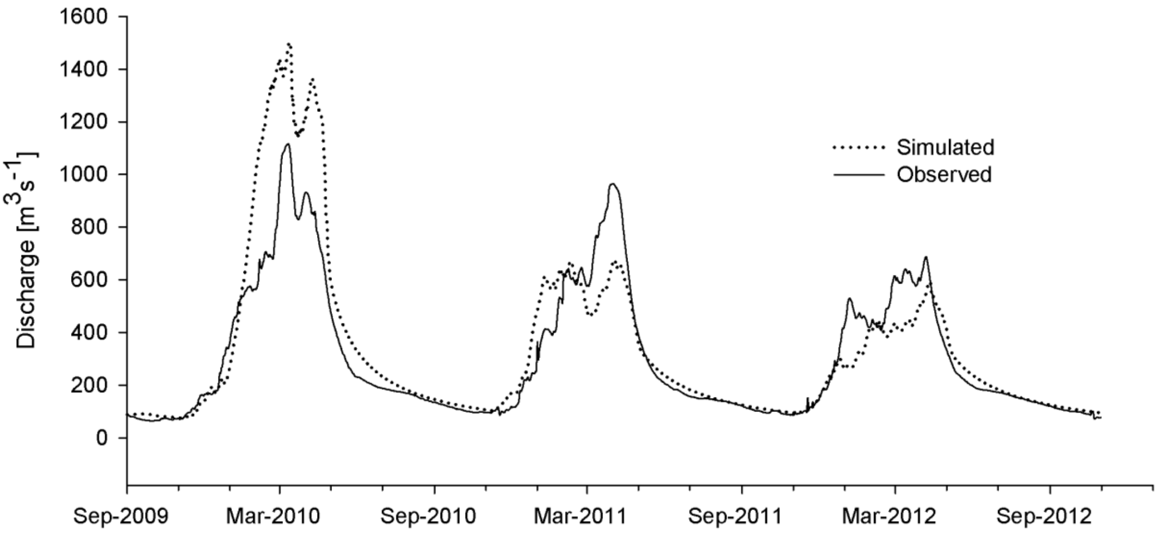

Figure 5.14: Calibration results for the Kabompo Basin (Sept. 2009 – Aug. 2012).

Table 5.12: Optimal parameter values and model efficiency on calibration.

m [m]	T_0 [m²/h]	SR_{max} [m]	NS [-]	RV_E [%]
0.03	4.2	0.009	0.65	10.03

The optimal calibration parameter values when applied to different hydro-meteorological dataset (Sept. 2007-Nov. 2008) yields validation hydrograph shown in Figure 5.15. Generally, the model was able to simulate the patterns of recession curves and base flows of the hydrograph with a RV_E of 21.2% lower compared to 10.03% obtained during calibration. Similarly, the high peaks were moderately matched and timed with NS efficiency reducing to 0.57 from 0.65. However, the model could not match the rising limb of the observed hydrograph, particularly the onset of rainy period.

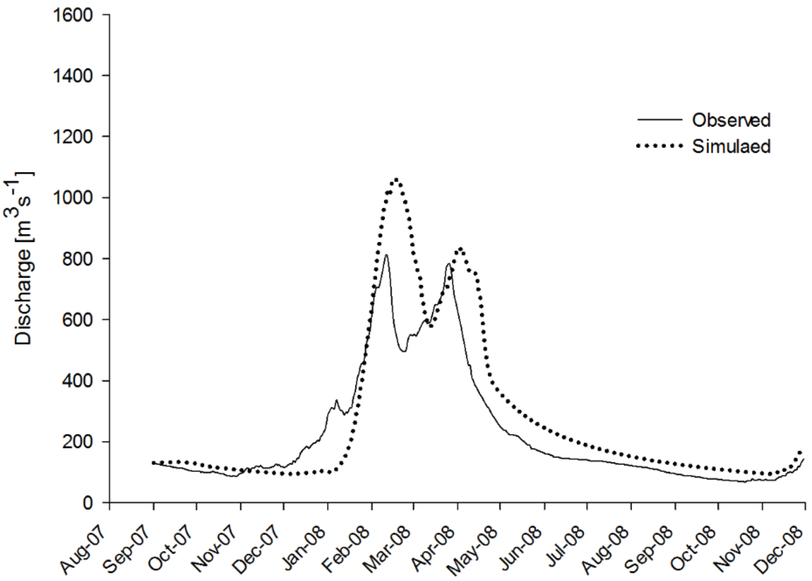

Figure 5.15: Validation results for the Kabompo Basin, Sept. 2007 - Nov. 2008.

5.6.2. Model water balance closure based on remote sensing rainfall

Comparison of simulated hydrographs based on uncorrected versus space-time variant bias corrected satellite rainfall instead of *in-situ* rainfall are shown in Figure 5.16 - Figure 5.18. The uncorrected rainfall products poorly simulated baseflows and could not properly model recession curves. A clear indication of bias in SREs propagating into streamflow simulations. For the uncorrected products, TMPA shows the highest model efficiency of 0.78 whereas CMORPH has the largest volume error (-16.42 %) for the simulation period of 2008-2012.

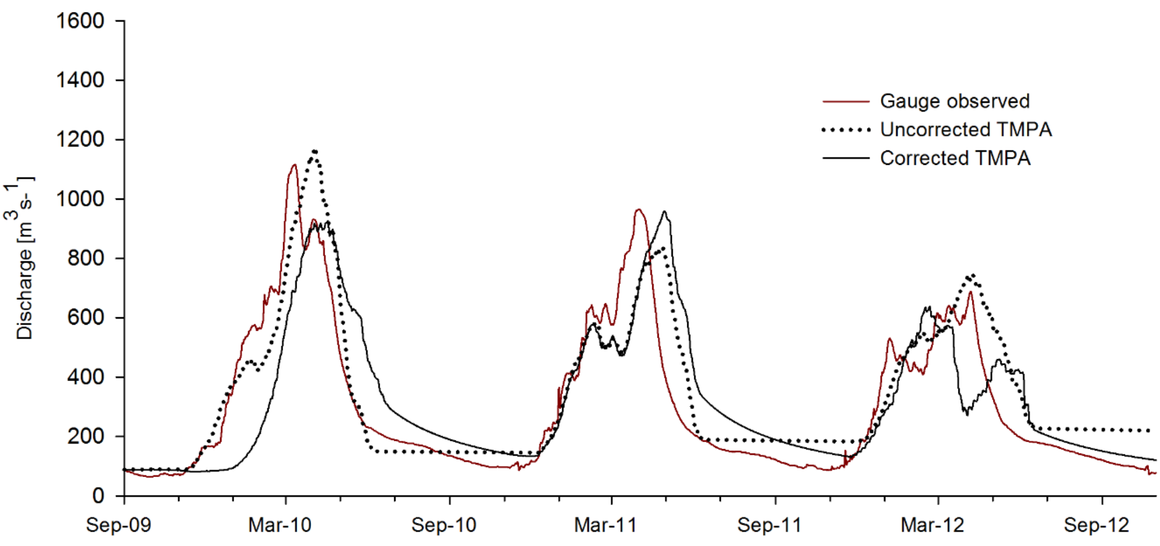

Figure 5.16: Comparing streamflow simulations based on uncorrected and bias corrected TMPA rainfall estimates (Sept. 2009-Aug 2012).

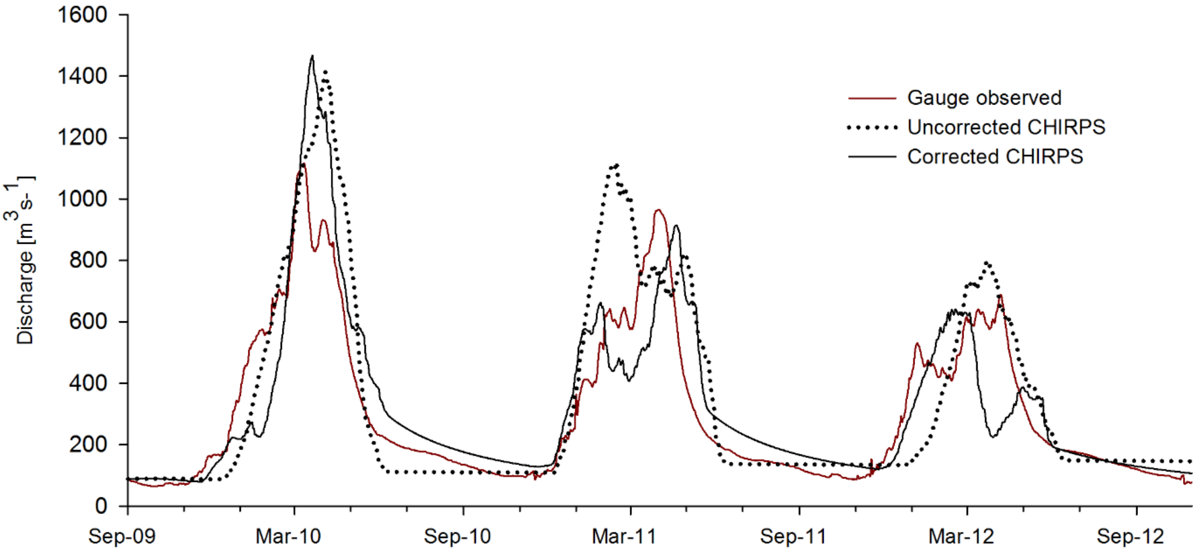

Figure 5.17: Streamflow simulations based on uncorrected and bias corrected CHIRPS rainfall estimates (Sept. 2009-Aug 2012).

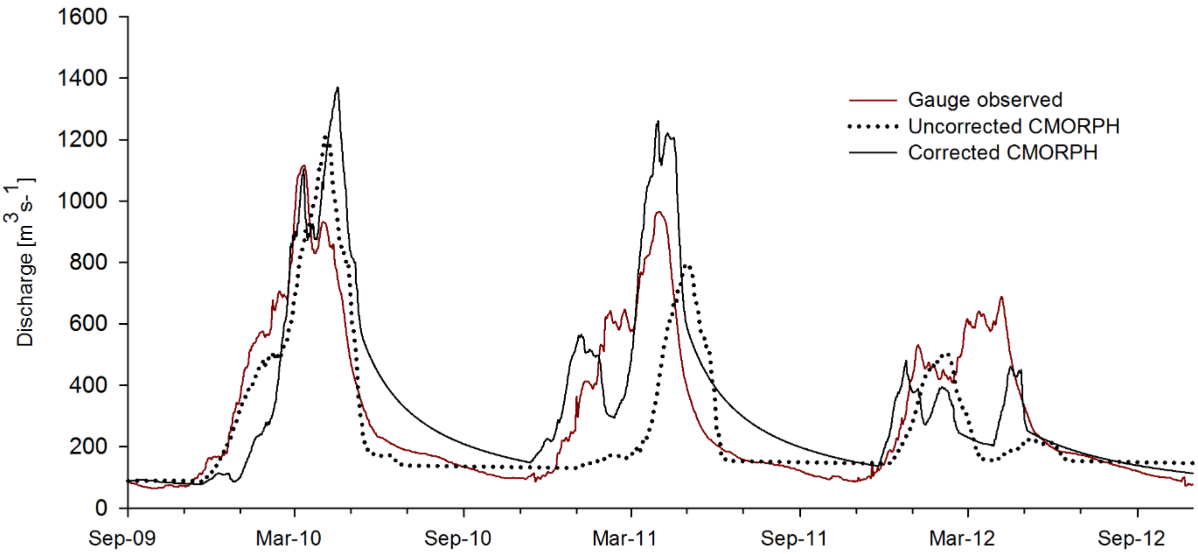

Figure 5.18: Streamflow simulations based on uncorrected and bias corrected CMORPH rainfall estimates (Sept. 2009-Aug 2012).

TOPMODEL calibration output based on bias corrected rainfall, except for CMORPH, results in more visually improved peak flows than both uncorrected satellite and *in-situ* rainfall. In addition to better captured hydrograph patterns, an improved volumetric error between 4.8% and 9.9% are achieved than when uncorrected rainfall (-16.42%) or *in-situ* rainfall (10.03%) is used. This is consistent with Habib et al. (2014) findings when they forced HBV-96 with bias corrected CMORPH rainfall in the Gilgel Abbay catchment. Resulting model efficiency in terms of NS both improved and deteriorated on using bias corrected rainfall. NS for CHIRPS improved to 0.67 whereas that of CMORPH reduced to 0.52 compared to *in-situ* rainfall, but an improvement over uncorrected counterpart. For TMPA, corrected rainfall estimates show lower NS of 0.53 than uncorrected and *in-situ* rainfall.

Except for the delayed effect, the model simulates well the high peaks, recession curves, falling limbs and base flows of the hydrographs. The delayed effect, could be due to model infiltrating most of rainwaters into the soil. TMPA results in lower simulated streamflow than CHIRPS and CMORPH. Figure 5.19 illustrates an inter-comparison of streamflow results from the three bias corrected rainfall.

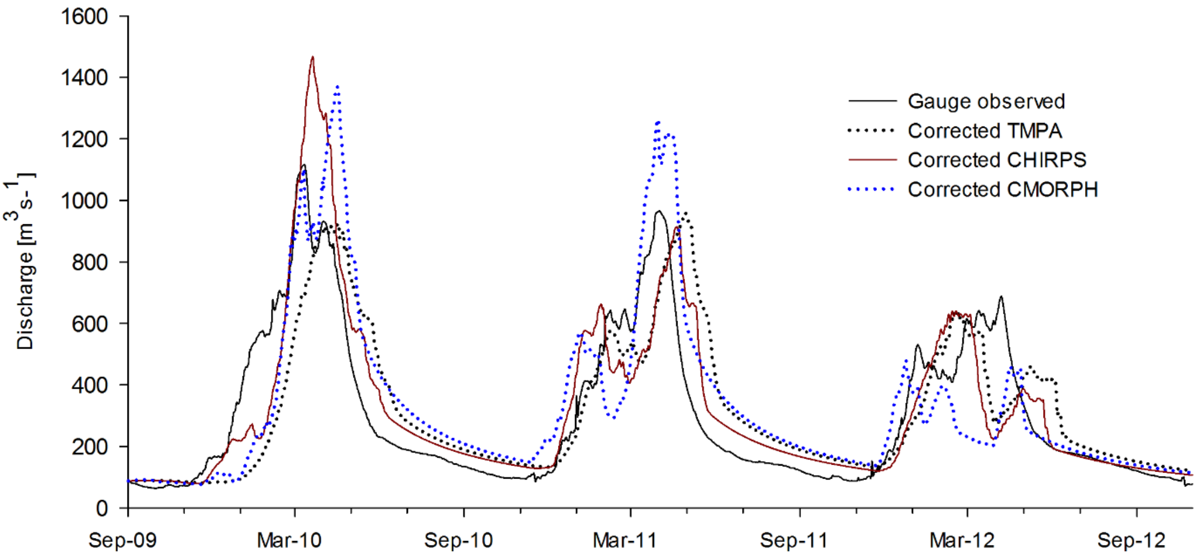

Figure 5.19: Streamflow simulation based on bias corrected (TVSV) TMPA and CHIRPS rainfall (Sept. 2009 – Aug. 2012).

Table 5.13 shows a comparison of water balance components obtained from the model based on *in-situ*, uncorrected and bias corrected satellite rainfall forcing. These are based on simulation results for the period 2009-2012, where the end of the dry season in 2009 marked the onset of the simulation period. All the three rainfall products (uncorrected and bias corrected) over-simulated accumulated rainfall, evaporation and root zone storage versus *in-situ* model forcing. Uncorrected SREs show higher over-estimates than bias corrected estimates. Water balance closure errors presented represent the water balance equation residual term, and are expressed as percentage of precipitation, as the main model forcing. A clear improvement in water balance closure is shown on bias correcting the satellite rainfall estimates. However, correcting CMORPH resulted in deteriorating closure (4.2%) compared to that of *in-situ* rainfall (1.9%) in the basin.

Table 5.13: Kabompo Basin water balance components and closure error for TOPMODEL simulation (2008-2012).

		Un-corrected			Corrected		
Water balance components [mm]	In- situ	TMPA	CHIRPS	CMORPH	TMPA	CHIRPS	CMORPH
Precipitation	2414	4006	3639	3026	2655	2649	2635
Actual ET	1950	2424	2566	2440	2207	2199	2207
Simulated Discharge	479.2	493.7	489.9	366.9	457.7	463.8	437.0
Root zone storage deficit	9.0	69.3	100.0	97.8	16.8	20.2	23.4
Upper zone storage	0.0	0.0	0.0	0.0	0.0	0.0	0.0
Catchment deficit to saturation	52.4	1963.0	678.7	275.5	38.9	41.7	97.0
Water balance Closure Error	46.2	3120.6	1361.8	592.4	46.0	48.1	111.4
WB Closure Error, [%]	1.9	77.9	37.4	19.6	1.7	1.8	4.2
NS [-]	0.64	0.78	0.60	0.45	0.53	0.67	0.52
RV_E [%]	10.03	11.82	11.82	-16.42	4.80	5.81	9.99

6. CONCLUSION AND RECOMMENDATION

6.1. Conclusion

A clear relationship between elevation and accumulated satellite rainfall measured in the basin could not be indicated in this study. Perhaps due to insignificant elevation differences between the gauge stations considered (i.e. less than 310m). That notwithstanding, most of the missed and falsely detected rainfall originated from higher-elevated stations (i.e. Solwezi and Mwinilunga).

This study shows that detection skills of the rainfall products can be related to the dry and wet season periods. For wet seasons, rainfall is better detected than during dry seasons. However, in rainy seasons and in case of extreme rainfall events, bias was reported to be as large as 29.32 mm d^{-1}. TMPA outperformed the other products with best detecting of 88% of rainfall occurrence in wet periods.

Since CHIRPS is a blend-product of CHIRP and *in-situ* stations data, it was expected to outperform the other rainfall products in terms of detection skills. This was however not the case, and can possibly be explained by the omission of other rain gauge stations in and around Kabompo Basin. This except for Kaoma station that was used in the blending procedure by the product providers. A complete list of rain gauge stations used each month in the CHIRPS rainfall estimation algorithm is available at ftp://ftp.chg.ucsb.edu/pub/org/chg/products/CHIRPS-2.0/diagnostics/list_of_stations_used/monthly/. CHIRPS detection skills in dry season reduced to 20% that directly can be contributed to the less skilful nature in detecting low rainfall depths.

The SREs underestimates maximum and mean gauged rainfall. CMORPH shows the largest daily underestimation (1.56 mm) whereas TMPA has the lowest daily bias (less than 0.05 mm). Generally, CHIRPS and TMPA portrayed a closer match to gauged rainfall than CMORPH. CVs for the SREs were consistently lower during wet seasons than dry seasons. Error sources for SREs vary and are seasonally dependent, which conforms to Ward et al. (2011) findings. Wet seasons had the largest amount of hit rainfall and falsely detected rainfall than during dry seasons.

This study also shows that effectiveness of the selected bias correction schemes varies depending on what indicator is of focus, coinciding with Habib et al. (2014) findings. Errors in the SREs reduced on bias correction with DT, TFSV and TVSV being the most effective methods. DT has the best correlation coefficient > 0.7 and low standard deviation of 0.52 mm d^{-1}. TVSV shows the lowest daily bias (less than 0.09 mm) whereas TFSV was the best for correcting mean daily rainfall.

No perfect fit of observed discharge could be modelled by respective rainfall forcing types used. However, acceptable model efficiencies (evaluated on $NS \geq 0.6$ and RV_E of $\pm$10%) were obtained. TOPMODEL simulations based on bias corrected satellite rainfall estimates show visually improved hydrograph patterns than those by *in-situ* and uncorrected SREs rainfall. A clear improvement in water balance closure error is shown on bias correcting the satellite rainfall estimates to as low as 1.7%. in the basin.

6.2. Recommendation

Based on the findings, further research on improving CHIRPS rainfall detection of extreme rainfall occurrence in the basin is encouraged. In addition, to improve the CHIRPS accuracy, omitted rain gauge stations need to be incorporated in its blending procedure, to improve its performance.

Limited availability of rainfall gauges covering the extent of the Kabompo Basin was a major constraint in this study, and inconsistencies in the rainfall and discharge time series hampered streamflow simulation outputs. An increase in number of meteorological gauge stations across the basin, particularly for rainfall measurements, is recommended. Crucial for streamflow simulations in the basin are further investigations on spatial distribution of rainfall distributions and/or validating discharge records used, before concluding on TOPMODEL errors.

This study assessed and concluded on the effect of seasonal variations on products' rainfall detections. To improve the rainfall products' accuracies thereby reducing systematic errors, further studies should assess how the seasonality effect can be incorporated in these products algorithms.

Even though TOPMODEL requires modest number of calibration parameters, the 'trial and error' optimization procedure adopted in streamflow simulation was laborious. This would likely be facilitated by an automated calibration routine, but for further studies.

LIST OF REFERENCES

Abera, W., Brocca, L., & Rigon, R. (2016). Comparative evaluation of different satellite rainfall estimation products and bias correction in the Upper Blue Nile (UBN) basin. *Atmospheric Research*, *178–179*, 471–483. https://doi.org/10.1016/j.atmosres.2016.04.017

Aghakouchak, A., Mehran, A., Norouzi, H., & Behrangi, A. (2012). Systematic and random error components in satellite precipitation data sets. *Geophysical Research Letters*, *39*(9), n/a-n/a. https://doi.org/10.1029/2012GL051592

Alemohammad, S. H., McColl, K. A., Konings, A. G., Entekhabi, D., & Stoffelen, A. (2015). Characterization of precipitation product errors across the United States using multiplicative triple collocation. *Hydrology and Earth System Sciences*, *19*(8), 3489–3503. https://doi.org/10.5194/hess-19-3489-2015

Allen, R. G., Pereira, L. S., Raes, D., & Smith, M. (1998). *Crop Evapotranspiration (guidelines for computing crop water requirements). FAO Irrigation and drainage paper 56*. Rome, Italy: Food and Agriculture Organization of the United Nations. Retrieved from https://www.kimberly.uidaho.edu/water/fao56/fao56.pdf

Behrangi, A., Khakbaz, B., Jaw, T. C., AghaKouchak, A., Hsu, K., & Sorooshian, S. (2011). Hydrologic evaluation of satellite precipitation products over a mid-size basin. *Journal of Hydrology*, *397*(3–4), 225–237. https://doi.org/10.1016/j.jhydrol.2010.11.043

Beven, K., & Freer, J. (2001). A dynamic TOPMODEL. *Hydrological Processes*, *15*(10), 1993–2011. https://doi.org/10.1002/hyp.252

Beven, K. J., & Kirkby, M. J. (1979). A physically based, variable contributing area model of basin hydrology / Un modèle à base physique de zone d'appel variable de l'hydrologie du bassin versant. *Hydrological Sciences Bulletin*, *24*(1), 43–69. https://doi.org/10.1080/02626667909491834

Bhattacharya, B., & Solomatine, D. (2015). Bias correction of satellite-based rainfall data. *Geophysical Research Abstracts EGU General Assembly*, *17*, 2015–12502.

Bhatti, H., Rientjes, T., Haile, A., Habib, E., & Verhoef, W. (2016). Evaluation of Bias Correction Method for Satellite- Based Rainfall Data. *Sensors*, *16*(6), 884. https://doi.org/10.3390/s16060884

CGIAR. (1998). SRTM 90m DEM Digital Elevation Database. Retrieved November 18, 2016, from http://srtm.csi.cgiar.org/

Chai, T., & Draxler, R. R. (2014). Root mean square error (RMSE) or mean absolute error (MAE)? – Arguments against avoiding RMSE in the literature. *Geoscientific Model Development*, *7*(3), 1247–1250. https://doi.org/10.5194/gmd-7-1247-2014

Chen, J., Brissette, F. P., Chaumont, D., & Braun, M. (2013). Finding appropriate bias correction methods in downscaling precipitation for hydrologic impact studies over North America. *Water Resources Research*, *49*(7), 4187–4205. https://doi.org/10.1002/wrcr.20331

CHRS. (2004). Satellite Precipitation - Center for Hydrometeorology and Remote Sensing. Retrieved May 23, 2016, from http://www.chrs.web.uci.edu/research/satellite_precipitation/index.html

Cohen Liechti, T., Matos, J. P., Boillat, J.-L., & Schleiss, A. J. (2012). Comparison and evaluation of satellite derived precipitation products for hydrological modeling of the Zambezi River Basin. *Hydrology and Earth System Sciences*, *16*(2), 489–500. https://doi.org/10.5194/hess-16-489-2012

Cover, T., & Hart, P. (1967). Nearest neighbor pattern classification. *IEEE Transactions on Information Theory*, *13*(1), 21–27. https://doi.org/10.1109/TIT.1967.1053964

De Silva, R. P., Dayawansa, N. D. K., & Ratnasiri, M. D. (2016). A comparison of methods used in estimating missing rainfall data. *Journal of Agricultural Sciences*, *3*(2), 101. https://doi.org/10.4038/jas.v3i2.8107

Dempster, A. P., Laird, N. M., & Rubin, D. B. (1977). Maximum Likelihood from Incomplete Data via the EM Algorithm. *Journal of the Royal Statistical Society. Series B (Methodological)*, *39*(1), 1–38. Retrieved from http://links.jstor.org/sici?sici=0035-9246%281977%2939%3A1%3C1%3AMLFIDV%3E2.0.CO%3B2-Z

Devia, G. K., Ganasri, B. P., & Dwarakish, G. S. (2015). A Review on Hydrological Models. *Aquatic Procedia*, *4*(Icwrcoe), 1001–1007. https://doi.org/10.1016/j.aqpro.2015.02.126

Dinku, T., Chidzambwa, S., Ceccato, P., Connor, S. J., & Ropelewski, C. F. (2008). Validation of high resolution satellite rainfall products over complex terrain. *International Journal of Remote Sensing*, *29*(14), 4097–4110. https://doi.org/10.1080/01431160701772526

Dinku, T., Connor, S. J., & Ceccato, P. (2010). Comparison of CMORPH and TRMM-3B42 over Mountainous Regions of Africa and South America. In *Satellite Rainfall Applications for Surface Hydrology* (pp. 193–204). Dordrecht: Springer Netherlands. https://doi.org/10.1007/978-90-481-2915-7_11

Duncan, J. M. A., & Biggs, E. M. (2012). Assessing the accuracy and applied use of satellite-derived precipitation estimates over Nepal. *Applied Geography*, *34*, 626–638. https://doi.org/10.1016/j.apgeog.2012.04.001

ESRI. (2016). FAQ: What is the difference between Nearest Neighbor, Bilinear Interpolation and Cubic Convolution? Retrieved September 12, 2016, from http://support.esri.com/technical-article/000005606

Fang, G. H., Yang, J., Chen, Y. N., & Zammit, C. (2015). Comparing bias correction methods in downscaling meteorological variables for a hydrologic impact study in an arid area in China. *Hydrology and Earth System Sciences*, *19*(6), 2547–2559. https://doi.org/10.5194/hess-19-2547-2015

Farr, T. G., Rosen, P. A., Caro, E., Crippen, R., Duren, R., Hensley, S., … Alsdorf, D. (2007). The Shuttle Radar Topography Mission. *Reviews of Geophysics*, *45*(2), RG2004. https://doi.org/10.1029/2005RG000183

Funk, C. C., Peterson, P. J., Landsfeld, M. F., Pedreros, D. H., Verdin, J. P., Rowland, J. D., … Verdin, A. P. (2014). *A quasi-global precipitation time series for drought monitoring: U.S. Geological Survey Data Series 832*. https://doi.org/10.3133/ds832

Funk, C., Peterson, P., Landsfeld, M., Pedreros, D., Verdin, J., Shukla, S., … Michaelsen, J. (2015). The climate hazards infrared precipitation with stations—a new environmental record for monitoring extremes. *Scientific Data*, *2*, 150066. https://doi.org/10.1038/sdata.2015.66

Gosset, M., Viarre, J., Quantin, G., & Alcoba, M. (2013). Evaluation of several rainfall products used for hydrological applications over West Africa using two high-resolution gauge networks. *Quarterly Journal of the Royal Meteorological Society*, *139*(673), 923–940. https://doi.org/10.1002/qj.2130

Gotway, C. A., & Young, L. J. (2002). Combining Incompatible Spatial Data. *Journal of the American Statistical Association*, *97*(458), 632–648. https://doi.org/10.1198/016214502760047140

Gumindoga, W. (2010). Hydrologic impacts of landuse change in the Upper Gilgel Abay River bassin, Ethiopia : TOPMODEL application. *ITC MSc. Thesis*. Retrieved from http://www.itc.nl/library/papers_2010/msc/wrem/gumindoga.pdf

Gumindoga, W., Rientjes, T. H. M., Haile, A. T., & Dube, T. (2014). Predicting streamflow for land cover changes in the Upper Gilgel Abay River Basin, Ethiopia: A TOPMODEL based approach. *Physics and Chemistry of the Earth, Parts A/B/C*, *76*, 3–15. https://doi.org/10.1016/j.pce.2014.11.012

Gumindoga, W., Rientjes, T. H. M., Haile, A. T., Makurira, H., & Reggiani, P. (2016). Bias correction schemes for CMORPH satellite rainfall estimates in the Zambezi River Basin. *Hydrology and Earth System Sciences Discussions*, *0*, 1–36. https://doi.org/10.5194/hess-2016-33

Gumindoga, W., Rwasoka, D. T., & Murwira, A. (2011). Simulation of streamflow using TOPMODEL in the Upper Save River catchment of Zimbabwe. *Physics and Chemistry of the Earth*, *36*(14–15), 806–813. https://doi.org/10.1016/j.pce.2011.07.054

Habib, E., ElSaadani, M., & Haile, A. T. (2012). Climatology-Focused Evaluation of CMORPH and TMPA Satellite Rainfall Products over the Nile Basin. *Journal of Applied Meteorology and Climatology*, *51*(12), 2105–2121. https://doi.org/10.1175/JAMC-D-11-0252.1

Habib, E., Haile, A., Sazib, N., Zhang, Y., & Rientjes, T. (2014). Effect of Bias Correction of Satellite-Rainfall Estimates on Runoff Simulations at the Source of the Upper Blue Nile. *Remote Sensing*, *6*(7), 6688–6708. https://doi.org/10.3390/rs6076688

Haile, A. T., Habib, E., & Rientjes, T. (2013). Evaluation of the climate prediction center (CPC) morphing technique (CMORPH) rainfall product on hourly time scales over the source of the Blue Nile River. *Hydrological Processes*, *27*(12), 1829–1839. https://doi.org/10.1002/hyp.9330

Hirpa, F. A., Gebremichael, M., & Hopson, T. (2010). Evaluation of High-Resolution Satellite Precipitation Products over Very Complex Terrain in Ethiopia. *Journal of Applied Meteorology and Climatology*, *49*(5), 1044–1051. https://doi.org/10.1175/2009JAMC2298.1

Hong, Y., Hsu, K., Moradkhani, H., & Sorooshian, S. (2006). Uncertainty quantification of satellite precipitation estimation and Monte Carlo assessment of the error propagation into hydrologic response. *Water Resources Research*, *42*(8). https://doi.org/10.1029/2005WR004398

Huffman, G. (2013). Algorithm 3B42: TRMM Merged HQ/Infrared Precipitation. Retrieved October 29, 2016, from http://trmm.gsfc.nasa.gov/3b42.html

Huffman, G. J., Adler, R. F., Bolvin, D. T., & Nelkin, E. J. (2010). The TRMM Multi-Satellite Precipitation Analysis (TMPA). In *Satellite Rainfall Applications for Surface Hydrology* (pp. 3–22). Dordrecht: Springer Netherlands. https://doi.org/10.1007/978-90-481-2915-7_1

Huffman, G. J., Bolvin, D. T., Nelkin, E. J., Wolff, D. B., Adler, R. F., Gu, G., … Stocker, E. F. (2007). The TRMM Multisatellite Precipitation Analysis (TMPA): Quasi-Global, Multiyear, Combined-Sensor Precipitation Estimates at Fine Scales. *Journal of Hydrometeorology*, *8*(1), 38–55. https://doi.org/10.1175/JHM560.1

Huffman, G. J., Pendergrass, A., & National Center for Atmospheric Research Staff (Eds). (2016). The Climate Data Guide: TRMM: Tropical Rainfall Measuring Mission. Retrieved October 28, 2016, from https://climatedataguide.ucar.edu/climate-data/trmm-tropical-rainfall-measuring-mission

Hyndman, R. J., & Koehler, A. B. (2006). Another look at measures of forecast accuracy. *International Journal of Forecasting*, *22*(4), 679–688. https://doi.org/10.1016/j.ijforecast.2006.03.001

Ines, A. V. M., & Hansen, J. W. (2006). Bias correction of daily GCM rainfall for crop simulation studies. *Agricultural and Forest Meteorology*, *138*(1), 44–53. https://doi.org/10.1016/j.agrformet.2006.03.009

Jagalingam, P., & Hegde, A. V. (2015). A Review of Quality Metrics for Fused Image. *Aquatic Procedia*, *4*, 133–142. https://doi.org/10.1016/j.aqpro.2015.02.019

Janssen, P. H. M., & Heuberger, P. S. C. (1995). Calibration of process-oriented models. *Ecological Modelling*, *83*(1–2), 55–66. https://doi.org/10.1016/0304-3800(95)00084-9

Jobard, I., Chopin, F., Berges, J. C., & Roca, R. (2011). An intercomparison of 10-day satellite precipitation products during West African monsoon. *International Journal of Remote Sensing*, *32*(9), 2353–2376. https://doi.org/10.1080/01431161003698286

Joyce, R. J., Janowiak, J. E., Arkin, P. A., & Xie, P. (2004). CMORPH: A Method that Produces Global Precipitation Estimates from Passive Microwave and Infrared Data at High Spatial and Temporal Resolution. *Journal of*

Hydrometeorology, *5*(3), 487–503. https://doi.org/10.1175/1525-7541(2004)005<0487:CAMTPG>2.0.CO;2

Joyce, R. J., Xie, P., Yarosh, Y., Janowiak, J. E., & Arkin, P. A. (2010). CMORPH: A morphing approach for high resolution precipitation product generation. In M. Gebremichael & F. Hossain (Eds.), *Satellite Rainfall Applications for Surface Hydrology* (pp. 23–37). Dordrecht: Springer Netherlands. https://doi.org/10.1007/978-90-481-2915-7_2

K. Yamamoto, M., UENO, K., & NAKAMURA, K. (2011). Comparison of Satellite Precipitation Products with Rain Gauge Data for the Khumb Region, Nepal Himalayas. *Journal of the Meteorological Society of Japan*, *89*(6), 597–610. https://doi.org/10.2151/jmsj.2011-601

Kampata, J. M. J., Rientjes, T. H. M., & Timmermans, J. (2013). Effects of Land Cover Change on the Hydrologic Regime of Kabompo River Basin , Zambia. In *ESA Living Planet Symposium* (Vol. 2013, pp. 1–6). ESA. Retrieved from http://www.narcis.nl/publication/RecordID/oai%3Adoc.utwente.nl%3A90380

Khan, S. I., Hong, Y., Wang, J., Yilmaz, K. K., Gourley, J. J., Adler, R. F., … Irwin, D. (2011). Satellite Remote Sensing and Hydrologic Modeling for Flood Inundation Mapping in Lake Victoria Basin: Implications for Hydrologic Prediction in Ungauged Basins. *IEEE Transactions on Geoscience and Remote Sensing*, *49*(1), 85–95. https://doi.org/10.1109/TGRS.2010.2057513

Lafon, T., Dadson, S., Buys, G., & Prudhomme, C. (2013). Bias correction of daily precipitation simulated by a regional climate model: a comparison of methods. *International Journal of Climatology*, *33*(6), 1367–1381. https://doi.org/10.1002/joc.3518

Lee, J.-K., Kim, J.-H., & Suk, M.-K. (2015). Application of bias correction methods to improve the accuracy of quantitative radar rainfall in Korea. *Atmospheric Measurement Techniques Discussions*, *8*(4), 4011–4047. https://doi.org/10.5194/amtd-8-4011-2015

Li, H., Sheffield, J., & Wood, E. F. (2010). Bias correction of monthly precipitation and temperature fields from Intergovernmental Panel on Climate Change AR4 models using equidistant quantile matching. *Journal of Geophysical Research*, *115*(D10), D10101. https://doi.org/10.1029/2009JD012882

Liu, Z. (2015). Comparison of precipitation estimates between Version 7 3-hourly TRMM Multi-Satellite Precipitation Analysis (TMPA) near-real-time and research products. *Atmospheric Research*, *153*, 119–133. https://doi.org/10.1016/j.atmosres.2014.07.032

Maathuis, B. H. P., & Wang, L. (2006). Digital Elevation Model Based Hydro-processing. *Geocarto International*, *21*(1), 21–26. https://doi.org/10.1080/10106040608542370

Maathuis, B., Mannaerts, C., Schouwenburg, M., Retsios, B., Lemmens, R., & Nkepu, M. R. (2014). In Situ and Online Data Toolbox User Guide. Enschede, The Netherlands: University of Twente. Retrieved from http://52north.org/files/earth-observation/userguides/isod/ISOD_Toolbox_V1.4UG.pdf

Maggioni, V., Vergara, H. J., Anagnostou, E. N., Gourley, J. J., Hong, Y., & Stampoulis, D. (2013). Investigating the Applicability of Error Correction Ensembles of Satellite Rainfall Products in River Flow Simulations. *Journal of Hydrometeorology*, *14*(4), 1194–1211. https://doi.org/10.1175/JHM-D-12-074.1

Mashingia, F., Mtalo, F., & Bruen, M. (2014). Validation of remotely sensed rainfall over major climatic regions in Northeast Tanzania. *Physics and Chemistry of the Earth, Parts A/B/C*, *67*, 55–63. https://doi.org/10.1016/j.pce.2013.09.013

Mei, Y., Anagnostou, E. N., Nikolopoulos, E. I., & Borga, M. (2014). Error Analysis of Satellite Precipitation Products in Mountainous Basins. *Journal of Hydrometeorology*, *15*(5), 1778–1793. https://doi.org/10.1175/JHM-D-13-0194.1

Michelle, L. (1997). Statistical Topics: Multiple Linear Regression. Retrieved October 24, 2016, from http://www.stat.yale.edu/Courses/1997-98/101/linmult.htm

Moazami, S., Golian, S., Kavianpour, M. R., & Hong, Y. (2014). Uncertainty analysis of bias from satellite rainfall estimates using copula method. *Atmospheric Research*, *137*, 145–166. https://doi.org/10.1016/j.atmosres.2013.08.016

Muhammed, A. H. (2012). *Satellite Based Evapotranspiration Estimation and Runoff Simulation : a Topmodel Application To the Gilgel Abay Catchment , Ethiopia*. *ITC MSc. Thesis*. University of Twente Faculty of Geo-Information and Earth Observation (ITC).

Mwiza, M. (2012). *Application of remote sensing using a GIS based soil water assessment tool(SWAT)to estimate river discharge in the Kabompo river basin-Zambia*. *University of Zambia Ph.D Thesis*. University of Zambia. Retrieved from http://hdl.handle.net/123456789/991

Nash, J. E., & Sutcliffe, J. V. (1970). River flow forecasting through conceptual models part I — A discussion of principles. *Journal of Hydrology*, *10*(3), 282–290. https://doi.org/10.1016/0022-1694(70)90255-6

Noori, M. J., Hassan, H. H., & Mustafa, Y. T. (2014). Spatial Estimation of Rainfall Distribution and Its Classification in Duhok Governorate Using GIS. *Journal of Water Resource and Protection*, *6*(2), 75–82. https://doi.org/10.4236/jwarp.2014.62012

Nourani, V., Hosseini Baghanam, A., Adamowski, J., & Kisi, O. (2014). Applications of hybrid wavelet–Artificial Intelligence models in hydrology: A review. *Journal of Hydrology*, *514*, 358–377. https://doi.org/10.1016/j.jhydrol.2014.03.057

Pan, M., Li, H., & Wood, E. (2010). Assessing the skill of satellite-based precipitation estimates in hydrologic applications. *Water Resources Research*, *46*(9), n/a-n/a. https://doi.org/10.1029/2009WR008290

Piani, C., Haerter, J. O., & Coppola, E. (2010). Statistical bias correction for daily precipitation in regional climate models over Europe. *Theoretical and Applied Climatology*, *99*(1–2), 187–192. https://doi.org/10.1007/s00704-009-0134-9

Quinn, P. F., Beven, K. J., & Lamb, R. (1995). The in(a/tan/β) index: How to calculate it and how to use it within the topmodel framework. *Hydrological Processes*, *9*(2), 161–182. https://doi.org/10.1002/hyp.3360090204

Rientjes, T. (2015). *Hydrologic modelling for Intergated Water Resource*. *Lecture notes for Module 9-10 surface water stream*.

Rientjes, T. H. M., Haile, A. T., Kebede, E., Mannaerts, C. M. M., Habib, E., & Steenhuis, T. S. (2011). Changes in land cover, rainfall and stream flow in Upper Gilgel Abbay catchment, Blue Nile basin – Ethiopia. *Hydrology and Earth System Sciences*, *15*(6), 1979–1989. https://doi.org/10.5194/hess-15-1979-2011

Roberto, J. (2011). *Contrasting two catchments with hydrological modelling in the Guatiquia river basin, Paramo Chingaza, Colombia*. *ITC MSc. Thesis*. University of Twente Faculty of Geo-Information and Earth Observation (ITC). Retrieved from http://adlib.itc.utwente.nl/detail.aspx?parentpriref=

Santhos, B., & Devi, Mr. (2010). An Analysis of Different Resampling Methods in Coimbatore, District. *Global Journal of Computer Science and Technology*, *10*(10).

Searcy, J. K., & Hardison, C. H. (1960). *Double-Mass Curves: Manual of Hydrology - Part 1. General Surface-Water Techniques*. Washington DC: United states Government Printing Office.

Seo, D.-J., Breidenbach, J. ., & Johnson, E. . (1999). Real-time estimation of mean field bias in radar rainfall data. *Journal of Hydrology*, *223*(3–4), 131–147. https://doi.org/10.1016/S0022-1694(99)00106-7

Shepard, D. (1968). A two-dimensional interpolation function for irregularly-spaced data. In *Proceedings of the 1968 23rd ACM national conference on* - (pp. 517–524). New York, New York, USA: ACM Press. https://doi.org/10.1145/800186.810616

Siwila, S., Taye, M. T., Quevauviller, P., & Willems, P. (2013). Climate Change Impact Investigation on Hydro-

Meteorological Extremes on Zambia' s Kabompo Catchment. *Associazione Acque Sotteranee*, 29–40. https://doi.org/10.4409/Am-057-13-0050

Smith, T. M., Arkin, P. A., Bates, J. J., & Huffman, G. J. (2006). Estimating Bias of Satellite-Based Precipitation Estimates. *Journal of Hydrometeorology*, *7*(5), 841–856. https://doi.org/10.1175/JHM524.1

Studley, H., & Weber, K. T. (2011). Comparison of Image Resampling Techniques for Satellite Imagery. In K. T. Weber & K. Davis (Eds.), *Final Report: Assessing Post-Fire Recovery of Sagebrush-Steppe Rangelands in Southeastern Idaho* (pp. 185–196).

Sun, Z., Gebremichael, M., Ardö, J., Nickless, A., Caquet, B., Merboldh, L., & Kutschi, W. (2012). Estimation of daily evapotranspiration over Africa using MODIS/Terra and SEVIRI/MSG data. *Atmospheric Research*, *112*, 35–44. https://doi.org/10.1016/j.atmosres.2012.04.005

Taylor, K. E. (2001). Summarizing multiple aspects of model performance in a single diagram. *Journal of Geophysical Research: Atmospheres*, *106*(D7), 7183–7192. https://doi.org/10.1029/2000JD900719

Teng, J., Potter, N. J., Chiew, F. H. S., Zhang, L., Wang, B., Vaze, J., & Evans, J. P. (2015). How does bias correction of regional climate model precipitation affect modelled runoff? *Hydrology and Earth System Sciences*, *19*(2), 711–728. https://doi.org/10.5194/hess-19-711-2015

Thiessen, A. H. (1911). Precipitation avaerages for large areas. *Monthly Weather Review*, *39*(7), 1082–1089. https://doi.org/10.1175/1520-0493(1911)39<1082b:PAFLA>2.0.CO;2

Tian, X., Dai, A., Yang, D., & Xie, Z. (2007). Effects of precipitation-bias corrections on surface hydrology over northern latitudes. *Journal of Geophysical Research Atmospheres*, *112*(14), D14101. https://doi.org/10.1029/2007JD008420

Tian, Y., Peters-Lidard, C. D., Eylander, J. B., Joyce, R. J., Huffman, G. J., Adler, R. F., … Zeng, J. (2009). Component analysis of errors in satellite-based precipitation estimates. *Journal of Geophysical Research*, *114*(D24), D24101. https://doi.org/10.1029/2009JD011949

Tobin, K. J., & Bennett, M. E. (2010). Adjusting Satellite Precipitation Data to Facilitate Hydrologic Modeling. *Journal of Hydrometeorology*, *11*(4), 966–978. https://doi.org/10.1175/2010JHM1206.1

Tramblay, Y., Thiemig, V., Dezetter, A., & Hanich, L. (2016). Evaluation of satellite-based rainfall products for hydrological modelling in Morocco. *Hydrological Sciences Journal*, *6667*(March), 1–11. https://doi.org/10.1080/02626667.2016.1154149

Valdés-Pineda, R., Demaría, E. M. C., Valdés, J. B., Wi, S., & Serrat-Capdevilla, A. (2016). Bias correction of daily satellite-based rainfall estimates for hydrologic forecasting in the Upper Zambezi, Africa. *Hydrology and Earth System Sciences Discussions*, 1–28. https://doi.org/10.5194/hess-2016-473

Wagner, S., Kunstmann, H., Bárdossy, A., Conrad, C., & Colditz, R. R. (2009). Water balance estimation of a poorly gauged catchment in West Africa using dynamically downscaled meteorological fields and remote sensing information. *Physics and Chemistry of the Earth, Parts A/B/C*, *34*(4–5), 225–235. https://doi.org/10.1016/j.pce.2008.04.002

Ward, E., Buytaert, W., Peaver, L., & Wheater, H. (2011). Evaluation of precipitation products over complex mountainous terrain: A water resources perspective. *Advances in Water Resources*, *34*(10), 1222–1231. https://doi.org/10.1016/j.advwatres.2011.05.007

Wilks, D. S. (2006). *Statistical methods in the atmospheric sciences*. (H. T. R. Renata Dmowska, Dennis Hartmann, Ed.), *International Geophysics Series* (Second, Vol. 91).

World Bank. (2010). *The Zambezi river basin: a multi-sector investment opportunities analysis*. *State of the Basin* (Vol. 3). Washington, DC. Retrieved from http://documents.worldbank.org/curated/en/938311468202138918/State-of-the-Basin

WWF. (2006). Tropical and subtropical dry broadleaf forests, Southern Africa: Zambia (Angola). Retrieved from http://www.worldwildlife.org/ecoregions/at0203

Xianghu, L., Zhang, Q., & Xu, C.-Y. (2014). Assessing the performance of satellite-based precipitation products and its dependence on topography over Poyang Lake basin. *Theoretical and Applied Climatology*, *115*(3–4), 713–729. https://doi.org/10.1007/s00704-013-0917-x

Yang, Y., & Luo, Y. (2014). Evaluating the performance of remote sensing precipitation products CMORPH, PERSIANN, and TMPA, in the arid region of northwest China. *Theoretical and Applied Climatology*, *118*(3), 1–17. https://doi.org/10.1007/s00704-013-1072-0

Yusuf, Y., Sri Sumantyo, J. T., & Kuze, H. (2013). Spectral information analysis of image fusion data for remote sensing applications. *Geocarto International*, *28*(4), 291–310. https://doi.org/10.1080/10106049.2012.692396

ZEMA, GRID-Arendal, GRID-Sioux Falls, UNEP. (2012). *Zambia Atlas of Our Changing Environment*. Lusaka, Arendal, Sioux Falls and Nairobi. Retrieved from http://www.grida.no/publications/zambia-atlas/

Zotarelli, L., Dukes, M. D., Romero, C. C., Migliaccio, K. W., & Morgan, K. T. (2013). Step by step calculation of the Penman-Monteith Evapotranspiration (FAO-56 Method). *Institute of Food and Agricultural Sciences (IFAS)*, 1–10. Retrieved from https://edis.ifas.ufl.edu/pdffiles/AE/AE45900.pdf

APPENDICES

Appendix A Daily variation of FEWSNET and FAO-56 based ET_0 estimates (2008-2011).

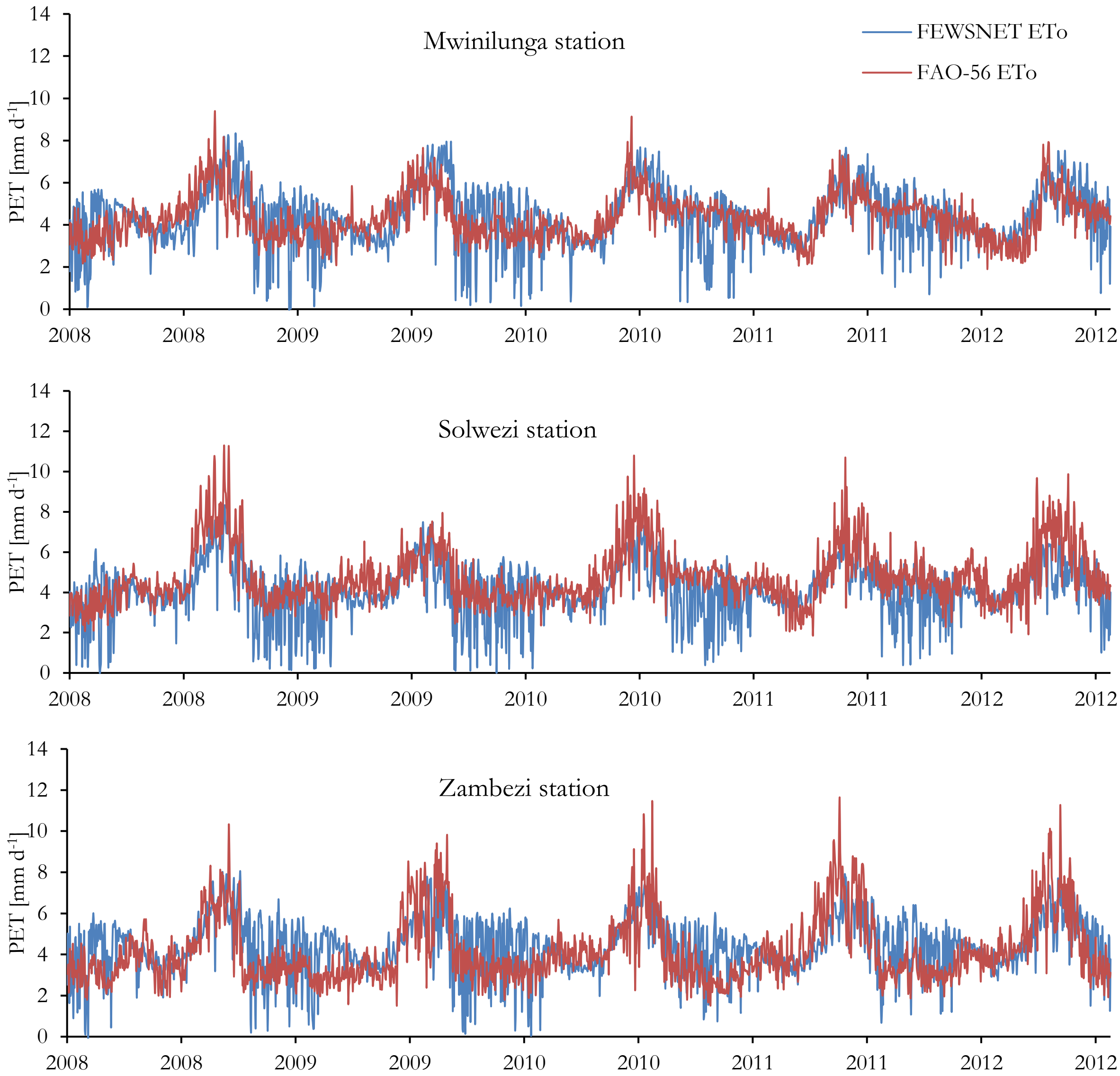

Appendix B Cumulative and scatter plots for daily FEWSNET and FAO-56 ET_0 estimates (2008-2012).

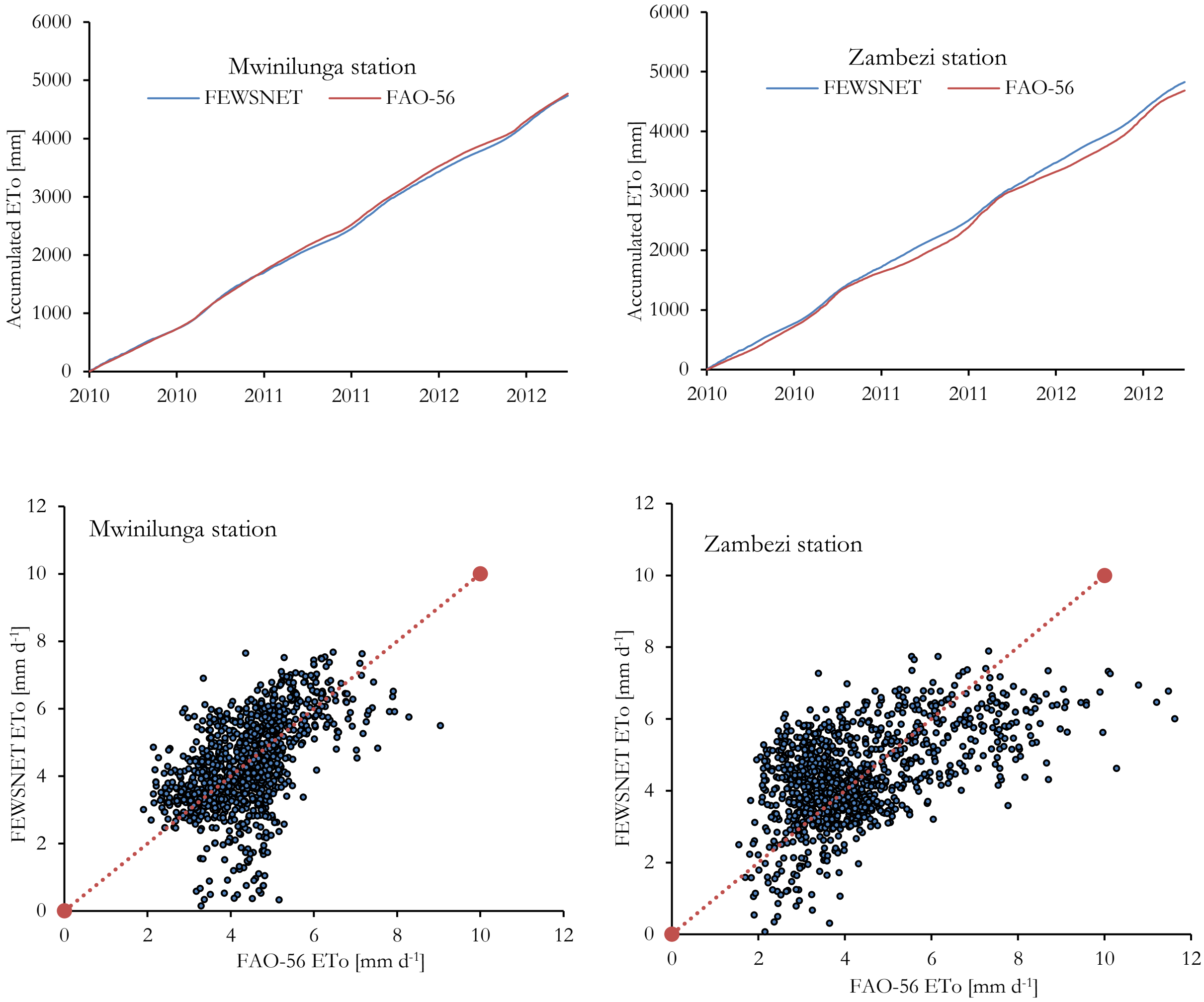

Appendix C Showing TMPA-imagery of 31/12/2008 when interpolated using nearest neighbour, bilinear and bicubic methods at 0.05°, 0.07° and 0.25° grids for a sub-catchment in Kabompo Basin. A clear indication of how resampling have difficulties reproducing maximum pixel values.

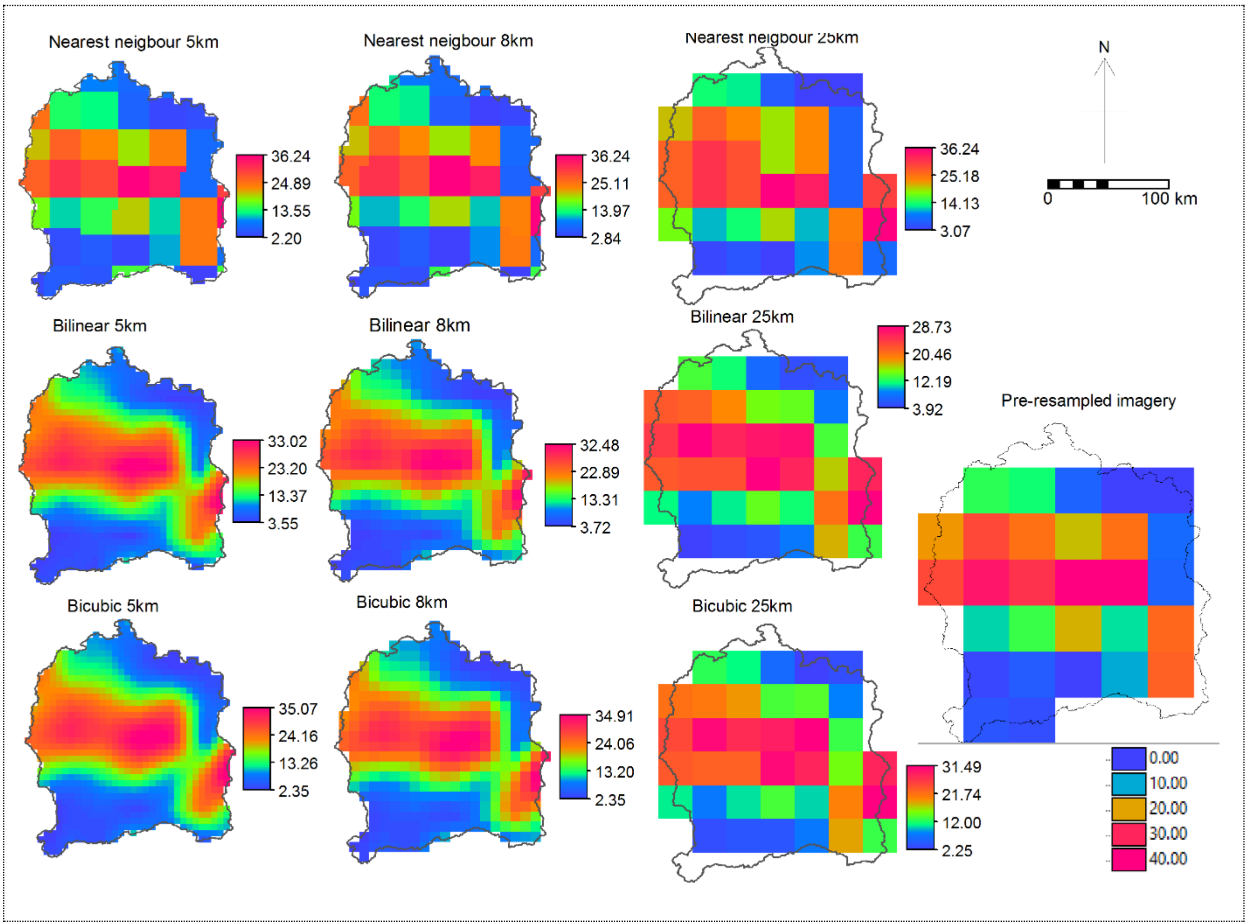

Appendix D Respective interpolation methods' mean bias expressed as a percentage of satellite estimates in the basin at daily, monthly, seasonal and >20mm d^{-1} rainfall occurrence in the basin at 0.05°, 0.07° and 0.25° grid sizes

Appendix E Scatterplots of various satellite-based rainfall and *in-situ* measurements in Kabompo Basin.

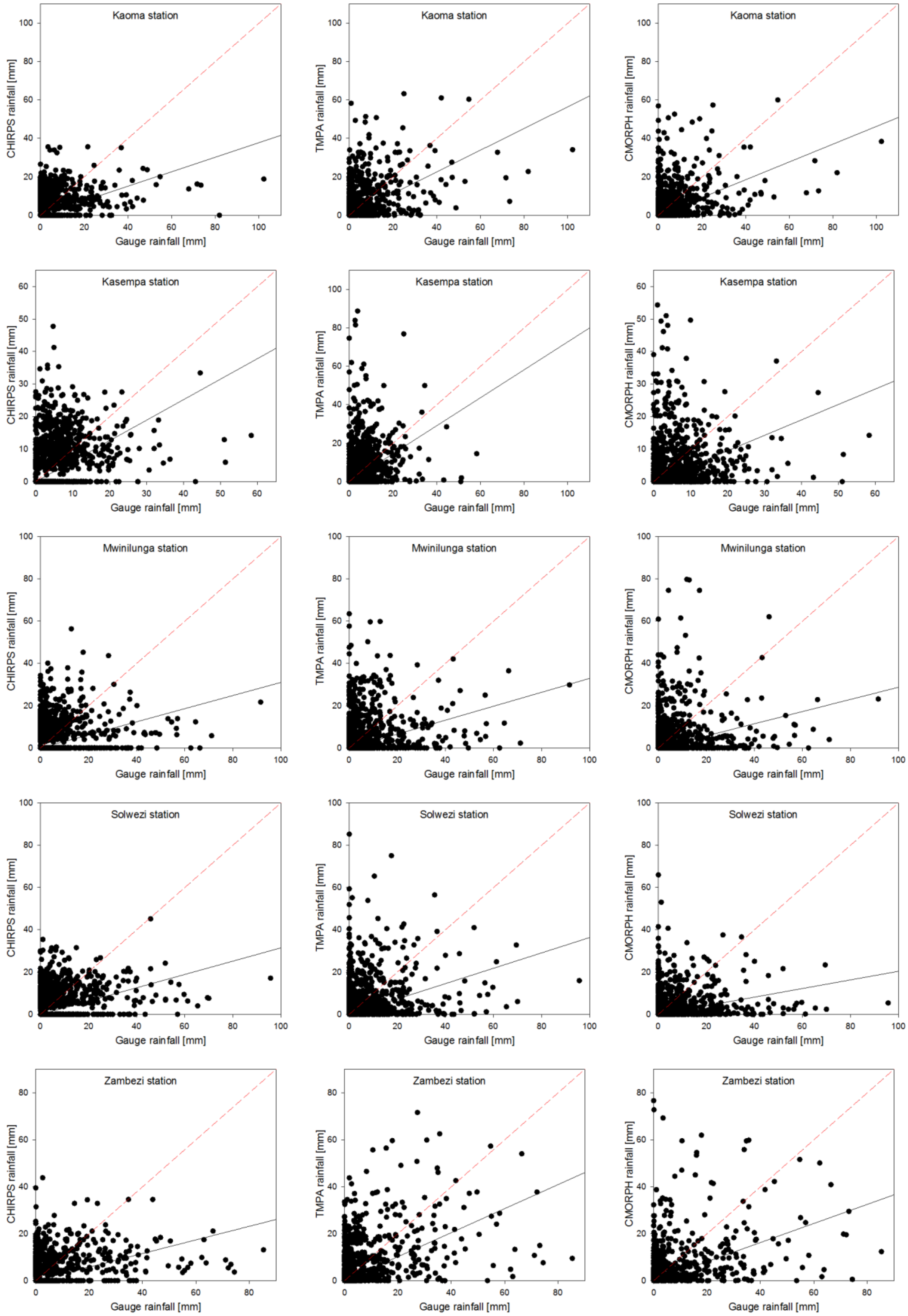

Appendix F Scatterplots comparing performance of CHIRPS, CMORPH and TMPA in Kabompo Basin